

The Microwave SQUID Multiplexer

by

John Arthur Benson Mates

B.A., Swarthmore College, 2004

A thesis submitted to the
Faculty of the Graduate School of the
University of Colorado in partial fulfillment
of the requirements for the degree of
Doctor of Philosophy
Department of Physics

2011

This thesis entitled:
The Microwave SQUID Multiplexer
written by John Arthur Benson Mates
has been approved for the Department of Physics

Kent Irwin

Prof. Konrad Lehnert

Date _____

The final copy of this thesis has been examined by the signatories, and we find that both the content and the form meet acceptable presentation standards of scholarly work in the above mentioned discipline.

Mates, John Arthur Benson (Ph.D., Physics)

The Microwave SQUID Multiplexer

Thesis directed by Dr. Kent Irwin

This thesis describes a multiplexer of Superconducting Quantum Interference Devices (SQUIDS) with low-noise, ultra-low power dissipation, and great scalability. The multiplexer circuit measures the magnetic flux in a large number of unshunted rf SQUIDS by coupling each SQUID to a superconducting microwave resonator tuned to a unique resonance frequency and driving the resonators from a common feedline. A superposition of microwave tones measures each SQUID simultaneously using only two coaxial cables between the cryogenic device and room temperature. This multiplexer will enable the instrumentation of arrays with hundreds of thousands of low-temperature detectors for new applications in cosmology, materials analysis, and nuclear non-proliferation.

The driving application of the Microwave SQUID Multiplexer is the readout of large arrays of superconducting transition-edge sensors, by some figures of merit the most sensitive detectors of electromagnetic signals over a span of more than nine orders of magnitude in energy, from 40 GHz microwaves to 200 keV gamma rays. Modern transition-edge sensors have noise-equivalent power as low as $10^{-20} \text{ W}/\sqrt{\text{Hz}}$ and energy resolution as good as 2 eV at 6 keV. These per-pixel sensitivities approach theoretical limits set by the underlying signals, motivating a rapid increase in pixel count to access new science. Compelling applications, like the non-destructive assay of nuclear material for treaty verification or the search for primordial gravity waves from inflation use arrays of these detectors to increase collection area or tile a focal plane.

We developed three generations of SQUID multiplexers, optimizing the first for flux noise ($0.17 \mu\Phi_0/\sqrt{\text{Hz}}$), the second for input current noise ($19 \text{ pA}/\sqrt{\text{Hz}}$), and the last for practical multiplexing of large arrays of cosmic microwave background polarimeters based on transition-edge sensors. Using the last design we demonstrated multiplexed readout of prototype polarimeters with the performance required for the future development of a large-scale astronomical instrument.

Acknowledgements

It has been a privilege to work under Kent Irwin for the last five years. He introduced me to the world of superconducting devices and the details of modern SQUID design. His passion is astonishing and infectious. When Kent joined me in the lab, I knew I would get home late, but I usually didn't mind. Working with him is exciting rather than draining. He taught me about physics, design, funding and academia, and life in general. I could not have had a better advisor.

It has also been a privilege to work with Professor Konrad Lehnert. He introduced me to the theory of superconducting microwave resonators and to experimental techniques at microwave frequencies. A mere three weeks in his lab resulted in my first academic paper.

I thank everyone in my research group who helped me throughout my graduate school career. Randy Doriese was the first to show me how to measure SQUIDS. Dan Schmidt taught me essential practical skills in electronics, cryogenics, and machining, and has been the most consistently useful resource of my scientific apprenticeship. Lisa Ferriera taught me to wirebond and enumerable small tricks of soldering and electronics assembly. Gene Hilton helped me often with software development and was always willing to take time to help me understand the constraints of fabrication. Leila Vale gave me perhaps more than anyone by fabricating the devices in this thesis.

Finally, I want to thank Rob Horansky for constantly teaching me about how to succeed as a young scientist and Mr. Galen O'Neil for sustaining me with humor and friendship. In a tiny office for three people, I never felt crowded or uncomfortable.

Contents

Chapter

1	Introduction	1
1.1	Low-Temperature Detectors	1
1.2	Transition-Edge Sensors	2
1.3	Superconducting Quantum Interference Devices	4
1.4	Arrays and Multiplexing	7
1.5	Microwave Kinetic Inductance Detectors	9
1.6	Microwave SQUID Multiplexer	10
1.7	Bolometric Applications	12
1.8	Spectroscopic Applications	13
2	Theory	16
2.1	Dissipationless rf SQUID	17
2.1.1	Josephson Junction Inductance	17
2.1.2	Non-hysteretic rf SQUIDs	18
2.1.3	Measuring the SQUID Inductance	20
2.1.4	Junction Resistance and Capacitance	21
2.2	Resonance Frequency	22
2.2.1	Ideal Quarter-Wave Resonator	22
2.2.2	Capacitive Coupling	24

2.2.3	Inductive Load	25
2.2.4	Variation in Load Inductance	27
2.3	Resonator Bandwidth	28
2.3.1	Resonance Shape	28
2.3.2	Coupled Q	30
2.3.3	Response to Frequency Shift	31
2.3.4	Energy in the Resonator	31
2.3.5	Driven Steady-State	33
2.3.6	Power Dissipation in the Terminations	34
2.3.7	Antinode Current	36
2.3.8	Matching Frequency Shift to Bandwidth	36
2.3.9	Crosstalk and Resonance Spacing	38
2.4	Losses in the Resonator Circuit	39
2.4.1	CPW Radiation	39
2.4.2	Dielectric Loss	39
2.4.3	Loss in the Flux Input Circuit	40
2.4.4	S_{21}^{min}	42
2.5	Flux Noise	43
2.5.1	Johnson Noise	43
2.5.2	SQUID Noise	43
2.5.3	HEMT noise	44
2.5.4	TLS noise	44
2.6	Flux-ramp Modulation	45
3	Fabrication	47
3.1	Substrate	47
3.2	Junction Fabrication	47

3.3 SQUID and Resonator Fabrication	48
4 Measurement Setup	49
4.1 Open-Source Electronics	53
5 Design Summary	54
6 μmux07a: Low Flux Noise	55
6.1 Design	55
6.1.1 Resonator Design	55
6.1.2 Resonator-Feedline Coupling	56
6.1.3 Critical Current	58
6.1.4 Coil Geometry	58
6.2 Filter Design	59
6.3 Results	60
6.3.1 Resonance Spacing	60
6.3.2 Flux-variable Resonance Frequency	61
6.3.3 Flux Noise	62
6.3.4 Flux-ramp Modulation	63
6.3.5 Summary	64
7 μmux09a: Low Input Current Noise	65
7.1 Design	65
7.1.1 Resonator Design	65
7.1.2 Resonator-Feedline Coupling	65
7.1.3 Critical Current	65
7.1.4 Coil Geometry	66
7.1.5 SQUID-Resonator Coupling	67
7.2 Filter Design	72

7.3	Results	73
7.3.1	Resonance Spacing	73
7.3.2	Flux-variable Resonance Frequency	74
7.3.3	Flux Noise and Current Noise	75
7.3.4	TES Readout	75
7.3.5	Summary	77
8	μ mux10b: Multiplexer for CMB TESs	78
8.1	Design	78
8.1.1	Resonator Design	78
8.1.2	Resonator-Feedline Coupling	79
8.1.3	Coil Geometry	80
8.1.4	Filter Design	81
8.2	Results	81
8.2.1	Resonance Spacing	81
8.2.2	Flux-variable Resonance Frequency	83
8.2.3	Flux Noise and Frequency Noise	84
8.2.4	Flux Ramp Modulation	86
8.3	SQUID Multiplexing Demonstration	91
8.4	TES Multiplexing	92
8.5	TES Readout	93
8.5.1	Summary	94
9	Future Work	95
9.1	Multiplexer Re-design	95
9.1.1	Surface State Reduction	95
9.1.2	SQUID Design	96
9.1.3	Resonator Geometry	96

9.2	Microwave Launches	97
9.3	Room Temperature Electronics	97
9.4	Lumped-Element Resonators	98
9.5	Multiplexer Efficiency	98
9.5.1	Multi-SQUID Resonators	99
9.5.2	Hybrid Multiplexing	100
10	Conclusion	103
Bibliography		104
Appendix		
A	Instruments and Components	109
B	Transformer Coupling Calculations	110
B.1	Shunted Junction	111
B.2	Input Filter	112
C	Derivative of Resonator Impedance	114

Tables

Table

7.1	Simulated inductance values for a weak inductive coupling	69
7.2	Simulated inductance values for a strong inductive coupling	70
7.3	Simulated inductance values for a variable inductive coupling	71

Figures

Figure

1.1	Applications of low-temperature detectors span the electromagnetic spectrum	1
1.2	Example transition between superconducting and normal states of a transition-edge sensor . .	2
1.3	Illustration of an ideal bolometer/calorimeter	3
1.4	Artistic representations and accurate schematics of different SQUIDS.	5
1.5	Schematic of dc-SQUID readout of a voltage-biased TES.	6
1.6	Sensitivity and pixel count trends	7
1.7	MKID resonance curves	9
1.8	Schematic of a three-pixel MKID device	10
1.9	Schematic of a three-pixel device with TESs	10
1.10	Schematic of a three-pixel device with rf SQUIDS	11
1.11	E-mode and B-mode components of the CMB	13
1.12	Spectra of a plutonium sample	14
1.13	TES microcalorimeter array with 256 pixels	14
1.14	Megapixel x-ray CCD camera	15
2.1	Circuit schematic of the Microwave SQUID Multiplexer	16
2.2	Schematic representation of a Josephson Junction.	17
2.3	Schematic representation of an rf SQUID.	18
2.4	Relationship between externally applied and total magnetic flux	19

2.5	Circuit diagram of an rf SQUID screening another inductor.	20
2.6	Flux variable inductance of the termination	20
2.7	SQUID circuit including leakage resistance and junction capacitance.	21
2.8	Illustration of voltage and current along a perfect quarter-wave resonator.	23
2.9	Circuit diagram of a quarter-wave resonator capacitively coupled to a microwave feedline.	24
2.10	A length of transmission line, terminated with a load impedance.	24
2.11	A quarter-wave resonator loaded by an inductor screened by an rf SQUID	26
2.12	Flux variable resonance frequency	27
2.13	Illustration of resonance circle	28
2.14	Transmitted power at different frequencies near resonance	30
2.15	Illustration of the voltage waves for a resonator driven on resonance.	33
2.16	Transmitted power as a function of frequency and magnetic flux	37
2.17	Schematic of the rf SQUID and input coil coupling to both the resonator and each other.	41
3.1	Diagram of the main layers of the microwave SQUID process.	48
4.1	Photo of the NIST ADR	49
4.2	Schematic of the measurement apparatus for a single pixel.	51
4.3	Photos of the microwave components in an adiabatic demagnetization refrigerator (ADR).	52
4.4	Schematic of the setup for measurement with two tones.	52
4.5	Photo of the open-source electronics.	53
6.1	Diagram of a coplanar waveguide	56
6.2	Photos of interdigitated coupling capacitors	57
6.3	Closeup of one of the bridges connecting the ground planes	57
6.4	Schematic of a parallel first-order gradiometer	58
6.5	Photos of μ mux07a rf SQUIDS	59
6.6	Survey of the μ mux07a resonances.	60

6.7	Variation of a μ mux07a resonance with magnetic flux in the SQUID	61
6.8	Flux noise of a μ mux07a rf SQUID	62
6.9	Demonstration of flux ramp demodulation	63
7.1	Photo of a μ mux09a gradiometric SQUID	66
7.2	Circuit diagram of a directly coupled rf SQUID	67
7.3	FastHenry model of a weak inductive coupling	68
7.4	FastHenry model of a strong inductive coupling	70
7.5	FastHenry model of a variable inductive coupling	71
7.6	Photo of the μ mux09a input filters	72
7.7	Survey of μ mux09a resonances	73
7.8	Variation of a μ mux09a resonance with magnetic flux in the SQUID	74
7.9	Flux noise of a μ mux09a SQUID	75
7.10	Photo of a μ mux09a chip wired to TESs	76
7.11	Noise-equivalent power of a CMB TES, measured with μ mux09a	76
8.1	Photo of an arrangement of trombone resonators	79
8.2	Photo of the elbow coupler in μ mux10b.	79
8.3	Photo of a μ mux10b SQUID	80
8.4	Photo of the μ mux10b input filters	81
8.5	Survey of the μ mux10b resonances	82
8.6	Quality factors for the resonances across a μ mux10b chip	82
8.7	Variation of a μ mux10b resonance with magnetic flux in the SQUID	83
8.8	Variation of two μ mux10b resonances with current through their flux bias lines	84
8.9	Open-loop flux noise of a μ mux10b SQUID	85
8.10	Open-loop frequency noise of a μ mux10b SQUID	86
8.11	Flux ramp that repeatedly sweeps out the SQUID response of all resonators	87
8.12	Illustration of the phase-fitting method	88

8.13 Flux noise after flux-ramp demodulation	88
8.14 Flux ramp demodulation performed with μ mux10b showing linear response.	89
8.15 Difference between applied flux ramp and a perfectly linear ramp.	90
8.16 Measured non-linearity of the flux-ramp modulation scheme	90
8.17 Multiplexed readout of two synthesized flux signals	91
8.18 DC crosstalk of one channel into the other	92
8.19 Photo of a μ mux10b chip wired for readout of several CMB TES chips	92
8.20 Multiplexed readout of two voltage-biased TES's responding to sinusoidal heater signals . . .	93
8.21 Noise-equivalent power of a TES using μ mux10b	94
9.1 The layout for the rf SQUID in μ mux11a.	96
9.2 Open-source software-defined radio solution	97
9.3 A resonator using lumped rather than distributed capacitance and inductance	98
9.4 Two rf SQUIDs coupling to the same quarter-wave resonator	99
9.5 Different SQUIDs produce signals in different sidebands	100
9.6 Hybrid multiplexing	101
9.7 Inversion pattern for a 4-channel Walsh code for CDM	102
B.1 Circuit diagram of an rf-SQUID screening an inductor.	110
B.2 SQUID circuit including leakage resistance and junction capacitance.	111
B.3 Schematic of the rf-SQUID and input coil coupling to both the resonator and each other. . .	112

Chapter 1

Introduction

The Microwave SQUID Multiplexer is a device for the readout of large arrays of low-temperature detectors with a small number of wires. It was motivated by the dramatic growth in array sizes and will provide the necessary multiplexing factors for megapixel arrays of the future.

1.1 Low-Temperature Detectors

Detectors operating at very low temperature[1] have been studied since 1908 when Bottomley[2] cooled a platinum-platinoid thermojunction to the temperature of liquid nitrogen (77 K) and used it to measure thermal radiation from other bodies. Thermal fluctuations are smaller at low temperatures, and detector responsivity is greater[3]. The sensitivity of low-temperature detectors has enabled measurements of the cosmic microwave background, THz imaging for security, optical photon counting for telecommunications, x-ray spectroscopy for materials analysis, γ -ray spectroscopy for nuclear non-proliferation, and more.

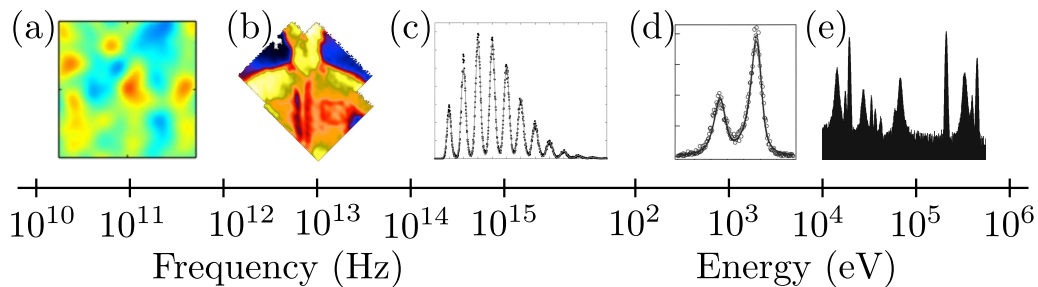


Figure 1.1: Applications of low-temperature detectors span the electromagnetic spectrum: a) Cosmic Microwave Background b) THz imaging c) Optical photon counting d) x-ray spectroscopy e) γ -ray spectroscopy

The first low-temperature detectors were cooled metal strips and thermocouples[2]. In 1941, Andrews used a superconducting film as a “radiometric receiver”[4][5]. In 1957, Boyle cooled a carbon thermocouple and used it to make sensitive measurements of radiation in the far infrared[6]. In 1961, cooled semiconductor detectors were developed and the doped-germanium bolometer[7] became a workhorse of astronomy and particle detection. The past twenty years has seen broad adoption of the superconducting transition-edge sensor[8], and the past ten years has seen work begin on magnetic calorimeters[9][10] and microwave kinetic inductance detectors[11][12]. All of these technologies use low temperature to increase sensitivity.

The Microwave SQUID Multiplexer has been developed in the context of Transition-Edge Sensors and Microwave Kinetic Inductance Detectors.

1.2 Transition-Edge Sensors

A Transition-Edge Sensor (TES) uses the steep change in resistance of a superconducting film at the transition between the superconducting and normal states.

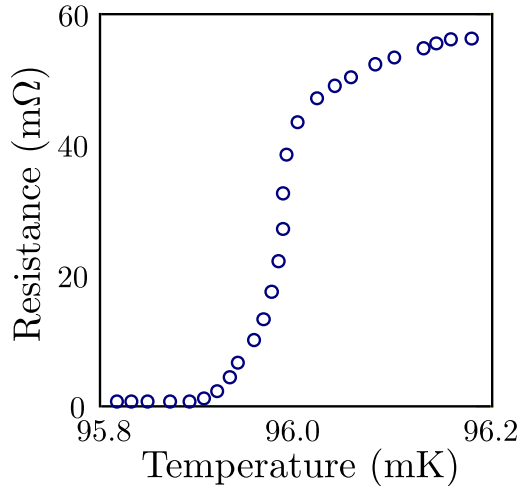


Figure 1.2: Example transition between superconducting and normal states of a transition-edge sensor (TES).

Biased in temperature in its transition, the film acts as an exquisitely sensitive thermometry and can be used to form a TES bolometer or TES calorimeter.

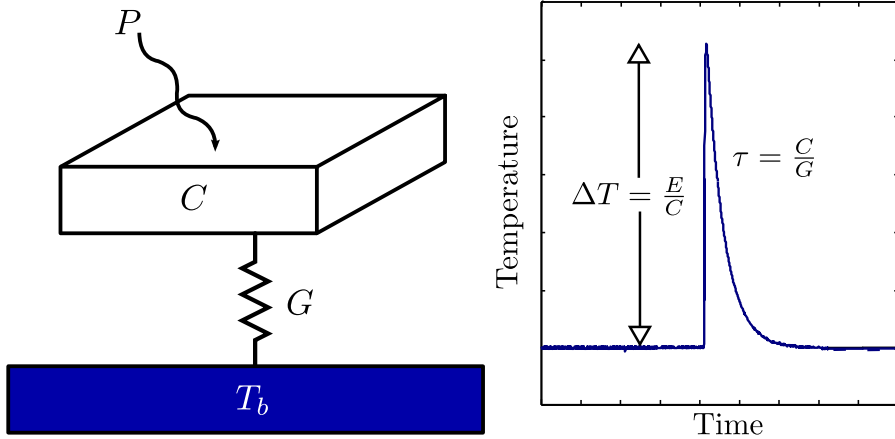


Figure 1.3: Illustration of an ideal bolometer/calorimeter. Incident power heats the floating heat capacity above the temperature of the bath. A pulse of energy causes a pulse in temperature that decays back to equilibrium with the bath.

A *bolometer* consists of an absorber of heat capacity C connected by a weak thermal conductance G to a bath at temperature T_b (Figure 1.3)[13]. Measurement of the temperature of the absorber constitutes a measurement of incident power P because the power heats the absorber to a temperature $T = T_b + \frac{P}{G}$ [14]. The same device is called a *calorimeter* when measuring discrete incident energy E [15][8][16], such that the absorber warms to $T = T_b + \frac{E}{C}$ and returns to the bath temperature with a $\tau = \frac{C}{G}$ time constant.

In a TES bolometer/calorimeter, the superconducting film provides the sensitive thermometry of the floating absorber. These devices achieve world-record power and energy sensitivity across more than nine orders of magnitude in wavelength and energy: CMB[17][18], THz[19], sub-mm[20][21], FIR[22], optical[23], x-ray[24][25], γ -ray[26], and α -particles[27].

We describe the sensitivity of a bolometer by a Noise-Equivalent Power (NEP), the signal power in a 1 Hz bandwidth at which the signal-to-noise is unity. We describe the sensitivity of a calorimeter by an energy sensitivity ΔE , the full width at half maximum of a spectral peak. The noise-equivalent power[28] and energy resolution[15] of TESs are limited by heat fluctuating across the thermal conductance:

$$NEP \approx \sqrt{4k_B T^2 G} \quad (1.1)$$

$$\Delta E \approx 2.35 \sqrt{k_B T^2 C} \quad (1.2)$$

This fluctuation is the thermal analog of Johnson noise in a resistor. TESs therefore benefit greatly from operation at low temperatures (Equations 1.1 and 1.2). For example, a typical TES bolometer used for CMB measurement operates at 300 mK with a thermal conductivity of $G \approx 70 \text{ pW/K}$ and a noise-equivalent power of roughly $2 \times 10^{-17} \text{ W}/\sqrt{\text{Hz}}$. TESs have operated at temperatures as low as 20 mK and many active TES instruments now operate at roughly 100 mK.

Practical Transition-Edge Sensors are voltage-biased[15][29] which keeps them in the transition using the V^2/R self-heating. The self-heating provides negative electro-thermal feedback; as the TES temperature and resistance increase, current through the device and joule-heating decrease. The primary advantage of negative electro-thermal feedback is that it allows TESs with different transition temperatures T_c to operate simultaneously as long as the bath temperature is colder than every T_c . This realization enabled the construction of arrays of TESs. The voltage-biased TES is a low-impedance device, producing a current signal proportional to incident power. The noise power spectral density of this current signal is[15]:

$$S_I = \frac{4k_B T}{R} \left(\frac{(n/\alpha)^2 + (\omega/\omega_{ETF})^2 + n/2}{1 + (\omega/\omega_{ETF})^2} \right) \quad (1.3)$$

where $\alpha \equiv \frac{T}{R} \frac{dR}{dT}$ is a unitless measure of the sharpness of the superconducting transition, $\omega_{ETF} \equiv \frac{G(1+\alpha/n)}{C}$ is the rolloff of the detector response, and n describes the heat loss to the bath $P \propto (T_c^n - T_b^n)$ and can be 4, 5, or 6 depending on the temperature range and physical mechanism of heat exchange. Superconducting films can be made with α as high as 1,000.

The output noise temperature of a TES is therefore between two and three times the transition temperature. For typical TES operating resistance $R_{TES} \approx 1 \text{ m}\Omega$, the current signal is on the order of microamps with fluctuations on the order of $100 \text{ pA}/\sqrt{\text{Hz}}$. Non-degrading detection of such small and quiet currents requires a low-impedance amplifier with low input current noise that can operate at cryogenic temperatures. The Superconducting Quantum Interference Device is the amplifier of choice.

1.3 Superconducting Quantum Interference Devices

In 1962, Brian Josephson observed[30][31] that the supercurrent tunneling through a superconductor-insulator-superconductor junction must be a periodic function of the phase difference between the supercon-

ducting wave-functions on either side of the junction. The Superconducting Quantum Interference Device (SQUID), which consists of a superconducting loop interrupted by one or more Josephson junctions, was invented at Ford labs soon after[32]. The two-junction, or dc-SQUID was invented in 1964[33] and the one-junction, or rf SQUID was invented in 1967[34].

These devices are sensitive to magnetic flux in the loop because the electromagnetic vector potential advances the phase of the superconducting wave function through the Hamiltonian of charged particles[35]:

$$H = \frac{(\mathbf{p} - q\mathbf{A})^2}{2m} - q\varphi \quad (1.4)$$

The superconducting wave function therefore accumulates a 2π phase twist around a loop containing $\Phi_0 = \frac{\hbar}{2e} = 2.068 \times 10^{-15}$ Webers, called the *magnetic flux quantum*[36][37]. A SQUID is a circuit that uses Josephson junctions to detect this phase.

The dc SQUID consists of a superconducting loop interrupted by two resistively-shunted Josephson junctions. Current taps are placed on the loop so that a bias current must flow through one junction or the other. Magnetic flux in the loop changes the relationship between the phase differences at the two junctions, effectively modulating the total tunneling supercurrent that can flow between the taps. When the bias current exceeds the maximum tunneling supercurrent through the two Josephson junctions, the excess current flows through the resistive shunts and generates a fluctuating voltage with a dc component between the current taps. Magnetic flux in the SQUID loop modulates this dc voltage. The low-noise and readout simplicity of dc-SQUIDs has made them the most popular SQUID technology today.

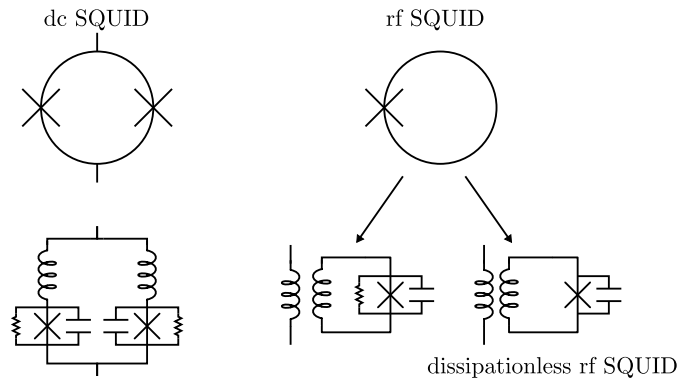


Figure 1.4: Artistic representations and accurate schematics of different SQUIDS.

The standard rf SQUID consists of a superconducting loop interrupted by a single resistively-shunted Josephson junction. Oscillating magnetic flux in the loop dissipates power in the shunt, with the energy dissipation per cycle a function of the mean value of flux. A tank circuit that inductively couples to the SQUID drives ac flux in the SQUID loop to measure this dissipation. These rf SQUIDs generally have higher noise than dc-SQUIDs and require ac readout, but were popular before the development of methods to reliably fabricate multiple Josephson junctions.

The dissipationless rf SQUID in the Microwave SQUID Multiplexer consists of a superconducting loop interrupted by a single unshunted Josephson junction. For small flux oscillations, the SQUID behaves like a loop whose self-inductance depends on the mean value of flux. We inductively couple this SQUID to a microwave resonator so that mean flux in the SQUID shifts the resonance frequency. We call these SQUIDs “dissipationless” because their readout method does not rely on loss. Although these SQUIDs are not actually dissipationless due to sub-gap resistance and the loss tangent of the junction dielectric, in practice they dissipate very little power. We work out the theory of these SQUIDs in section 2.1.

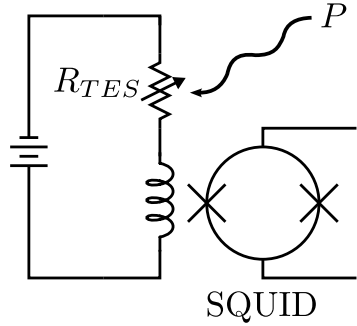


Figure 1.5: Schematic of dc-SQUID readout of a voltage-biased TES.

To measure a TES, we direct the signal current through an inductor that couples magnetic flux into the SQUID (Figure 1.5). SQUIDs typically have flux noise of order $1 \mu\Phi_0/\sqrt{\text{Hz}}$ so a coupling as low as $M \approx 50 \text{ pH}$ is sufficient to give a current noise ($40 \text{ pA}/\sqrt{\text{Hz}}$) well below the output current noise of most TES designs. SQUIDs are therefore ideal amplifiers for TESs, and naturally operate at cryogenic temperatures. They have been used for TES readout for the past twenty years[38].

1.4 Arrays and Multiplexing

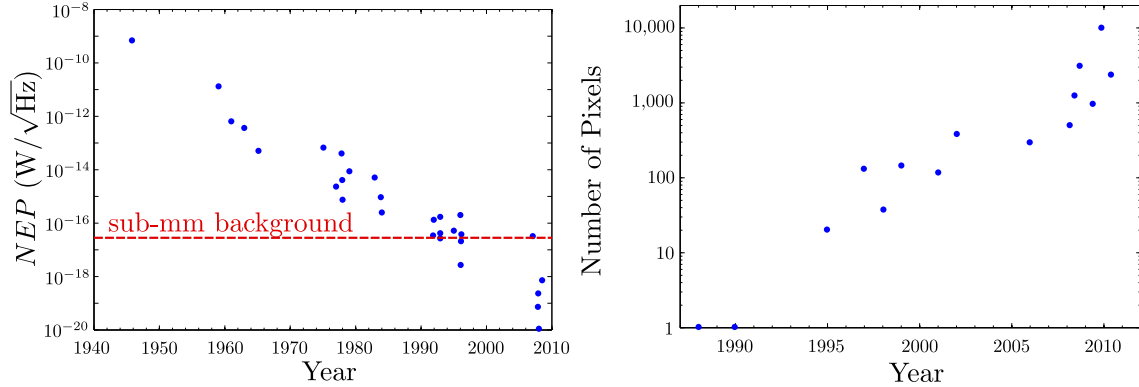


Figure 1.6: Improvement in sensitivity of low-temperature detectors and growth in number of detectors per instrument.[39] The red line shows a typical background noise for ground-based observations in the sub-mm.

The sensitivity of low-temperature detectors has improved dramatically over the past few decades to the point where many applications are limited by other factors. For example, ground-based observations in the sub-mm are limited by shot noise from atmospheric absorption (Figure 1.6 left) and x-ray spectra are limited by the natural width of the underlying emission lines. To continue accessing new science, increasingly large arrays of detectors have been developed (Figure 1.6 right).

One difficulty posed by low-temperature detector arrays is that of large wire counts between room temperature and the cryogenic stage, which add heat load and cryogenic complexity. We therefore multiplex the detector signals onto a smaller number of wires. Most existing TES arrays use either time-division SQUID multiplexing or frequency-division TES multiplexing schemes.

Time-division multiplexing (TDM) consists of multiple input signals taking turns on an output channel. To satisfy the Nyquist-Shannon sampling theorem[40], the multiplexer must return to each channel with a frequency at least twice the bandwidth of the input channel. Time-division SQUID multiplexing[41][42] switches between dc-SQUIDs by applying bias current to one SQUID at a time. The outputs of all the “first-stage” SQUIDs are summed into a “second-stage” SQUID that amplifies the combined signals onto a single output channel. With n current bias lines and m output channels this technique allows measure-

ment of $n \times m$ detectors with $O(n + m)$ wires. The majority of existing TES arrays[43][44][21][45][26] use time-division SQUID multiplexing.

Frequency-division multiplexing (FDM) consists of modulating multiple input signals at different frequencies on the same output channel[46][47][48]. Frequency-division TES multiplexing uses cold filter circuits to apply a different oscillating voltage bias to each TES. The TES currents are summed into a common SQUID amplifier. The detector signals appear in sidebands of the bias frequencies which must therefore be spaced by more than the expected bandwidth of input signals. Many existing instruments[49][50][51] use frequency-division TES multiplexing.

Code-division multiplexing uses an orthogonal basis set intermediate between time-division and frequency-division. Like time-division multiplexing, readout is broken into multiple timeslots, but unlike time-division multiplexing the signals from all pixels are summed in each timeslot. To allow separation of the input signals, the weight of different input signals changes between timeslots. For example, in a two pixel device the first timeslot could sum the signals and the second timeslot could take the difference. Development of practical code-division SQUID multiplexing is just beginning[52][53].

Information theory limits the maximum possible multiplexing factor N with any of these multiplexers to the ratio of the input channel capacity to the output channel capacity, where channel capacity is defined by Shannon[54][40][55] as:

$$C = \int_0^{BW} \log_2 (1 + (SNR)^2) df \quad (1.5)$$

and has units of bits per second (bps).

A single pixel for the CMB application I will discuss has a dynamic range of 5 pW, a photon shot noise of 4×10^{-17} W/ $\sqrt{\text{Hz}}$, and a bandwidth of 100 Hz. It therefore requires 2.7 kbps of channel capacity for lossless readout. An open-loop SQUID has a linear range of approximately Φ_0/π , a flux noise of $1\mu\Phi_0/\sqrt{\text{Hz}}$, and a bandwidth of a few MHz, providing roughly 100 Mbps of channel capacity. A perfectly efficient multiplexer could therefore read out 40,000 CMB TESs on a single SQUID-amplified output channel.

It is practically difficult to approach the theoretical limits of a multiplexer in an analog system. The maximum multiplexing factor achieved so far with time-division SQUID multiplexing is 40 and the maximum with frequency-division TES multiplexing is 7. Neither multiplexing solution seems likely to provide the

multiplexing factors that will be necessary in the next decade.

1.5 Microwave Kinetic Inductance Detectors

The Microwave Kinetic Inductance Detector (MKID) is a low-temperature detector that approaches the photon noise limit in the sub-mm. Although it does not have the sensitivity of TESs at all wavelengths, it provides elegant large-scale multiplexability[12][56][11][57][58]. An MKID consists of a superconducting strip integrated in a microwave resonator. Incident radiation breaks Cooper pairs in the superconductor, changing the surface impedance of the strip, which in turn changes the resonance frequency and quality factor of the resonator (Figure 1.7).

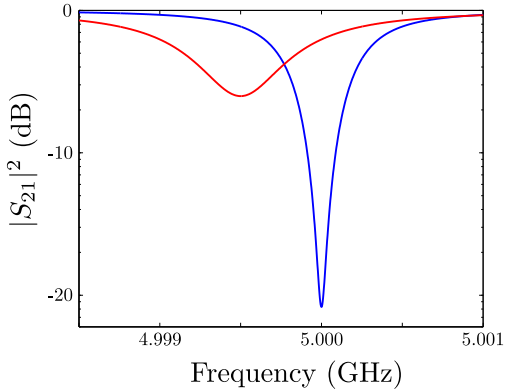


Figure 1.7: Change in transmitted power $|S_{21}|^2$ as a function of frequency for a microwave kinetic-inductance detector. Pair-breaking radiation transforms the blue curve into the red curve.

A large number of superconducting microwave resonators can be fabricated on a single chip or wafer (Figure 1.8). Non-overlapping resonances can be read out simultaneously by measuring the complex transmission of a superposition of microwave tones. Only two coaxial cables are therefore necessary between the cryogenic device and room temperature. This technology was enabled by the development of a cryogenic microwave amplifier called a high electron-mobility transistor[59] (HEMT) with a 10 GHz bandwidth, a saturation power of -40 dBm, and a noise temperature of roughly 5 K, implying a channel capacity of 300 Gbps. Even inefficient use of this channel capacity should allow practical multiplexing factors in the thousands.

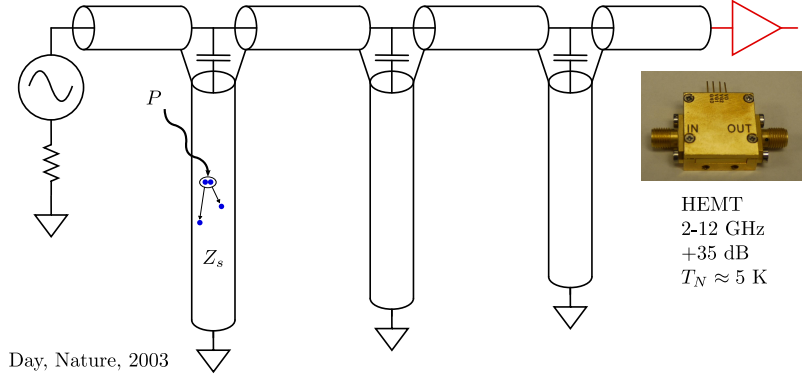


Figure 1.8: Schematic of a three-pixel MKID device, representing the detectors as quarter-wave resonators.

Recent work on MKIDs[60][61] and the remarkable channel capacity of the HEMT inspired the development of the Microwave SQUID Multiplexer.

1.6 Microwave SQUID Multiplexer

The Microwave SQUID Multiplexer is an attempt to combine the sensitivity of TESs across a wide range of applications with the multiplexability of MKIDs, and may allow even larger multiplexing factors in combination with other multiplexing technologies (Section 9.5.2).

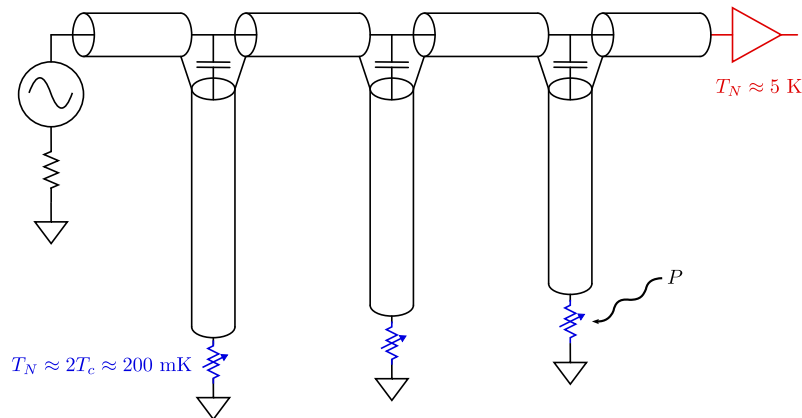


Figure 1.9: Schematic of a three-pixel device with transition-edge sensors modulating the Q of microwave resonators. The HEMT noise dominates the TES noise.

A natural first thought is the simple inclusion of TESs in the microwave resonant circuit (Figure 1.9). Unfortunately, TESs do not retain their sensitivity in microwave resonant circuits with a HEMT amplifier because of the mismatch between the input noise temperature of the HEMT ($T_N \approx 5$ K) and the output noise temperature of the TESs ($T_N \approx 2T_c \approx 200$ mK). We therefore use SQUIDs to provide gain between the TESs and the resonators sufficient to elevate the TES noise above the HEMT noise.

The Microwave SQUID Multiplexer couples SQUIDs to superconducting microwave resonators (Figure 1.10). An early device[62] used dc-SQUIDs to modulate the Q of the resonators, but current devices use the change in inductance of dissipationless rf SQUIDs to modulate the resonance frequencies[63][64]. The magnetic flux in thousands of SQUIDs, each modulating a distinct microwave resonance, can then be measured with a pair of coaxial cables.

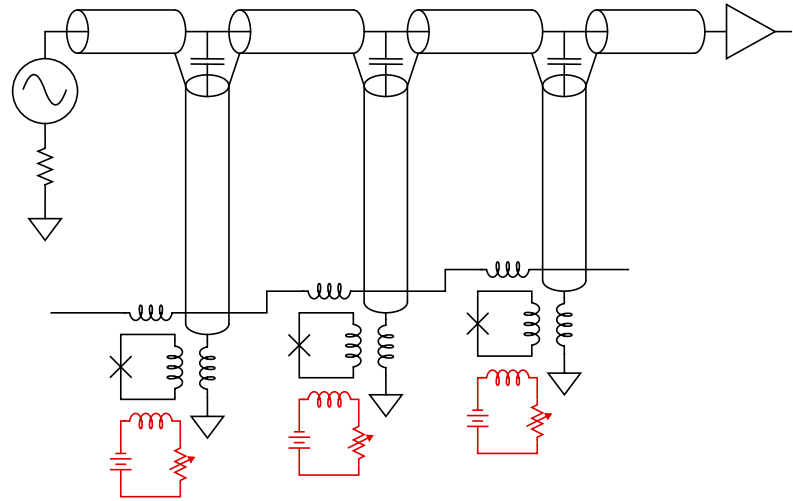


Figure 1.10: Schematic of a three-pixel device with rf SQUIDs providing gain between TESs and microwave resonators. A common flux-bias line is used to linearize all the SQUIDs (Sections 2.6, 6.3.4 and 8.2.4).

By contrast with MKIDs, the Microwave SQUID Multiplexer allows independent optimization of the multiplexer and detectors and use of the same multiplexer design with many different detectors. The SQUID amplifier enables modulation of the detector signal to avoid low-frequency noise in the resonators and HEMT. Finally, the Microwave SQUID Multiplexer does not degrade the sensitivity of the TES detectors, making it

useful for a wide range of cutting-edge scientific applications.

This thesis explores the theory, design, and experimental results of the Microwave SQUID Multiplexer. We discuss the predicted and observed flux noise in Sections 2.5, 6.3.3, 7.3.3, and 8.2.3. We discuss the linearization of SQUID readout with *flux-ramp modulation* in Sections 2.6, 6.3.4, and 8.2.4. We conclude by considering the compatibility of the Microwave SQUID Multiplexer with hybrid multiplexing schemes in Section 9. Hybrid multiplexing could potentially achieve Shannon efficiencies that allow read out of a megapixel array with a handful of coaxial cables and twisted pairs.

Let us justify this work by considering a few scientific applications that will require large multiplexed arrays.

1.7 Bolometric Applications

Instruments with TES bolometers currently perform astronomy in the microwave, sub-mm, terahertz, and far infrared, as well as terrestrial terahertz imaging, providing unsurpassed sensitivity in each band. There are too many applications of TES bolometers to accurately describe each, so we will focus on one of the most compelling: the measurement of the polarization of the cosmic microwave background (CMB).

After the inflationary epoch the universe consisted of a hot, dense plasma in thermal equilibrium with a black body population of photons[65]. When the universe cooled enough to form neutral hydrogen (3000 K) the photons began to propagate without scattering. They have since redshifted into the microwave region of the spectrum, with a peak frequency of 160.2 GHz corresponding to a temperature of 2.725 K.

A variety of mechanisms of scientific interest have slightly polarized the CMB. The polarization varies across the sky and can be broken into two parts, a tensor curl-less or *E-mode* component, and a tensor divergence-less or *B-mode* component. Primordial gravity waves from inflation impart a B-mode polarization signature on the CMB[66]. The B-mode polarization component due to primordial gravity waves is expected to be no more than 100 nK (Figure 1.11)[67], but its detection would confirm theories of inflation in the early universe and thus has great scientific importance.

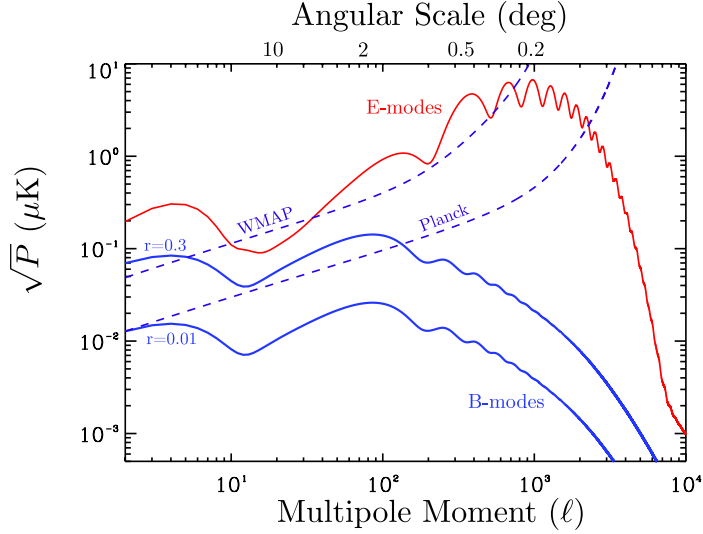


Figure 1.11: E-mode and B-mode components of the cosmic microwave background[67].

The two primary terrestrial observing sites for CMB astronomy are the Atacama desert in Chile[68][18] and the south pole[69][50][70]. At the south pole the noise-equivalent temperature (*NET*) is $200 \mu\text{K}\sqrt{\text{s}}$ in the 150 GHz band and higher for higher frequency observing windows on the CMB[70].

The search for inflationary B-modes requires observation of a large area of sky from low multipole moment $\ell \approx 2$ to $\ell \approx 100$. Surveying a hemisphere to that angular resolution with a single pixel would take many hundreds of years. Therefore new instruments[71][72] for this work are being designed with tens of thousands of pixels. These instruments require large-scale multiplexing solutions.

1.8 Spectroscopic Applications

Instruments with TES calorimeters currently perform optical photon counting for telecommunication applications, x-ray spectroscopy for materials analysis, imaging x-ray spectroscopy for astronomy, γ -ray spectroscopy for nuclear materials analysis, and α -particle spectroscopy for nuclear forensics, providing record non-dispersive resolution in all of these applications.

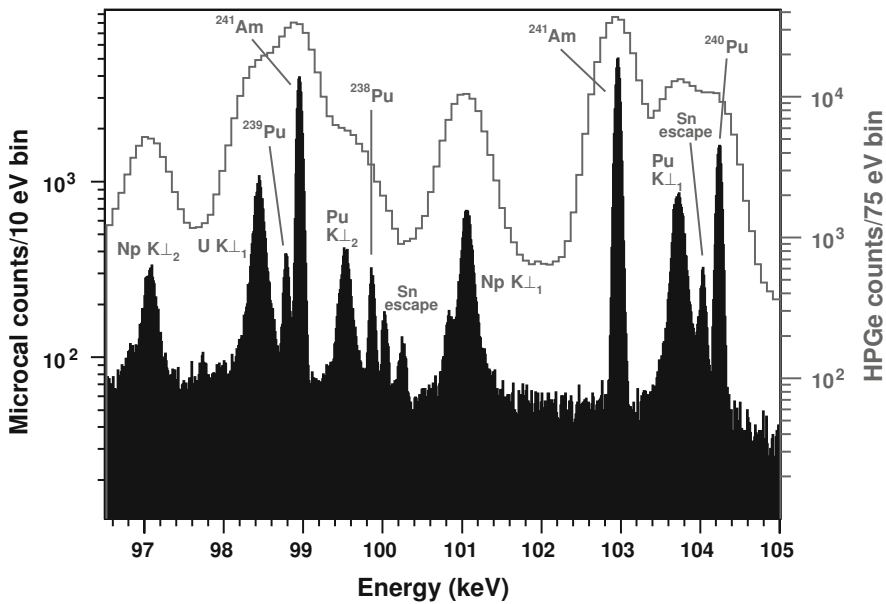


Figure 1.12: Spectra of a plutonium sample using a state-of-the-art high-purity germanium detector (grey line) and a TES microcalorimeter (solid black). (Andrew Hoover, LANL)

One compelling application is the non-destructive assay of nuclear materials for nuclear non-proliferation and treaty verification. TES microcalorimeters can distinguish between the nearby peaks of ^{238}Pu , ^{239}Pu , ^{240}Pu , and ^{241}Pu (Figure 1.12) which a doped-germanium detector cannot. The ratio of ^{240}Pu to ^{239}Pu in nuclear fuel provides important evidence of whether it is being used to generate power or make weapons.

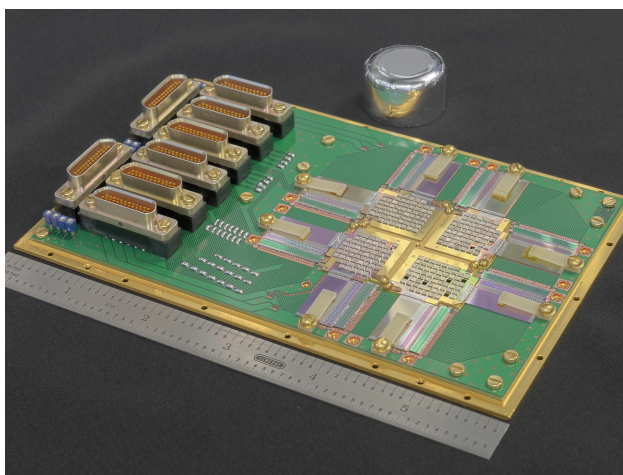


Figure 1.13: TES microcalorimeter array with 256 pixels and HPGe detector of similar collection area.

For these TES calorimeters to achieve much better resolution than other detector technologies they must have less collection area per pixel ($\Delta E \propto \sqrt{C} \propto \sqrt{V}$). To increase the count rate we therefore assemble arrays of detectors (Figure 1.13) which require multiplexed readout. In the future we desire arrays of hundreds or even thousands of TES microcalorimeters.

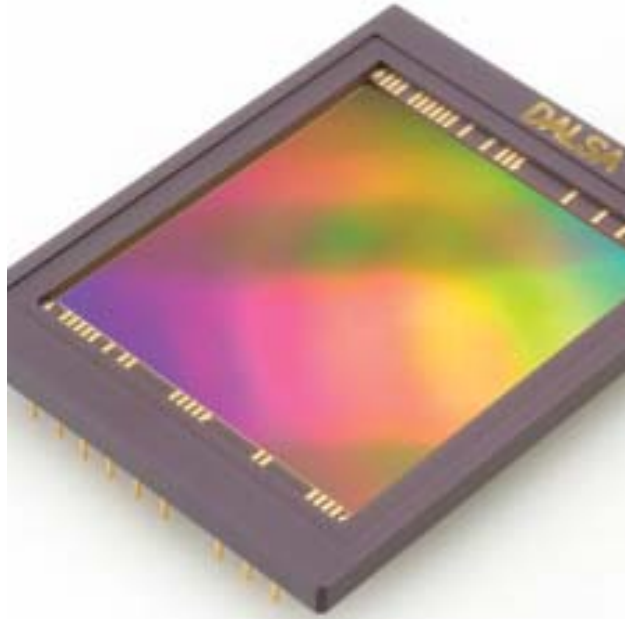


Figure 1.14: Megapixel x-ray CCD camera. (DALSA IA-DJ-01044)

Figure 1.14 shows a megapixel x-ray camera using CCDs. These devices are used for x-ray astronomy, crystallography, microscopy, plasma studies, medical imaging, and more, but have no spectroscopic capability. A similar device where each pixel can perform high-resolution spectroscopy would revolutionize x-ray astronomy and many other fields. This is the scale that we aspire to enable with the Microwave SQUID Multiplexer.

Chapter 2

Theory

This section will explore the physical and electrical theory of the Microwave SQUID Multiplexer circuit shown in Figure 2.1. Each input channel consists of a dissipationless rf SQUID coupled to a superconducting quarter-wave resonator. The input channels are combined into a common output channel by capacitive coupling to a microwave feedline.

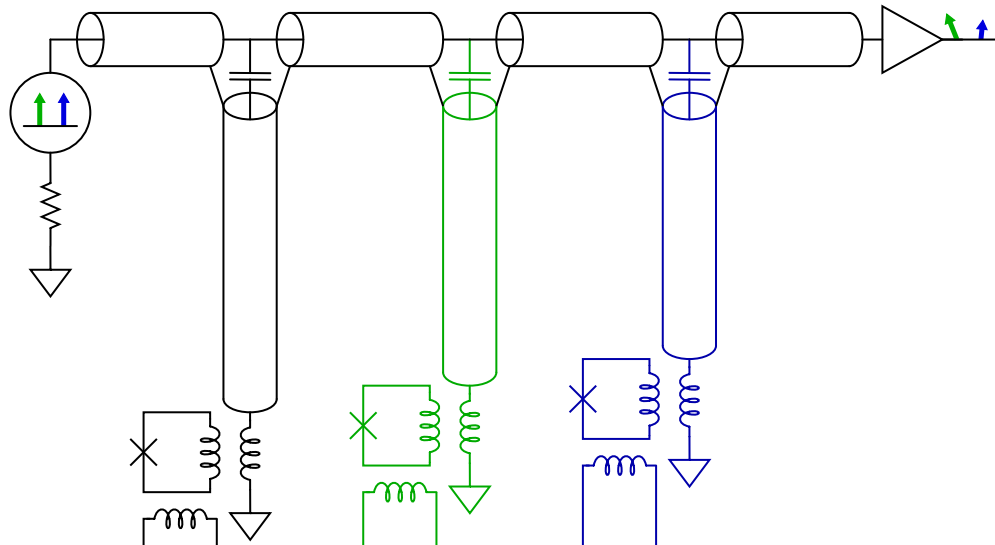


Figure 2.1: Circuit schematic of the Microwave SQUID Multiplexer. Current on the input coil of a SQUID-resonator pair modulates the transmitted amplitude and phase of a microwave tones on-resonance with the resonator.

We will derive the flux-variable resonance frequency of a SQUID-coupled resonator and the corresponding modulation of the transmission of an on-resonance probe tone. We will match the resonance frequency shift to the resonance bandwidth and derive the optimal readout power. We will conclude with a noise theory that predicts the noise referred to flux in the SQUID.

2.1 Dissipationless rf SQUID

We use a dissipationless rf SQUID[73][74] to transduce a change in current in an input coil into a change in inductive load of a microwave resonator. The SQUID consists of a superconducting loop interrupted by an insulating tunnel barrier, called a *Josephson junction*[30].

2.1.1 Josephson Junction Inductance

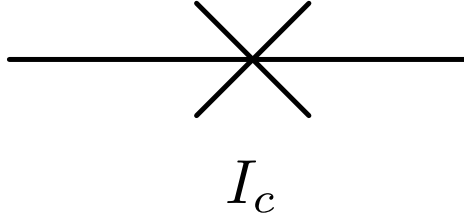


Figure 2.2: Schematic representation of a Josephson Junction.

The tunneling supercurrent across a Josephson junction (Figure 2.2) depends on the difference in phase of the superconducting wave function between the two sides of the junction[30][74]:

$$\boxed{I = I_c \sin \phi} \quad (2.1)$$

where I_c is the so-called *critical current* of the junction and ϕ is the phase difference across the junction.

A voltage drop across the junction makes the phase evolve faster on the high-voltage side than on the low-voltage side. Therefore the phase difference across the junction evolves in time:

$$\boxed{\frac{d\phi}{dt} = \frac{2eV}{\hbar}} \quad (2.2)$$

These two equations are called the *Josephson relations* and have been verified by experiment[31]. In combination, they imply an effective self-inductance of the junction. Near any particular value of ϕ the rate of change of current through the junction is:

$$\frac{dI}{dt} = I_c \cos(\phi) \frac{d\phi}{dt} \quad (2.3)$$

$$= I_c \cos(\phi) \frac{2eV}{\hbar} \quad (2.4)$$

which implies

$$V = \frac{\hbar}{2eI_c \cos(\phi)} \frac{dI}{dt} \quad (2.5)$$

This voltage-current relation describes an effective inductance called the *Josephson inductance*:

$L(\phi) = L_J \sec(\phi)$

where $L_J \equiv \frac{\hbar}{2eI_c} = \frac{\Phi_0}{2\pi I_c}$

(2.6)

where $\Phi_0 = \frac{\hbar}{2e} \approx 2 \times 10^{-15}$ Webers is the quantum of magnetic flux. We can adjust I_c to achieve different values of L_J . Note that this relation holds only for small oscillations in ϕ .

2.1.2 Non-hysteretic rf SQUIDS

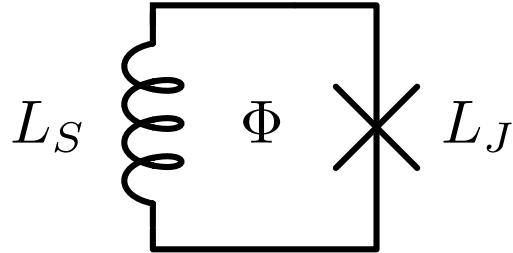


Figure 2.3: Schematic representation of an rf SQUID.

An rf SQUID consists of a superconducting loop interrupted by a single Josephson Junction as shown in Figure 2.3. The phase difference across the junction is initially $\phi = 0$ and evolves with magnetic flux as:

$$\phi = \frac{2e}{\hbar} \int \frac{d\Phi}{dt} dt \quad (2.7)$$

$$= \frac{2e\Phi}{\hbar} \quad (2.8)$$

$$= 2\pi \frac{\Phi}{\Phi_0} \quad (2.9)$$

Because the loop has a self inductance L_S the same current that tunnels across the junction also drives magnetic flux the loop and therefore magnetic flux in the loop Φ is not in general a single-valued function of externally applied magnetic flux Φ_e .

$$\Phi_e = \Phi - I_c L_S \sin\left(2\pi \frac{\Phi}{\Phi_0}\right) \quad (2.10)$$

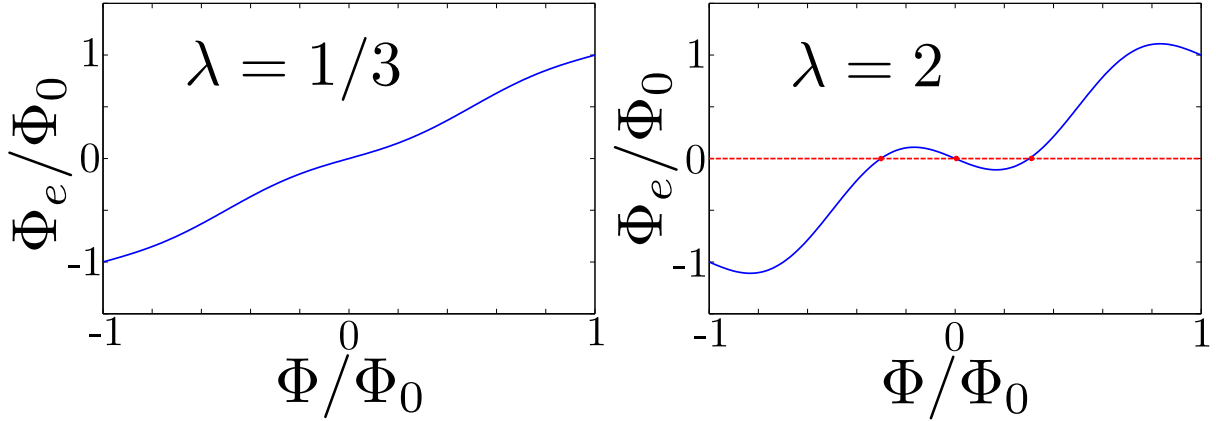


Figure 2.4: Relationship between externally applied and total magnetic flux for two values of $\lambda \equiv L_S/L_J$.

When $\lambda > 1$ the total flux may have multiple acceptable values for a given value of applied flux.

To avoid hysteresis the total flux must be a single-valued function of the applied flux. Therefore $\Phi_e(\Phi)$ must be monotonic.

$$0 < \frac{d\Phi_e}{d\Phi} \quad (2.11)$$

$$< 1 - I_c L_S \cos\left(2\pi \frac{\Phi}{\Phi_0}\right) \frac{2\pi}{\Phi_0} \quad (2.12)$$

$$< 1 - \frac{2\pi I_c L_S}{\Phi_0} \quad (2.13)$$

$$< 1 - \frac{L_S}{L_J} \quad (2.14)$$

We define $\lambda \equiv L_S/L_J$. When $\lambda < 1$, the rf SQUID is non-hysteretic and when $\lambda > 1$, the rf SQUID is hysteretic and can perform flux jumps between metastable states (Figure 2.4). A resistive shunt of the junction is necessary to make these transitions predictable. Most rf SQUIDs use resistive shunts, but we

desire a dissipationless SQUID to minimize the heat load in a large array and therefore operate without shunts, targeting $\lambda \approx 1/3$.

2.1.3 Measuring the SQUID Inductance

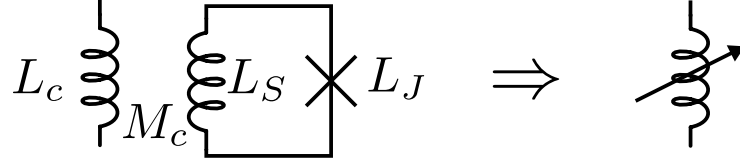


Figure 2.5: Circuit diagram of an rf SQUID screening another inductor.

To read out the SQUID we use it to screen an inductor in another circuit (Figure 2.5). The other inductor therefore has an effective self-inductance variable with flux in the SQUID (Appendix B):

$$L(\Phi) = L_c - \frac{M_c^2}{L_S + L_J \sec(2\pi\Phi/\Phi_0)} \quad (2.15)$$

$$= L_c - \frac{M_c^2}{L_S} \frac{\lambda \cos(2\pi\Phi/\Phi_0)}{1 + \lambda \cos(2\pi\Phi/\Phi_0)} \quad (2.16)$$

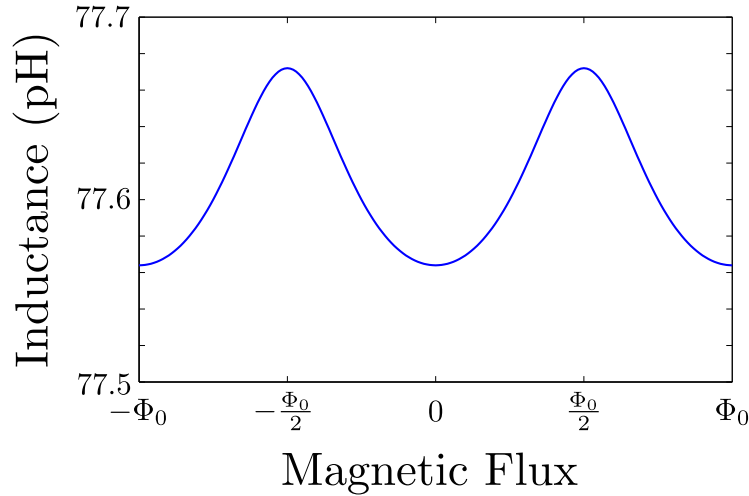


Figure 2.6: Flux variable inductance of the termination for $L_c = 77.6$ pH, $M_c = 1.65$ pH, $L_S = 18.9$ pH, and $\lambda = 1/3$. These values come from the design in Section 7.1.5.2.

For small values of λ this looks like a nearly cosinusoidal function of flux (Figure 2.6). The peak-to-peak change in inductance is:

$$L_{pp} = \frac{M_c^2}{L_S} \left(\frac{1}{1 + \lambda^{-1}} - \frac{1}{1 - \lambda^{-1}} \right) \quad (2.17)$$

$$= \frac{M_c^2}{L_S} \frac{2\lambda^{-1}}{\lambda^{-2} - 1} \quad (2.18)$$

$$= \frac{M_c^2}{L_S} \frac{2\lambda}{1 - \lambda^2} \quad (2.19)$$

We are particularly interested in the rate of change of inductance with respect to flux because it determines the SQUID gain:

$$\frac{dL}{d\phi} = \frac{M_c^2}{L_S} \frac{-\lambda \sin(\phi) (1 + \lambda \cos(\phi)) + \lambda \sin(\phi) (\lambda \cos(\phi))}{(1 + \lambda \cos(\phi))^2} \quad (2.20)$$

$$= -\frac{M_c^2}{L_S} \frac{\lambda \sin(\phi)}{(1 + \lambda \cos(\phi))^2} \quad (2.21)$$

The maximum rate of change of inductance at small λ occurs at $\phi = \pi/2$ and is:

$$\boxed{\frac{dL}{d\phi}_{max} = -\frac{\lambda M_c^2}{L_S}}$$

(2.22)

2.1.4 Junction Resistance and Capacitance

Real Josephson junctions have some capacitance C_J and leakage resistance R_{sg} which shunt the junction inductance (Figure 2.7). Typical values of SQUID and junction inductance are $L_S \approx 20 \text{ pH}$ and $L_J \approx 60 \text{ pH}$. From the junction thickness and area we predict a parallel-plate capacitance of $C_J \approx 100 \text{ fF}$. The SQUID therefore resonates at between 90 and 130 GHz depending on the mean junction phase, far above our measurement frequency between 4 and 8 GHz. This resonance will only see the harmonics generated by the extreme high order terms of the junction non-linearity, and should not affect our measurements.

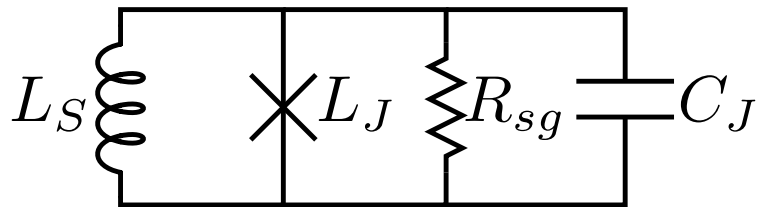


Figure 2.7: SQUID circuit including leakage resistance and junction capacitance.

The effective load impedance of L_S in a series loop with the parallel combination of the other three components (Appendix B.1) is simply:

$$Z_{\text{eff}} \approx i\omega \left(L_c - \frac{M_c^2}{L_S + L_J \sec \phi} \right) + \frac{(\omega M_c)^2 (i\omega C_J + 1/R)}{(1 + \lambda \cos \phi)^2} \quad (2.23)$$

For typical SQUIDs, the variation in effective load reactance due to the junction capacitance is therefore less than 5% of the variation due to junction inductance.

In similar junctions we measure leakage resistance of $R_{sg} \approx 100 \Omega$. For inductive coupling of $M_c \approx 1 \text{ pH}$, this adds a real component of less than $50 \mu\Omega$ to the effective load impedance, which we shall see limits internal Q (Section 2.4.3) to roughly one million. This loss is substantially smaller than other losses we will consider in Section 2.4.

These shunts do not substantially change the flux screening behavior of the SQUID or increase the loss. For simplicity, we therefore neglect C_J and R_{sg} in the rest of the analysis.

2.2 Resonance Frequency

To multiplex the SQUIDs in frequency space, we couple each SQUID to a different resonator with a unique resonance frequency. We therefore had to design resonators to resonate at microwave frequencies and adjust resonator parameters to prevent overlap of resonances. Let us begin with the quarter-wave resonator and then extend our analysis, first by capacitive coupling to the readout circuit, and then by inductive coupling to the input circuit.

2.2.1 Ideal Quarter-Wave Resonator

The ideal quarter-wave resonator is a dissipationless transmission line that is open at one end and shorted at the other (Figure 2.8). No current flows at the open end. No voltage exists at the shorted end. The only standing waves that can match these boundary conditions are those for which $(2n+1)\frac{\lambda}{4} = l$, where l is the length of the transmission line.

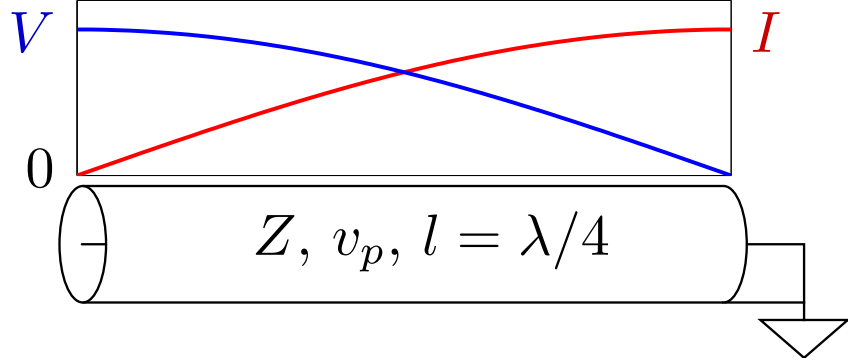


Figure 2.8: Illustration of voltage and current along a perfect quarter-wave resonator.

For a length l of transmission line of phase velocity v_p the frequency of the first mode is:

$$f_1 = \frac{v_p}{4l} \quad (2.24)$$

where we refer to the resonance frequency as f_1 in anticipation of using f_0 as the resonance frequency of the complete circuit with feedline and rf SQUID. More precisely, voltage and current waves of frequency ω on a transmission line with phase velocity v_p propagate as:

$$V(z) = V_0^+ e^{-i\beta z} + V_0^- e^{i\beta z} \quad (2.25)$$

$$I(z) = \frac{V_0^+}{Z_1} e^{-i\beta z} - \frac{V_0^-}{Z_1} e^{i\beta z} \quad (2.26)$$

where $\beta \equiv \frac{\omega}{v_p}$. Since the transmission line shorts to ground at $z = 0$ we have

$$V(0) = V_0^+ + V_0^- = 0 \quad (2.27)$$

$$I(0) = \frac{V_0^+}{Z_1} - \frac{V_0^-}{Z_1} \equiv I, \quad (2.28)$$

where I is the magnitude of the current oscillation at the shorted end of the quarter-wave transmission line. This implies a standing wave configuration of fields within the transmission line:

$$V(z) = -iIZ_1 \sin(\beta z) \quad (2.29)$$

$$I(z) = I \cos(\beta z) \quad (2.30)$$

Note that the voltage and current are $\pi/2$ out of phase.

2.2.2 Capacitive Coupling

To couple the quarter-wave resonator to the external world we replace the open with a small capacitance C_c to the center conductor of another transmission line (Figure 2.9).

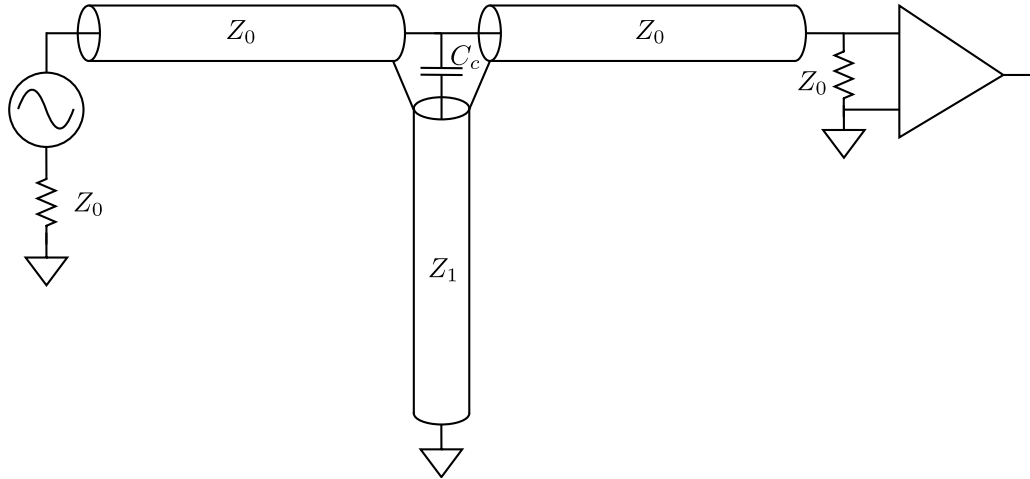


Figure 2.9: Circuit diagram of a quarter-wave resonator capacitively coupled to a microwave feedline.

The resonance frequency of this structure is the frequency at which the capacitively coupled resonator presents an effective short to the feedline. This occurs at the frequency where the reactance of the coupling capacitor exactly cancels the reactance of the quarter-wave transmission line. A length of lossless transmission line transforms a load impedance (Figure 2.10) as follows[75]:

$$Z = Z_1 \frac{Z_L + iZ_1 \tan\left(\omega \frac{l}{v_p}\right)}{Z_1 + iZ_L \tan\left(\omega \frac{l}{v_p}\right)}. \quad (2.31)$$

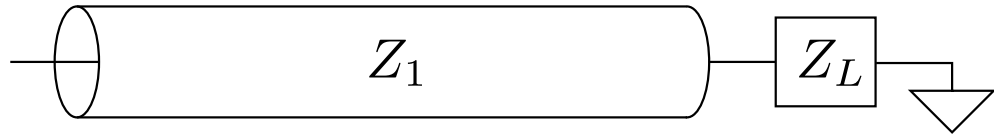


Figure 2.10: A length of transmission line, terminated with a load impedance.

For a shorted quarter-wave transmission line the transformed impedance is simply

$$Z = iZ_1 \tan\left(\omega \frac{l}{v_p}\right). \quad (2.32)$$

This impedance is in series with the impedance of the coupling capacitor. The resonance condition is thus:

$$0 = \frac{1}{i\omega_0 C_c} + iZ_1 \tan\left(\omega_0 \frac{l}{v_p}\right), \quad (2.33)$$

which means that the resonance frequency must satisfy

$$\omega_0 C_c Z_1 = \cot\left(\omega_0 \frac{\pi}{2\omega_1}\right) \quad (2.34)$$

where $\omega_1 = \frac{\pi v_p}{2l}$ is the resonance frequency of the uncoupled resonator. This equation is transcendental but can be solved for small $\omega_0 C_c Z_1$ by expanding the cotangent around $\pi/2$.

$$\omega_0 C_c Z_1 = \cot\left(\frac{\pi}{2} + \frac{\pi}{2\omega_1}(\omega_0 - \omega_1)\right) \quad (2.35)$$

$$= 0 - \frac{\pi}{2\omega_1}(\omega_0 - \omega_1) + O((\omega_0 - \omega_1)^2) \quad (2.36)$$

$$2\omega_0 \omega_1 C_c Z_1 / \pi \approx \omega_1 - \omega_0 \quad (2.37)$$

$$\omega_0 (1 + 2\omega_1 C_c Z_1 / \pi) \approx \omega_1 \quad (2.38)$$

$$\omega_0 \approx \frac{\omega_1}{1 + 2\omega_1 C_c Z_1 / \pi}. \quad (2.39)$$

Therefore the loaded resonance frequency is close to the quarter-wave resonance frequency but reduced by the coupling capacitor:

$$f_0 = \frac{f_1}{1 + 4f_1 C_c Z_1} \quad (2.40)$$

When weak capacitance $C_c \ll 1/4f_0 Z_1$ couples the resonators to the feedline, $f_0 \approx f_1$ and we can design for any resonance spacing using only the physical length of the resonators.

2.2.3 Inductive Load

We now consider the inductively coupled rf SQUID termination at the other end of the quarter-wave resonator (Figure 2.11). A change in the flux coupled to the SQUID changes the SQUID inductance, and therefore the parameters of the resonator, including particularly the resonance frequency. A resonator may thus be used to measure the flux in the SQUID.

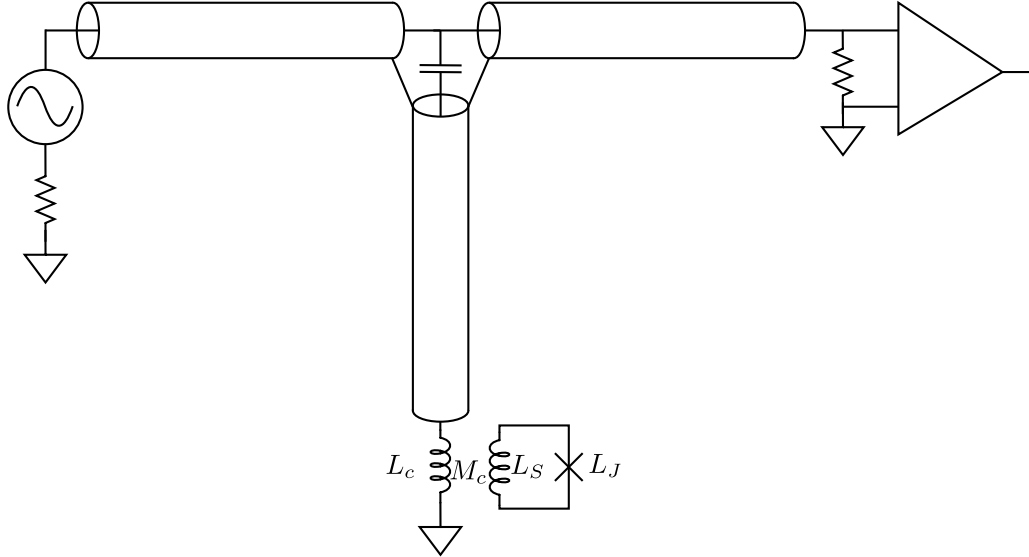


Figure 2.11: A quarter-wave resonator coupled to a microwave feedline and loaded by an inductor screened by an rf SQUID.

$$0 = \frac{1}{i\omega_0 C_c} + Z_1 \frac{i\omega_0 L \cot(\omega_0 \frac{l}{v_p}) + iZ_1}{Z_1 \cot(\omega_0 \frac{l}{v_p}) - \omega_0 L} \quad (2.41)$$

$$= (\omega_0 C_c Z_1) \left(\omega_0 L \cot\left(\omega_0 \frac{l}{v_p}\right) + Z_1 \right) - Z_1 \cot\left(\omega_0 \frac{l}{v_p}\right) - \omega_0 L \quad (2.42)$$

Expanding around the quarter-wave resonance frequency \$\omega_1\$:

$$0 = \omega_1^2 LC_c Z_1 \left(\frac{\pi}{2} - \frac{\pi\omega_0}{2\omega_1} \right) + \omega_0 C_c Z_1^2 - Z_1 \left(\frac{\pi}{2} - \frac{\pi\omega_0}{2\omega_1} \right) - \omega_0 L \quad (2.43)$$

$$= \omega_1^2 LC_c \left(1 - \frac{\omega_0}{\omega_1} \right) + 2\omega_0 C_c Z_1 / \pi - \left(1 - \frac{\omega_0}{\omega_1} \right) - 2\omega_0 L / \pi Z_1 \quad (2.44)$$

$$= \frac{\omega_0}{\omega_1} (1 + 2\omega_1 C_c Z_1 / \pi + 2\omega_1 L / \pi Z_1 - \omega_1^2 LC_c) - 1 + \omega_1^2 LC_c \quad (2.45)$$

Therefore the adjusted resonance frequency is close to the quarter-wave resonance frequency but reduced by both the coupling capacitor and the load inductor.

$$\frac{\omega_0}{\omega_1} = \frac{1 - \omega_1^2 LC_c}{1 + 2\omega_1 C_c Z_1 / \pi + 2\omega_1 L / \pi Z_1 - \omega_1^2 LC_c} \quad (2.46)$$

Since we will design the coupling capacitor so that $\frac{1}{\omega_1 C_c} \gg Z_1$ and the load inductor so that $\omega_1 L \ll Z_1$, we can discard the quadratic terms:

$$f_0 = \frac{f_1}{1 + 4f_1 C_c Z_1 + 4f_1 L/Z_1} \quad (2.47)$$

2.2.4 Variation in Load Inductance

The resonance frequency ω_0 therefore shifts with small changes in L :

$$\frac{\partial \omega_0}{\partial L} = \frac{-\omega_1}{(1 + 2\omega_1 C_c Z_1/\pi + 2\omega_1 L/\pi Z_1)^2} (2\omega_1/\pi Z_1) \quad (2.48)$$

$$= -\frac{2\omega_0^2}{\pi Z_1} \quad (2.49)$$

or

$$\frac{\partial f_0}{\partial L} = -\frac{4f_0^2}{Z_1} \quad (2.50)$$

Combining this with the small changes of load inductance with flux in the SQUID (Equation 2.21):

$$f_0(\phi) \approx f_1 - 4f_1^2 C_c Z_1 - \frac{4f_1^2 L_c}{Z_1} + \frac{4f_1^2 \lambda M_c^2}{Z_1 L_S} \cos \phi \quad (2.51)$$

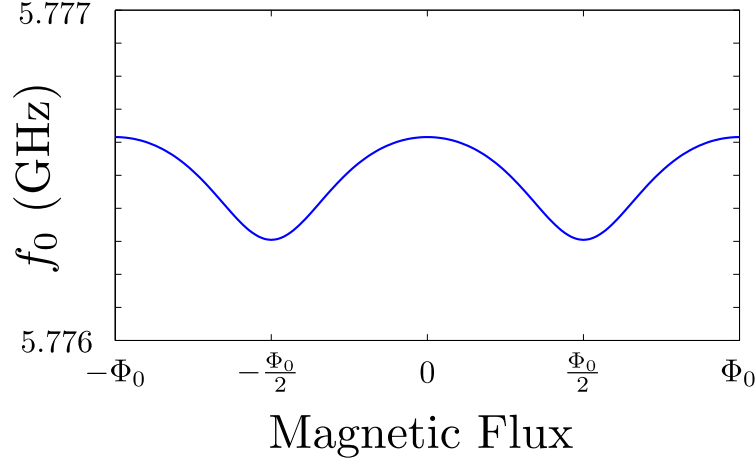


Figure 2.12: Flux variable resonance frequency for $L_c = 77.6$ pH, $M_c = 1.65$ pH, $L_S = 18.9$ pH, $\lambda = 1/3$, and an unperturbed resonance frequency of 6 GHz. These values come from the design in Section 7.1.5.2.

2.3 Resonator Bandwidth

On resonance, the resonator looks like a perfect short and reflects all microwave power. Far from resonance, the resonator looks like an open and therefore all microwave power passes by unperturbed. We now consider how quickly the resonator transitions from reflection to transmission and the response slightly detuned from resonance.

2.3.1 Resonance Shape

The reflection coefficient for a microwave signal encountering an impedance mismatch is:

$$\Gamma = \frac{Z_L - Z_0}{Z_L + Z_0} \quad (2.52)$$

In our setup the resonator is an impedance in parallel with a Z_0 termination. This means that:

$$\Gamma^{-1} = \frac{Z_L + Z_0}{Z_L - Z_0} \quad (2.53)$$

$$= \frac{1 + Z_0/Z_L}{1 - Z_0/Z_L} \quad (2.54)$$

$$= \frac{1 + Z_0 \left(\frac{1}{Z_0} + \frac{1}{Z_R} \right)}{1 - Z_0 \left(\frac{1}{Z_0} + \frac{1}{Z_R} \right)} \quad (2.55)$$

$$= \frac{2 + Z_0/Z_R}{-Z_0/Z_R} \quad (2.56)$$

$$= -(1 + 2Z_R/Z_0) \quad (2.57)$$

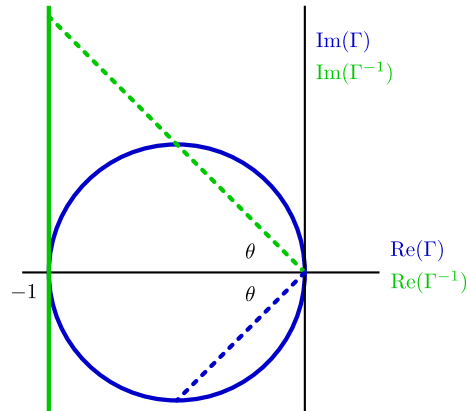


Figure 2.13: Plot of Γ^{-1} describing a vertical line in the complex plane and Γ describing a circle.

If the resonator has negligible losses then Z_R is purely imaginary and Γ^{-1} is a vertical line in the complex plane that passes through $(-1, 0)$ as in Figure 2.13. If a set of complex numbers forms a straight line in the complex plane then the reciprocal set forms a circle. Specifically, if $\Gamma^{-1} = -1 - i \tan \theta$ then $|\Gamma^{-1}| = 1/\cos \theta$ and

$$\Gamma = -\cos \theta (\cos \theta - i \sin \theta) \quad (2.58)$$

$$= -\cos^2 \theta + i \sin \theta \cos \theta \quad (2.59)$$

$$= -\frac{1}{2} \cos 2\theta - \frac{1}{2} + \frac{i}{2} \sin 2\theta \quad (2.60)$$

which describes a circle of radius $1/2$ around $(-1/2, 0)$, also shown in Figure 2.13. If the resonator has frequency-independent losses then Γ^{-1} shifts left and Γ forms a smaller circle. We usually measure transmission $S_{21} = 1 + \Gamma$ rather than reflection, and this also describes a circle in the complex plane.

The most familiar way to describe the shape of a resonance is by the peak in reflected power or dip in transmitted power.

$$|\Gamma|^2 = \frac{-1}{1 + 2Z_R/Z_0} \frac{-1}{1 + 2Z_R^*/Z_0} \quad (2.61)$$

$$= \frac{1}{1 + 4\operatorname{Re}(Z_R)/Z_0 + 4|Z_R|^2/Z_0^2} \quad (2.62)$$

Assuming negligible losses in the resonator ($\operatorname{Re}(Z_R) = 0$) and considering frequencies only slightly detuned from resonance:

$$|\Gamma|^2 \approx \frac{1}{1 + \left(\frac{2\partial Z_R/\partial\omega}{iZ_0}\right)^2 (\omega - \omega_0)^2} \quad (2.63)$$

Similarly,

$$|S_{21}|^2 = 1 - |\Gamma|^2 \quad (2.64)$$

$$\approx \frac{1}{1 + \left(\frac{iZ_0}{2\partial Z_R/\partial\omega}\right)^2 / (\omega - \omega_0)^2} \quad (2.65)$$

which are recognizable as Lorentzian lineshapes (Figure 2.14) with a full-width half-maximum bandwidth of

$$BW \approx \frac{iZ_0}{\partial Z_R/\partial\omega} \quad (2.66)$$

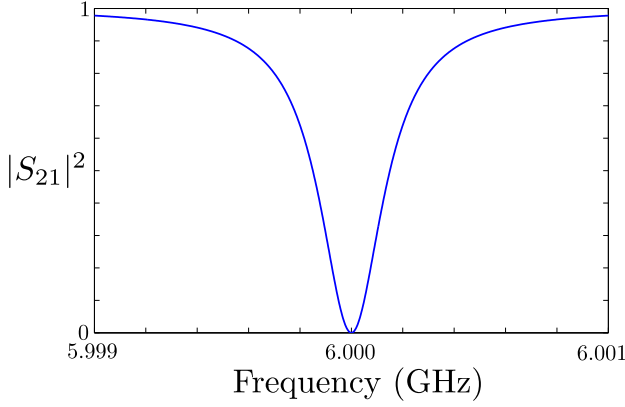


Figure 2.14: Transmitted power at different frequencies near resonance for $f_0 = 6$ GHz and $Q = 20,000$.

We often describe resonance widths by a dimensionless number $Q \equiv \omega_0/BW$ called the quality factor:

$$\boxed{Q \approx \frac{\partial(Z_R/iZ_0)}{\partial(\omega/\omega_0)}} \quad (2.67)$$

2.3.2 Coupled Q

We previously derived an expression for the impedance of a lossless resonator:

$$Z_R(\omega) = \frac{1}{i\omega C_c} + Z_1 \frac{i\omega L \cot\left(\omega \frac{l}{v_p}\right) + iZ_1}{Z_1 \cot\left(\omega \frac{l}{v_p}\right) - \omega L} \quad (2.68)$$

We can show (Appendix C) that the derivative of this impedance on resonance is:

$$\left. \frac{\partial Z_R(\omega)/iZ_0}{\partial(\omega/\omega_0)} \right|_{x=1} \approx \frac{Z_1}{Z_0} \frac{\pi}{2(\omega_0 C_c Z_1)^2} \quad (2.69)$$

This calculation allows us to extract a Q that we call the *coupled quality factor* and that reflects the finite bandwidth of the resonance resulting from the capacitive coupling to the feedline:

$$\boxed{Q_c = \frac{\pi}{2\omega_0^2 C_c^2 Z_0 Z_1}} \quad (2.70)$$

Our multiplexer designs will consistently ensure that Q_c is the lowest quality factor in the system and thus sets the bandwidth for the resonances.

2.3.3 Response to Frequency Shift

On resonance, the response of Γ to a small detuning is the same as the response of Γ^{-1} , but negative (see Figure 2.13). We are most concerned with the voltage signal in the imaginary direction:

$$\frac{d\Gamma}{d\omega} = \frac{2}{Z_0} \frac{dZ_R}{d\omega} \quad (2.71)$$

$$= 2iQ_c/\omega_0 \quad (2.72)$$

We measure the SQUID by interrogating the resonance with a fixed tone as its resonance frequency shifts. For small frequency shifts, the result of shifting the resonator away from the tone is just the inverse of the result of shifting the tone.

$$\frac{dS_{21}}{d\omega_0} = \frac{d\Gamma}{d\omega_0} = -\frac{2iQ_c}{\omega_0}$$

(2.73)

2.3.4 Energy in the Resonator

Let us now explicitly consider the energy in the resonator. This will allow us to confirm the calculations we have already performed from an impedance perspective and yield some new insights. In any electrical resonator, energy sloshes back and forth between the electric field and the magnetic field, with minimum dissipation occurring at the resonance frequency. In our quarter-wave resonator the majority of the energy is stored in the electric and magnetic fields between the inner and outer conductors of the transmission line. The line has a capacitance per unit length \mathcal{C} and inductance per unit length \mathcal{L} , which are related to the characteristic impedance and phase velocity:

$$Z_1 = \sqrt{\frac{\mathcal{L}}{\mathcal{C}}} \quad \mathcal{C} = \frac{1}{Z_1 v_p}$$

\Leftrightarrow

$$v_p = \frac{1}{\sqrt{\mathcal{L}\mathcal{C}}} \quad \mathcal{L} = \frac{Z_1}{v_p}$$

The energy stored in the electric field can be integrated over the length of the transmission line:

$$E = \int_0^l \frac{1}{2} \mathcal{C} (V(z))^2 dz \quad (2.74)$$

$$= \frac{I^2 Z_1^2}{2Z_1 v_p} \int_0^l \sin^2(\beta z) dz \quad (2.75)$$

$$= \frac{I^2 Z_1}{2v_p} \left[\frac{z}{2} - \frac{\sin(2\beta z)}{4\beta} \right]_0^l \quad (2.76)$$

$$= \frac{I^2 Z_1 l}{4v_p} \left(1 - \frac{\sin(2\beta l)}{2\beta l} \right) \quad (2.77)$$

$$= I^2 Z_1 \left(\frac{\pi}{8\omega_1} - \frac{\sin(2\beta l)}{8\beta v_p} \right) \quad (2.78)$$

Similarly, the energy stored in the magnetic field is:

$$E = \int_0^l \frac{1}{2} \mathcal{L} (I(z))^2 dz \quad (2.79)$$

$$= I^2 Z_1 \left(\frac{\pi}{8\omega_1} + \frac{\sin(2\beta l)}{8\beta v_p} \right) \quad (2.80)$$

Resonance occurs when the energy in the capacitor and inductor accounts for the difference between the energy in the electric and magnetic fields in the transmission line. The energy in the capacitor tends to dominate, so, neglecting the energy in the inductor:

$$\frac{1}{2} C_c V^2 = \frac{I^2 Z_1 \sin(2\beta l)}{4\beta v_p} \quad (2.81)$$

$$C_c \frac{I^2 \cos^2(\beta l)}{\omega_0^2 C_c^2} = \frac{I^2 Z_1 \sin(\beta l) \cos(\beta l)}{\beta v_p} \quad (2.82)$$

$$C_c^{-1} = \frac{Z_1 \omega_0^2 \tan(\beta l)}{\beta v_p} \quad (2.83)$$

$$\omega_0 C_c Z_1 = \cot(\omega_0 \frac{l}{v_p}) \quad (2.84)$$

This is a good check of our result from matching impedances. The consideration of energy stored in the inductive termination follows a similar argument. Finally, note that although the sinusoidally varying term in the energy is critical to determining the shift in resonance frequency it is a small fraction of the total energy stored in the resonator.

$$E \approx \frac{I^2 Z_1}{16 f_0}$$

(2.85)

2.3.5 Driven Steady-State

On resonance, the resonator looks like a short between the conductors of the feedline. This means that in steady-state the resonator enforces a voltage node on the feedline. If a voltage wave arrives from the left it must be reflected back to the left, inverted.

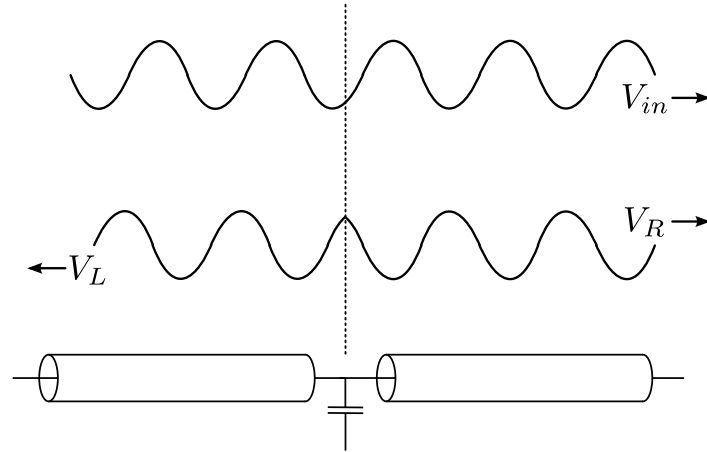


Figure 2.15: Illustration of the voltage waves for a resonator driven on resonance.

We can view this as a superposition of voltage waves as in Figure 2.15. By symmetry the two voltage waves, of amplitude V_L and V_R , generated at the resonator must propagate identically to the left and right. The third voltage wave, of amplitude V_{in} propagates from the source to the right. The sum of these waves must have a voltage node at the resonator:

$$V_L = V_R = -V_{in} \quad (2.86)$$

Although the resonator enforces a voltage node, current still flows in and out of the resonator from the feedline.

$$-i\omega_0 \mathcal{L}I = \frac{dV}{dz} \quad (2.87)$$

In this model of a superposition of voltage waves, the voltage wave from the source is continuously differentiable, and therefore supplies no current to the resonator. All current into and out of the resonator comes from the discontinuity in the derivative of the resonator voltage wave. If we parameterize the standing wave

in the resonator by the current I at the inductive termination, then at the capacitive coupler we have:

$$I \cos(\beta l) = \frac{iv_p}{\omega_0 Z_0} ((i\beta V_R) - (-i\beta V_L)) \quad (2.88)$$

$$= \frac{2v_p \beta V_{in}}{\omega_0 Z_0} \quad (2.89)$$

$$= \frac{2V_{in}}{Z_0} \quad (2.90)$$

We can therefore describe the energy in the resonator in terms of the voltage wave on the feedline

$$E \approx \frac{Z_1 \pi}{8\omega_0} I^2 \quad (2.91)$$

$$= \frac{Z_1 \pi}{8\omega_0} \frac{4V_{in}^2}{Z_0^2} \sec^2(\beta l) \quad (2.92)$$

$$= \frac{\pi P_{in} Z_1}{\omega_0 Z_0} \sec^2(\beta l) \quad (2.93)$$

$$\approx \frac{\pi P_{in}}{\omega_0} \frac{1}{\omega_0^2 C_c^2 Z_0 Z_1} \quad (2.94)$$

$$= \frac{2Q_c P_{in}}{\omega_0} \quad (2.95)$$

2.3.6 Power Dissipation in the Terminations

The steady-state calculation does not determine how quickly the resonator adjusts to a change in drive. No power enters or leaves the resonator. All input power reflects back to the source. We must calculate power loss from an excited resonator in the absence of a drive to know how quickly the resonator rings up or down.

Each time a traveling wave inside the resonator reflects from the coupling capacitor, some power leaks onto the feedline and dissipates at the terminations. The energy in the transmission line propagates down and back in $\tau = \frac{2l}{v_p}$. Thus, the internal power incident on the capacitor is

$$P_i = \frac{E}{\tau} \quad (2.96)$$

$$\approx \frac{E\omega_0}{\pi} \quad (2.97)$$

This power is constantly reflecting from a load $Z_L = \frac{1}{i\omega C_c} + \frac{Z_0}{2}$, which has a reflection coefficient of

$$\Gamma = \frac{Z_L - Z_1}{Z_L + Z_1} \quad (2.98)$$

$$= \frac{\frac{1}{i\omega_0 C_c} + \frac{Z_0}{2} - Z_1}{\frac{1}{i\omega_0 C_c} + \frac{Z_0}{2} + Z_1} \quad (2.99)$$

$$= \frac{1 + i\omega_0 C_c \left(\frac{Z_0}{2} - Z_1 \right)}{1 + i\omega_0 C_c \left(\frac{Z_0}{2} + Z_1 \right)} \quad (2.100)$$

For small capacitance, almost all the power reflects, but some disappears into the terminations:

$$1 - |\Gamma|^2 = 1 - \frac{1 + i\omega_0 C_c \left(\frac{Z_0}{2} - Z_1 \right)}{1 + i\omega_0 C_c \left(\frac{Z_0}{2} + Z_1 \right)} \frac{1 - i\omega_0 C_c \left(\frac{Z_0}{2} - Z_1 \right)}{1 - i\omega_0 C_c \left(\frac{Z_0}{2} + Z_1 \right)} \quad (2.101)$$

$$= 1 - \frac{1 + \omega_0^2 C_c^2 \left(\frac{Z_0}{2} - Z_1 \right)^2}{1 + \omega_0^2 C_c^2 \left(\frac{Z_0}{2} + Z_1 \right)^2} \quad (2.102)$$

$$= \frac{2\omega_0^2 C_c^2 Z_0 Z_1}{1 + \omega_0^2 C_c^2 \left(\frac{Z_0}{2} + Z_1 \right)^2} \quad (2.103)$$

$$\approx 2\omega_0^2 C_c^2 Z_0 Z_1 \quad (2.104)$$

which makes the dissipated power

$$P_{diss} = \frac{2E\omega_0}{\pi} \omega_0^2 C_c^2 Z_0 Z_1 \quad (2.105)$$

This power loss is twice the drive necessary to maintain the resonator at an internal energy E , which makes sense if we consider that each voltage wave emanating from the resonator would carry P_{in} if there were not other voltage waves on the line. This power loss is also in full agreement with our impedance-based calculation of coupled Q :

$$Q_c = \frac{\omega_0 E}{P_{diss}} \quad (2.106)$$

$$= \frac{\pi}{2\omega_0^2 C_c^2 Z_0 Z_1} \quad (2.107)$$

2.3.7 Antinode Current

The coupling quality factor Q_c and measurement power on the feedline determine the energy in the resonator and therefore the current oscillation at the inductive termination:

$$E = \frac{Z_1\pi}{8\omega_0} I^2 = \frac{2P_{in}Q_c}{\omega_0} \quad (2.108)$$

$$I^2 = \frac{16P_{in}Q_c}{\pi Z_1} \quad (2.109)$$

$$I = 4\sqrt{Q_c P_{in}/\pi Z_1} \quad (2.110)$$

In terms of voltage oscillation on the feedline this means

$I = V_{in} \sqrt{\frac{8Q_c}{\pi Z_0 Z_1}}$

(2.111)

This current oscillation modulates the flux in the SQUID and therefore determines the maximum microwave power we can apply for SQUID readout. Let p be the peak-to-peak measure of flux oscillating in the SQUID in units of magnetic flux quanta:

$$p \equiv \frac{2IM_c}{\Phi_0} \quad (2.112)$$

$$= V_{in} \frac{4M_c}{\Phi_0 Z_0} \sqrt{\frac{2Q_c Z_0}{\pi Z_1}} \quad (2.113)$$

Conversely, we can describe the voltage wave on the feedline in terms of flux in the SQUID:

$V_{in} = \frac{p\Phi_0 Z_0}{4M_c} \sqrt{\frac{\pi Z_1}{2Q_c Z_0}}$

(2.114)

We can also write the internal power in terms of flux in the SQUID:

$$P_i = 2f_0 E = \frac{p^2 \Phi_0^2 Z_1}{32 M_c^2} \quad (2.115)$$

2.3.8 Matching Frequency Shift to Bandwidth

In general, we choose the bandwidth for a resonator and then try to match the SQUID response to that bandwidth. If the peak-to-peak SQUID response is less than the bandwidth, we sacrifice possible SQUID gain. If the peak-to-peak SQUID response is greater than the bandwidth, there are two problems.

First, SQUID response becomes more square wave than sinusoidal. Second, measurement at high microwave power risks resonator bistability[76]. Let $\eta = \Delta\omega/BW$ parameterize the coupling strength:

$$\eta = \frac{2\omega_0^2}{\pi Z_1} \left(\frac{M_c^2}{L_S} \frac{2\lambda}{1 - \lambda^2} \right) \frac{Q_c}{\omega_0} \quad (2.116)$$

$$= \frac{4\omega_0 Q_c}{\pi Z_1} \frac{M_c^2}{L_S} \frac{\lambda}{1 - \lambda^2} \quad (2.117)$$

This allows us to relate mutual inductance to resonator bandwidth:

$$\boxed{\frac{\omega_0 M_c^2}{Z_1 L_S} = \frac{\eta \pi}{4\omega_0 Q_c} \frac{1 - \lambda^2}{\lambda}} \quad (2.118)$$

When the bandwidth matches the frequency shift the transmission looks like Figure 2.16. This response allows a single fixed tone to perform sensitive SQUID readout at nearly all values of flux.

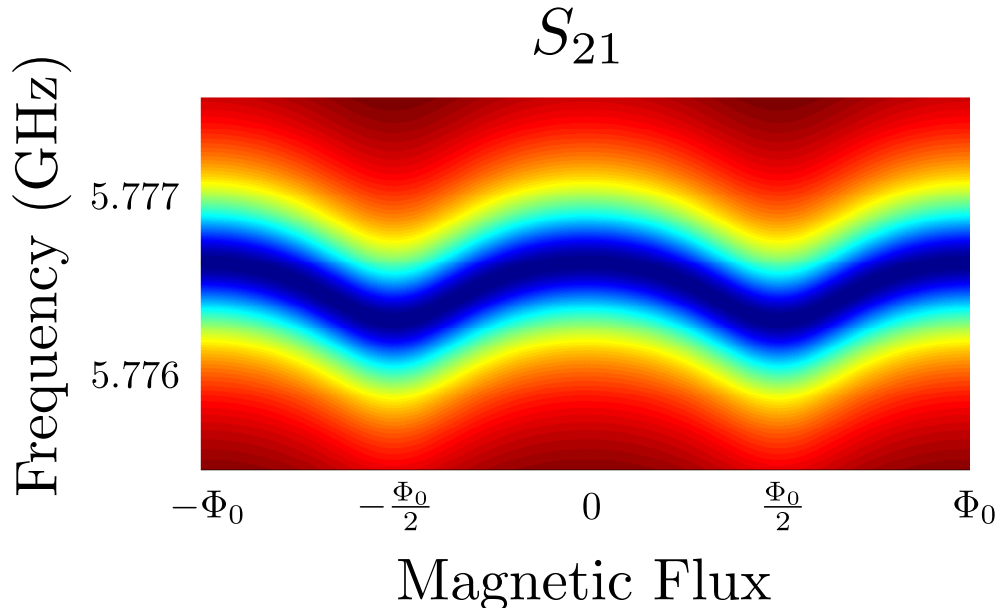


Figure 2.16: Transmitted power as a function of frequency and magnetic flux through the SQUID for a matched resonator. Red is high transmission and blue is low transmission.

Tracking the resonance in frequency space with a phase-locked loop could allow overcoupled operation. This technique may be useful in the future, for example to read out magnetic calorimeters[9][10], which may require lower flux noise than critical coupling can provide.

2.3.9 Crosstalk and Resonance Spacing

Adjacent resonators can couple through the tails of their Lorentzian responses. Consider a voltage wave travelling along the feedline and passing two resonators of variable resonance frequency. The transmission coefficient for the system, allowing for multiple reflections between the resonators, is:

$$S_{21} = (1 + \Gamma_1)(1 + \Gamma_2)(1 + \Gamma_1\Gamma_2 + \Gamma_1^2\Gamma_2^2 + \dots) \quad (2.119)$$

$$= \frac{(1 + \Gamma_1)(1 + \Gamma_2)}{1 - \Gamma_1\Gamma_2} \quad (2.120)$$

$$= \frac{(\Gamma_1^{-1} + 1)(\Gamma_2^{-1} + 1)}{\Gamma_1^{-1}\Gamma_2^{-1} - 1} \quad (2.121)$$

$$= \frac{4 \frac{Z_{R1}Z_{R2}}{Z_0^2}}{4 \frac{Z_{R1}Z_{R2}}{Z_0^2} + 2 \frac{Z_{R1}}{Z_0} + 2 \frac{Z_{R2}}{Z_0}} \quad (2.122)$$

$$= \frac{2}{2 + \frac{Z_0}{Z_{R1}} + \frac{Z_0}{Z_{R2}}} \quad (2.123)$$

Assuming lossless resonators at high coupling Q so that $Z_R \propto i\delta\omega$ we can rewrite S_{21} in terms of BW :

$$S_{21} = \frac{2}{2 - i \left(\frac{BW}{\omega - \omega_1} + \frac{BW}{\omega - \omega_2} \right)} \quad (2.124)$$

Consider shifting one resonance, ω_2 while measuring at ω on resonance with the unperturbed value of another resonator spaced n bandwidths away at ω_1 :

$$\Delta S_{21} = \frac{-2}{\left(2 - i \left(-\frac{BW}{\Delta\omega_1} - \frac{BW}{nBW} \right) \right)^2} \left(-iBW \frac{-1}{(nBW)^2} \right) (-\Delta\omega_2) + O(\Delta\omega_2^2) \quad (2.125)$$

$$\approx \frac{i}{2n^2 \left(1 + i \left(\frac{BW}{2\Delta\omega_1} + \frac{1}{2n} \right) \right)^2} \frac{\Delta\omega_2}{BW} \quad (2.126)$$

The crosstalk vanishes for $\Delta\omega_1 = 0$ as we expect because the voltage wave is fully reflected and never reaches the second resonator. One can show that the crosstalk into the imaginary component of S_{21} is maximized for $\frac{BW}{2\Delta\omega_1} + \frac{1}{2n} = \sqrt{3}$ so that the maximum crosstalk is

$$\text{Im}[\Delta S_{21}] \approx \frac{1}{2n^2} \frac{1-3}{(1+3)^2} \frac{\Delta\omega_2}{BW} \quad (2.127)$$

$$\approx \frac{-1}{16n^2} \frac{\Delta\omega_2}{BW} \quad (2.128)$$

To keep crosstalk between neighboring resonators at less than a part per 1,000 we therefore space resonators by at least ten times their bandwidth.

2.4 Losses in the Resonator Circuit

We have already considered loss in the Josephson junctions in Section 2.1.4. We will consider three additional loss mechanisms: loss to free-space radiation, loss in the transmission line, and loss in the input circuit. If we design the multiplexer correctly, the combination of these losses should be significantly less than the power dissipated in the terminations of the input and output ports.

2.4.1 CPW Radiation

The losses due to radiation from a quarter-wave resonator with dielectric below and free-space above can be given as[77]:

$$Q_{rad} = \frac{\pi(1+\epsilon)^2}{2\epsilon^{5/2}} \frac{\eta_0}{Z_0} \frac{1}{I'(\epsilon, n)} \frac{1}{n-1/2} \left(\frac{L}{s}\right)^2 \quad (2.129)$$

where $\eta_0 = 377 \Omega$ is the impedance of free space, n is the mode number, ϵ is the dielectric constant of the substrate, and s is the spacing between the centerlines of the two slots. $I'(\epsilon, n)$ is an integral that can be calculated numerically, e.g. for $\epsilon = 10$ and $n = 1$:

$$I'(10, 1) = 1.62 \quad (2.130)$$

and thus we find that for our fundamental oscillations with $\epsilon \approx 10$

$$Q_{rad} \approx 5.6 \left(\frac{L}{s}\right)^2 \quad (2.131)$$

for a typical design we might have $L = 5300 \mu\text{m}$ and $s = 16 \mu\text{m}$ so

$$Q_{rad} \approx 600,000 \quad (2.132)$$

This analytic calculation is a poor substitute for computational modeling, because it does not consider such things as the conducting enclosure which is closer than a free-space wavelength to the CPW. We have measured much higher internal quality factors in real devices.

2.4.2 Dielectric Loss

There is also lossy dielectric in the resonator transmission line, the silicon substrate and oxide coating the metal layers. The attenuation constant in a coaxial transmission line with a lossy dielectric between the

ground and the center conductor is

$$\alpha = \frac{\omega_0 \tan \delta}{2v_p}. \quad (2.133)$$

In a coaxial geometry the electric field is distributed evenly throughout the dielectric, but in a coplanar waveguide geometry the electric field is non-uniform and mostly exists outside of the dielectric. We can describe this with a loss tangent δ for the dielectric and a filling factor F that accounts for the distribution of the electric field in the dielectric:

$$\alpha \approx \frac{\omega_0 F \delta}{2v_p} \quad (2.134)$$

This attenuation constant means that a voltage wave starting at the capacitor, travelling to the inductive load, reflecting, and returning to the capacitor in time $\tau = \frac{2l}{v_p}$ gets attenuated by $e^{-2\alpha l}$. For weak attenuation this means that

$$Q_d = \frac{E\omega_0}{P} \quad (2.135)$$

$$= \frac{E\omega_0}{\frac{E}{\tau} \left(1 - (e^{-2\alpha l})^2 \right)} \quad (2.136)$$

$$\approx \frac{\omega_0 \tau}{4\alpha l} \quad (2.137)$$

$$= \frac{\omega_0}{2\alpha v_p} \quad (2.138)$$

$$= \frac{1}{F\delta} \quad (2.139)$$

$F\delta \sim 10^{-5}$ has been reported[78] at low power for niobium CPW ($s = 10 \mu\text{m}$) resonators on sapphire. We operate at higher power, which can saturate the two-level systems, and have measured $Q_i > 2 \times 10^6$ for bare resonators of niobium on high resistivity silicon.

2.4.3 Loss in the Flux Input Circuit

The circuit that feeds a magnetic flux signal to the SQUID (Figure 2.17) may present an impedance with a real component. Microwave power in the resonator may therefore dissipate in the input circuit.

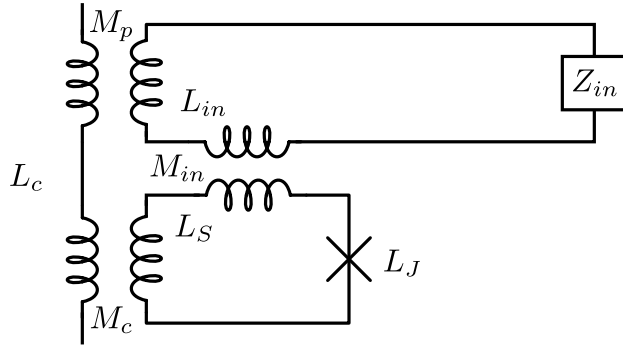


Figure 2.17: Schematic of the rf SQUID and input coil coupling to both the resonator and each other.

There are two ways for microwave power to couple to the input circuit. First, there is an unavoidable parasitic coupling from the resonator termination into the input coil. Second, the resonator drives microwave currents in the SQUID loop which directly couple to the input coil. Maximum coupling occurs when $\phi = \pi$ and the SQUID effectively "anti-screens" flux from the resonator. Solving the coupled set of linear equations gives (Appendix B.2):

$$\text{Re}[Z_L] \approx R_F \frac{M_c^2 M_{in}^2 + 4L_S (L_S M_p^2 + M_{in} M_c M_p)}{(2L_S(L_{in} + L_F) + M_{in}^2)^2} \quad (2.140)$$

where we have modeled the input impedance as an L/R -filter because in practice we place inductive chokes L_F shunted by resistors R_F on the input coils to prevent microwave power from reaching the input devices. A resistive termination on the quarter-wave resonator results in a power loss of

$$P = \frac{I^2 \text{Re}[Z_L]}{2} \quad (2.141)$$

$$= \frac{4\omega_0 E \text{Re}[Z_L]}{\pi Z_1}. \quad (2.142)$$

from which we can calculate a quality factor

$$Q_f = \frac{\omega_0 E}{P} \quad (2.143)$$

$$= \frac{\pi Z_1}{4 \text{Re}[Z_L]} \quad (2.144)$$

Plugging in the transformed filter resistance:

$$Q_f = \frac{\pi Z_1}{4R_F} \frac{(2L_S(L_{in} + L_F) + M_{in}^2)^2}{M_c^2 M_{in}^2 + 4L_S (L_S M_p^2 + M_{in} M_c M_p)} \quad (2.145)$$

which we can increase by increasing L_F and decreasing R_F . When we design input filters, we use this equation to ensure that they do not limit the resonator bandwidth.

2.4.4 S_{21}^{min}

We measure the transmitted and reflected power before it dissipates in the matched terminations of the external ports, and so Q_c differs from the other Q 's in its effect on the resonance circle. Q_c sets the bandwidth of the resonance but has no effect on S_{21}^{min} . If the resonator is lossless, $S_{21}^{min} = 0$ because on resonance the resonator becomes a perfect short and reflects all power. If power dissipates in the resonator:

$$P_{diss} = (1 - |S_{21} - 1|^2 - |S_{21}|^2) P_{in} \quad (2.146)$$

$$= 2P_{in} (\text{Re}[S_{21}] - |S_{21}|^2) \quad (2.147)$$

On resonance, the impedance of a lossy resonator becomes purely real, so

$$P_{diss} = 2P_{in} (S_{21}^{min} - (S_{21}^{min})^2) \quad (2.148)$$

$$= 2P_{in} S_{21}^{min} (1 - S_{21}^{min}) \quad (2.149)$$

$$= \frac{\omega_0 E}{Q} S_{21}^{min} (1 - S_{21}^{min}) \quad (2.150)$$

$$\approx \frac{\omega_0 E}{Q} S_{21}^{min} \quad (2.151)$$

and therefore

$$S_{21}^{min} \approx \frac{Q}{Q_i} \quad (2.152)$$

Note that

$$P_{diss} \approx 2P_{in} \frac{Q}{Q_i} \quad (2.153)$$

will be useful for calculating cold-stage heating, but that for a particular SQUID design, biased for maximum signal-to-noise, $P_{in}Q$ is constant.

$$2P_{in}Q = \frac{Z_1 \pi p^2 \Phi_0^2}{32M_c^2} \quad (2.154)$$

Therefore improvements in Q_i are the only way to reduce the per-pixel heat load.

2.5 Flux Noise

We will consider four sources of noise: Johnson noise in the flux input circuit, intrinsic flux noise in the SQUID, HEMT noise, and two-level system (TLS) noise in the resonator. The HEMT noise turns out to be the dominant broadband noise source in these systems, while the TLS noise dominates at low frequencies. We evade the excess low-frequency noise with a technique called *flux-ramp modulation*.

2.5.1 Johnson Noise

The lossy input filter can drive noise currents through the SQUID input coil of $S_I = 4k_B T / R_F$. We therefore choose R_F to ensure that this noise is small compared to the other sources of noise in the system. For example, at a base temperature of 300 mK, $R_F \approx 0.2 \Omega$, and $M_{in} \approx 88 \text{ pH}$, the input filter produces roughly $0.2 \mu\Phi_0 / \sqrt{\text{Hz}}$.

2.5.2 SQUID Noise

The dissipationless rf SQUID lacks an analog to Johnson noise to the extent that it is truly dissipationless, but there are other common mechanisms of noise in SQUIDs that can apply. One is fluctuations of the junction critical current[79][80] and another is the flipping of magnetic dipoles on the SQUID loop[81]. Both mechanisms produce noise with a spectral density that scales inversely with frequency, so-called $1/f$ noise. Magnetic dipole noise should be enhanced when $\phi = n\pi$ and suppressed when $\phi = (n + \frac{1}{2})\pi$, while critical current noise should be enhanced when $\phi = (n + \frac{1}{2})\pi$ and suppressed when $\phi = n\pi$.

Experiments have shown that in the NIST dc SQUIDs Johnson noise in the shunt resistors dominates to well below $1 \mu\Phi_0 / \sqrt{\text{Hz}}$ at 1 Hz. Since we use a similar layout and similar fabrication process to the NIST dc SQUID, we expect these noise contributions to be small. Measurements of low-frequency noise at different flux bias points confirm that these mechanisms are not significant in our system.

2.5.3 HEMT noise

The noise due to the HEMT amplifier, referred to flux in the SQUID is determined by the SQUID gain at maximum power:

$$\left. \frac{dV}{d\Phi} \right|_{\omega=\omega_0, \Phi=\Phi_0/2} = V_{in} \frac{d\text{Im}(S_{21})}{d\omega} \frac{d\omega_0}{dL} \frac{dL}{d\phi} \frac{2\pi}{\Phi_0} \quad (2.155)$$

$$= \frac{p\Phi_0 Z_0}{4M_c} \sqrt{\frac{\pi Z_1}{2Q_c Z_0}} \frac{2Q_c}{\omega_0} \frac{-2\omega_0^2 - \lambda M_c^2}{\pi Z_1} \frac{2\pi}{L_S} \frac{\Phi_0}{\Phi_0} \quad (2.156)$$

$$= \omega_0 p \lambda \frac{M_c}{L_S} \sqrt{2\pi Q_c Z_0 / Z_1} \quad (2.157)$$

$$\approx \omega_0 p \sqrt{\frac{\pi^2 \eta \lambda Z_0}{2\omega_0 L_S}} \quad (2.158)$$

we will generally desire $\eta \approx 1$ and $p \approx 1/\pi$, i.e. matched coupling with a strongly driven but not over-driven SQUID:

$$\boxed{\left. \frac{dV}{d\Phi} \right|_{\omega=\omega_0, \Phi=\Phi_0/2} \approx \omega_0 \sqrt{\frac{Z_0}{2\omega_0 L_J}}} \quad (2.159)$$

At this gain, the voltage noise of the HEMT, $S_V = 4k_B T_N Z_0$ refers to a flux noise in the SQUID of

$$\boxed{S_\Phi|_{f=f_0, \Phi=\Phi_0/2} \approx \frac{4k_B T_N L_J}{\pi f_0}} \quad (2.160)$$

For $T_N = 6$ K, $f_0 = 6$ GHz, and $L_J = 60$ pH this is a noise of $0.58 \mu\Phi_0/\sqrt{\text{Hz}}$.

2.5.4 TLS noise

Another major source of noise is fluctuations in two-level systems (TLS) in the resonator[58][82][78].

Where these have an electric dipole moment and feel the electric field of the resonator, they affect the distributed capacitance when they switch state and therefore produce fluctuations in the resonance frequency. Considering only the gain from flux to frequency:

$$\left. \frac{1}{f_0} \frac{df_0}{d\Phi} \right|_{f=f_0, \Phi=\Phi_0/2} = \frac{1}{\omega_0} \frac{d\omega_0}{dL} \frac{dL}{d\phi} \frac{2\pi}{\Phi_0} \quad (2.161)$$

$$= \frac{4\lambda\omega_0 M_c^2}{Z_1 L_S \Phi_0} \quad (2.162)$$

$$= \frac{\eta\pi}{Q_c \Phi_0} (1 - \lambda^2) \quad (2.163)$$

we again consider the matched state, $\eta \approx 1$, and small λ :

$$\left. \frac{1}{f_0} \frac{df_0}{d\Phi} \right|_{f=f_0, \Phi=\Phi_0/2} \approx \frac{\pi}{Q_c \Phi_0} \quad (2.164)$$

Referring frequency noise through this gain:

$$S_\Phi|_{f=f_0, \Phi=\Phi_0/2} \approx \left(\frac{Q_c \Phi_0}{\pi f_0} \right)^2 S_{f_0} \quad (2.165)$$

The frequency noise $S_{\delta f_0}$ of CPW resonators like the ones we use scales with geometry as $s^{-1.6}$ and internal power as $P_i^{-1/2}$ [58][78]. Gao reported the frequency noise at 1 kHz for resonators made of various materials[82]. The internal power predicted by Equation 2.115 for our most recent SQUIDs is roughly 1 μW , and at this internal power Gao measured $S_{\delta f_0}/f_0^2 \approx 10^{-19}/\text{Hz}$ which for $Q_c \approx 20,000$ predicts a flux noise of roughly $2 \mu\Phi_0/\sqrt{\text{Hz}}$ at 1 kHz.

This noise can be improved by going to lower Q_c and changing the resonator geometry.

2.6 Flux-ramp Modulation

A necessary component of any SQUID multiplexer is a method for linearizing the SQUID response. Conventional linearization uses an active feedback loop to maintain the SQUID at a particular flux bias point. The feedback current is then directly proportional to the input current. The Microwave SQUID Multiplexer cannot use this technique because it would have to apply feedback to every SQUID in the array, re-introducing the multiplexing problem.

The alternative method we propose is *flux-ramp modulation*. We apply a periodic ramp that sweeps through multiple flux quanta in the SQUIDs, and require the slew rate of this ramp to greatly exceed that of any expected input signal. An input signal therefore looks like a flux offset during the duration of the ramp and produces a phase-shift in the SQUID response:

$$\phi = 2\pi \frac{\Phi}{\Phi_0} \quad (2.166)$$

To measure flux in the SQUID, we track the phase of the SQUID response. This method linearizes the SQUID response up to a slew-rate set by the frequency and amplitude of the flux-ramp. Most importantly, it can linearize all the SQUIDs in a large array using a single low-frequency flux bias line to apply the

flux-ramp to every SQUID in the array. As a bonus, the flux-ramp modulates the input signal of the SQUID up to higher frequencies, and can therefore avoid low-frequency noise in the amplifier chain after the SQUID.

Flux-ramp modulation increases readout noise relative to open-loop readout on the steepest slope of the SQUID response or readout in a flux-locked loop. The noise increases because some measurements of the ramp response occur near extrema of the SQUID response curve, where it is insensitive to magnetic flux.

Assuming stationary noise and a sinusoidal SQUID response we can calculate the effective degradation in signal-to-noise. The signal-to-noise of independent measurements adds in quadrature. With stationary noise the signal-to-noise is proportional to the slope of the SQUID response and the degradation factor α is

$$\alpha = \frac{1}{2\pi} \int_0^{2\pi} \left(\frac{d}{d\phi} \sin \phi \right)^2 d\phi \quad (2.167)$$

$$= \frac{1}{2\pi} \int_0^{2\pi} \cos^2 \phi d\phi \quad (2.168)$$

$$= \frac{1}{2} \quad (2.169)$$

We should therefore expect at least a $\sqrt{2}$ increase in flux noise when using flux-ramp modulation. This noise increase is balanced by the ability to linearize the response of all the SQUIDs in an array and modulate their input signals using a single pair of wires.

Chapter 3

Fabrication

These devices were fabricated by Leila Vale and Gene Hilton in the Quantum Fabrication Facility at NIST in Boulder, CO.

3.1 Substrate

To minimize two-level systems in the substrate, these devices are fabricated on 3 inch diameter wafers of high-resistivity silicon[83] ($\rho > 10^4 \Omega \text{cm}^2$, 380 μm). The wafers are covered with a 20 nm layer of SiO_2 .

3.2 Junction Fabrication

SQUID fabrication requires Josephson junctions with reliable critical current density J_c and minimal leakage current. The NIST process for Josephson junctions begins with a trilayer deposition in vacuum: deposit niobium (200 nm), deposit a thin layer of aluminum ($\sim 7 \text{ nm}$), flow oxygen to oxidize it, and deposit more niobium (120 nm). The entire wafer thus begins as a Josephson junction. The trilayer process has been tuned over the last 10 years and produces repeatable critical current density and low leakage across the wafer. The current rf SQUIDs use a $J_c = 0.5 \mu\text{A}/\mu\text{m}^2$ adaptation of the standard $J_c = 5 \mu\text{A}/\mu\text{m}^2$ trilayer recipe used for the NIST time-division SQUID multiplexers.

The top two layers are etched away over most of the wafer, leaving isolated junction pillars. An additional niobium wiring layer subsequently connects these junctions to SQUID loops.

3.3 SQUID and Resonator Fabrication

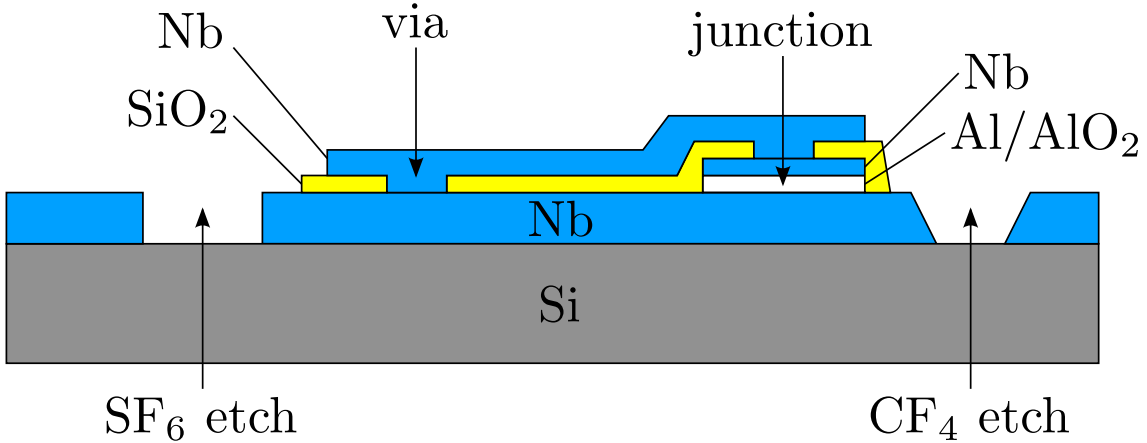


Figure 3.1: Diagram of the main layers of the microwave SQUID process.

Standard photolithography techniques pattern etch masks for the junctions, resonators, and SQUID wiring. The SQUID loop is defined in the base layer of niobium with a CF_4/O_2 reactive ion etch. This etch creates sloped sidewalls and therefore makes wiring crossovers more reliable. A silicon dioxide insulating layer is deposited (350 nm) and vias are etched in it to expose the junction islands and allow reconnection to the base niobium layer. A new layer of niobium is deposited (300 nm) that connects to these junctions and the base niobium. This layer constitutes the second wiring layer, while the base layer of the trilayer deposition constitutes the first wiring layer. These layers are shown in Figure 3.1.

The wiring pattern in the new layer is defined with an SF_6 reactive ion etch. This etch creates vertical sidewalls and appears to give much higher internal Q in niobium resonators. It is also used to define the coplanar waveguide resonators in the first layer of niobium.

Since the resonator is defined in the first layer of niobium, it will have had silicon dioxide deposited over it, then niobium, and then the second layer of niobium etched away. At the end of the process, the silicon dioxide is etched away wherever possible to minimize the two-level system noise.

There is also a deposition and etch of a $2\Omega/\square$ layer of PdAu (135 nm) for the filter resistors.

Chapter 4

Measurement Setup

Early work ($\mu\text{mux}07\text{a}$, $\mu\text{mux}09\text{a}$) took place in a dilution refrigerator in Konrad Lehnert's lab at JILA, with the HEMT in liquid helium at 4 K and the resonators at 17 mK. Later work ($\mu\text{mux}09\text{a}$, $\mu\text{mux}10\text{b}$) took place in an adiabatic demagnetization refrigerator (ADR) at NIST (Figure 4.1), with the HEMT at 3 K and the resonators at temperatures ranging from 70 mK to 350 mK depending on the measurement.

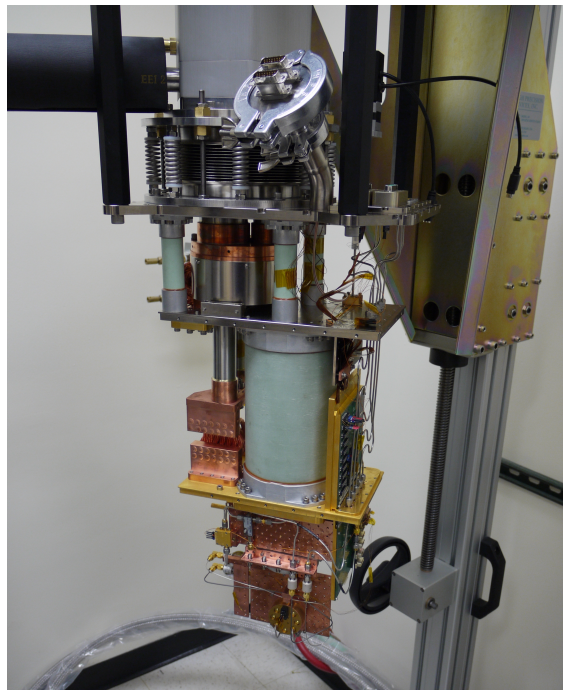


Figure 4.1: Photo of the the Adiabatic Demagnetization Refrigerator (ADR) at NIST, configured for microwave measurements.

Most experiments begin with sweeps on a network analyzer to identify the resonance frequency, Q 's, and flux-dependence of the resonances. We then interrogate specific resonances using a homodyne setup (Figure 4.2) to measure of the amplitude and phase of the microwave signal transmitted through the multiplexer.

This setup generates a microwave signal and splits it into two arms: a reference arm and a measurement arm. The measurement arm enters the cryostat, passes through the multiplexer, and returns to room temperature through the HEMT amplifier. The two arms mix at room temperature in an I-Q mixer, which extracts the amplitude of the in-phase and quadrature-phase components of the measurement signal with respect to the reference signal. The phase shifter on the reference arm rotates the signal in the I-Q plane to allow us to place first-order phase shifts ($\text{Im}[S_{21}]$) in one quadrature.

The expected input power of the local-oscillator (LO) port of the mixer determines the microwave power at the outputs of the splitter and a variable attenuator at room temperature to determine the microwave power entering the cryostat. The measurement signal passes through another attenuator at 3 K and a directional coupler at base temperature. It then enters the multiplexer chip and passes by the resonance structures which modulate the transmitted amplitude and phase. It then passes through a circulator to the HEMT amplifier. A room-temperature amplifier boosts the signal to the expected input power of the RF port of the mixer. The two arms mix and produce two low-frequency signals that we digitize and analyze.

We want the multiplexer chip to see cold 50Ω terminations on both ports to minimize the noise temperature of the feedline. The measurement signal begins with a noise temperature of 300 K. We reduce this noise temperature with a -20 dB attenuator at 3 K and a -20 dB directional coupler at base temperature. The directional coupler dissipates the incident power a different termination than it presents to the multiplexer, to guarantee that the multiplexer sees a termination at base temperature. A circulator provides the cold termination on the output side of the multiplexer and isolates it from the HEMT, which has an input noise temperature of roughly 5 K. Figure 4.3 shows the actual microwave components at 3 K and base temperature.

Appendix A lists the instruments and components used in this work.

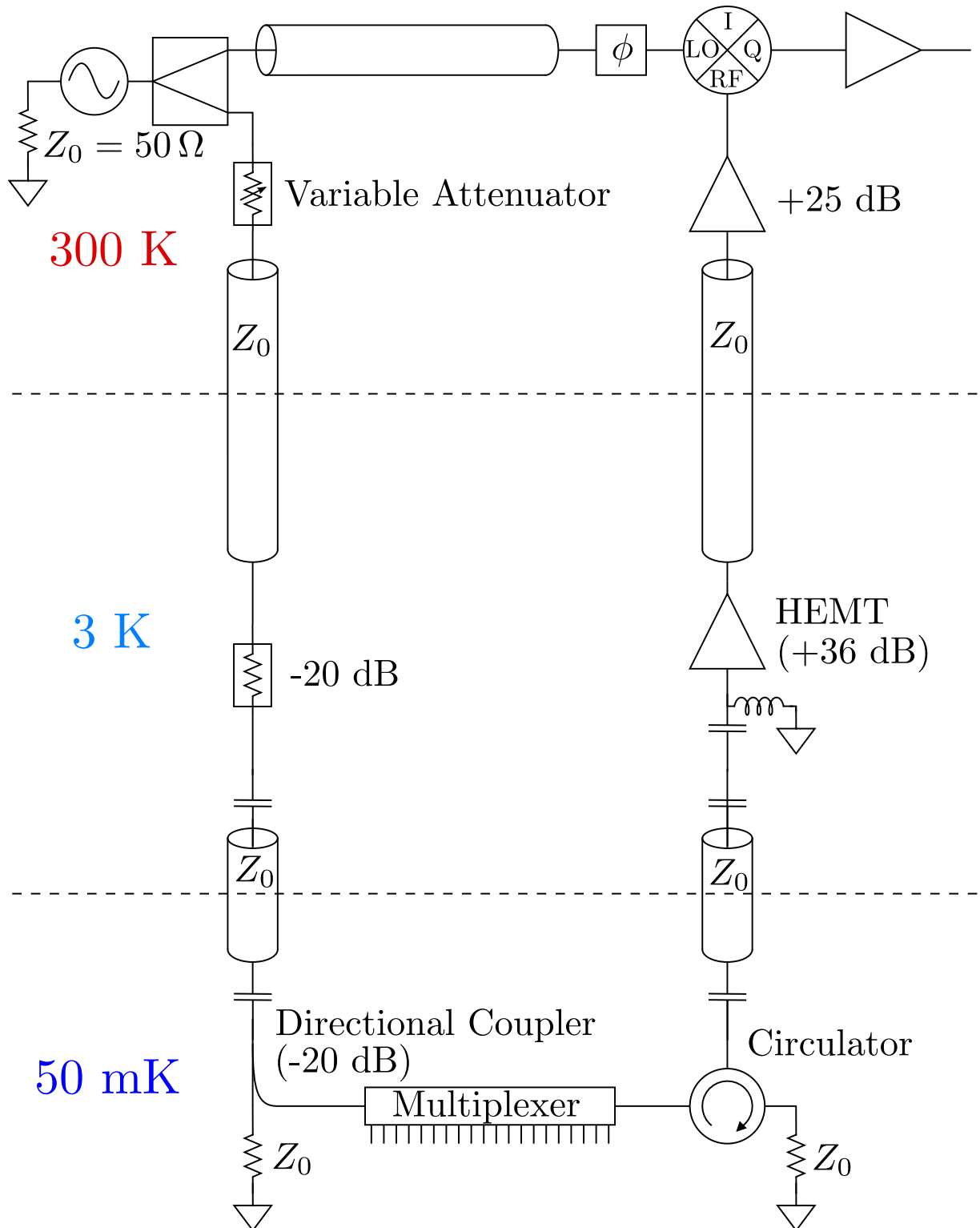


Figure 4.2: Schematic of the measurement apparatus for a single pixel.

To minimize the heat load on the ADR we use copper-nickel coaxial cables between 300 K and 3 K, thin copper-nickel coaxial cables between 3 K and the base temperature on the multiplexer input, and thin niobium-titanium coaxial cables between 3 K and the base temperature on the multiplexer output. We reduce the WiedemannFranz thermal conductivity by breaking the dc electrical connection of the coaxial cables with inside/outside dc blocks. Without good heat sinking the center pin of the HEMT can get much hotter than 3 K, so we heat sink it with a bias tee.

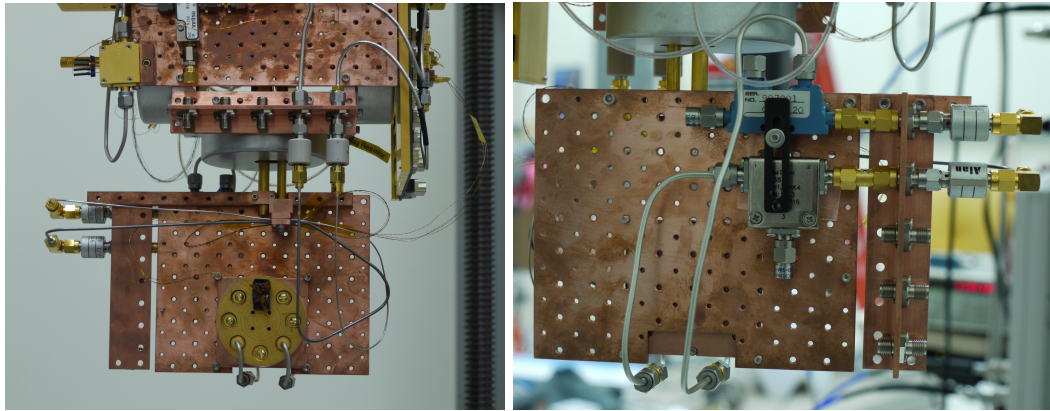


Figure 4.3: Photos of the microwave components in an adiabatic demagnetization refrigerator (ADR).

To simultaneously measure the flux in two SQUIDs, we used two synthesizers, two I-Q mixers, and splitters to combine the tones on the input and send a copy of the transmitted signals to each mixer.

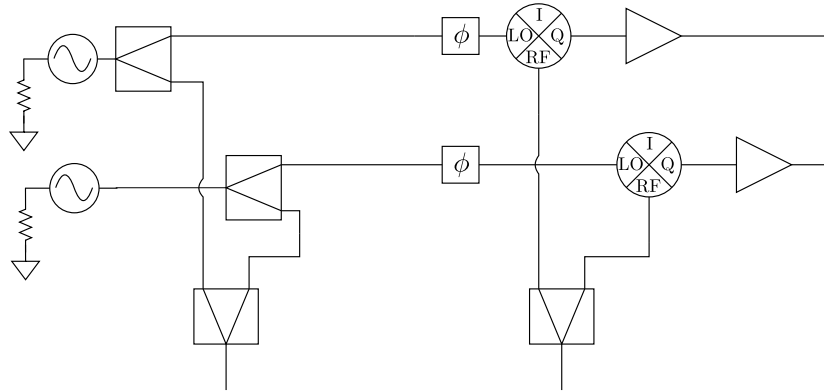


Figure 4.4: Schematic of the setup for measurement with two tones.

4.1 Open-Source Electronics

A collaboration including our research group, several MKID groups, and several groups of digital electronics engineers, has been developing open-source electronics to read out microwave frequency division multiplexers[84][85]. These electronics perform Software-Defined Radio (SDR), digitally generating a superposition of measurement tones and digitally recording their transmitted amplitude and phase.



Figure 4.5: Photo of the open-source electronics.

The existing open-source electronics (Figure 9.2) uses two 1 GS/s, 16-bit DACs to generate the measurement tones. We can mix these tones with a 4-8 GHz carrier to upconvert them to the microwave frequencies of interest, pass them through the multiplexer circuit, and mix them back down to baseband. Two 550 MS/s, 12-bit ADCs then extract the amplitude and phase.

Chapter 5

Design Summary

Subject to the constraints of the fabrication process and the physical theory, we designed, fabricated, and tested multiple generations of Microwave SQUID Multiplexer:

- $\mu\text{mux}07\text{a}$ was a proof-of-principle. It coupled simple, low-inductance dissipationless rf SQUIDs to microwave resonators and the resonators to a common feedline. It explored overcoupled and undercoupled regimes as well as rudimentary gradiometry and input filters. The primary goal was to perform microwave readout of a dissipationless rf SQUID. The secondary goal was to achieve low flux noise.
- $\mu\text{mux}09\text{a}$ built on the success of $\mu\text{mux}07\text{a}$. The SQUID became a second-order gradiometer using slit and slotted washers. Input coupling increased to achieve low current noise for coupling to TES devices.
- $\mu\text{mux}10\text{b}$ integrated the lessons of the previous designs to form a practical multiplexer for an array of CMB TESs. This entailed tight packing of the resonances in frequency space, optimizations to improve yield, and a common flux bias coil for flux-ramp modulation. The primary goal was a two-pixel TES multiplexing demonstration.

The next three sections describe the design process and experimental results (resonance spacing, Q , flux-dependence, flux-ramp modulation, crosstalk, noise) for these devices. They describe the major results of $\mu\text{mux}07\text{a}$ and $\mu\text{mux}09\text{a}$ and give a comprehensive treatment of $\mu\text{mux}10\text{b}$, culminating in a multiplexing demonstration with transition-edge sensors designed for polarimetry of the CMB.

Chapter 6

μ mux07a: Low Flux Noise

6.1 Design

μ mux07a was our first design to use dissipationless rf SQUIDs. It couples 33 of these SQUIDs to superconducting resonators with resonance frequencies around 5 GHz and bandwidths on the order of 1 MHz ($Q \approx 5,000$). We designed the SQUID-resonator coupling so that some SQUIDs are overcoupled and some are undercoupled, included both gradiometric and non-gradiometric SQUID designs, and used microwave blocking filters on the input coils.

6.1.1 Resonator Design

The transmission lines for the feedline and resonators are coplanar waveguides (CPW) of niobium on high purity silicon. A coplanar waveguide consists of a center conductor with ground plane on both sides separated by a gap (Figure 6.1). The simplicity of this geometry is particularly appealing because it does not require dielectric between the conductors, avoiding a significant mechanism of loss and source of two-level-system noise. The high critical temperature of niobium ($T_c = 9.2$ K) means that at operating temperatures of roughly 300 mK there will be low thermal excitation of quasiparticles and therefore low microwave loss. We have measured $Q_i > 2 \times 10^6$ in niobium resonators on high-purity silicon. (Leduc[83] has measured $Q_i > 3 \times 10^7$ in titanium nitride resonators on high-purity silicon, but we do not need such low loss.)

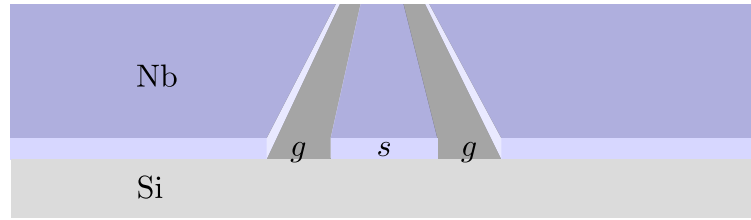


Figure 6.1: Diagram of a coplanar waveguide showing center conductor with a ground plane on both sides.

The frequency noise $S_{\delta f_0}$ of such CPW resonators exhibits a $f^{-1/2}$ spectral dependence and scales with geometry as $s^{-1.6}$ and power as $P_i^{-1/2}$ [58][78]. Gao reported the frequency noise at 1 kHz for resonators made of various materials[82], including niobium with a 3 μm center strip and 2 μm gaps at various internal powers. The internal power predicted by Equation 2.115 for these SQUIDs was roughly 0.1 μW or -40 dBm, and at this internal power Gao measured $S_{\delta f_0}/f_0^2 \approx 10^{-19}/\text{Hz}$.

For our design Q , this frequency noise implies (Equation 2.165) a flux noise of $0.5 \mu\Phi_0/\sqrt{\text{Hz}}$, exceeding the flux noise due to the HEMT. We designed resonators with a 10 μm center strip and 6 μm gaps to reduce this noise.

We chose to fabricate 33 resonators on a chip, spacing them 30 MHz apart to ensure negligible crosscoupling (Section 2.3.9). We used TX-line[86] to calculate the characteristic impedance $Z_1 = 50.3 \Omega$ and wavelength $\lambda = 20.4 \text{ mm}$ at 6 GHz, using $\epsilon = 11.45$ for the silicon substrate at cryogenic temperatures[87]. The coupling capacitor and coupling inductor combine to lower the resonance frequency by 10%. We therefore designed waveguides between 4 mm and 5 mm long, stepping the length by 25 μm .

6.1.2 Resonator-Feedline Coupling

We designed coupling capacitors for a spread around $Q_c \approx 3,000$ by simulating S_{13} of various designs in Microwave Office, where ports 1 and 2 are the ports of the feedline and port 3 is the resonator side of the coupler. From Section 2.3.6, this transmission coefficient relates to Q_c by:

$$Q_c = \frac{\pi}{1 - |\Gamma|^2} \quad (6.1)$$

$$= \frac{\pi}{2|S_{13}|^2} \quad (6.2)$$

The simulations led to various interdigitated capacitor couplers (Figure 6.2) for resonances of various bandwidths.

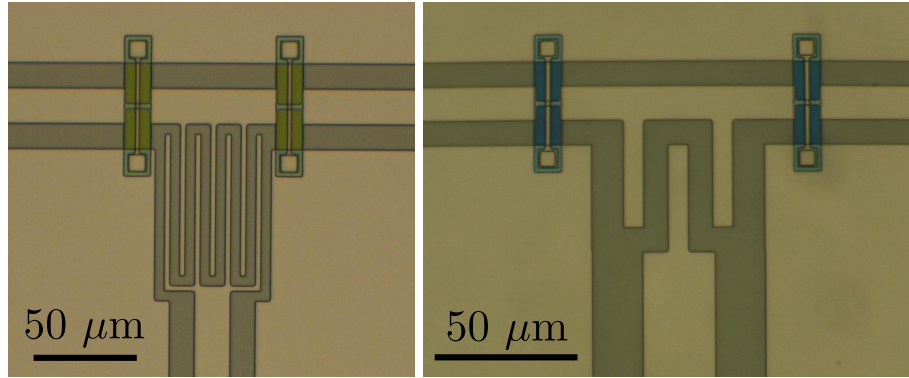


Figure 6.2: Photos of interdigitated capacitors coupling resonators to the feedline.

Straps connect the ground planes on either side of the feedline. These straps are critical for consistent Q and resonance spacing. Without them, oscillating voltage on the capacitor drives a coupled slotline mode on the feedline. This mode cannot propagate off the chip and therefore develops standing waves. These standing waves mean that the feedline presents a different effective impedance to resonators at different positions on the chip.

As the ground strap crosses over the feedline it changes the capacitance to ground and can create an impedance discontinuity. The feedline must constrict under the ground strap to maintain continuous impedance. Simulations in Microwave Office led to the design in Figure 6.3.

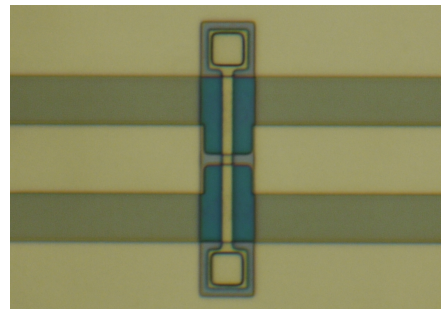


Figure 6.3: Closeup of one of the bridges connecting the ground planes on either side of the feedline.

6.1.3 Critical Current

The standard trilayer process for the NIST dc-SQUID has a critical current density of $J_c = 50 \mu\text{A}/\mu\text{m}^2$. A $10 \mu\text{m}^2$ junction requires ($\lambda \approx 1/3$) a SQUID loop inductance of $L_S \approx 2 \text{ pH}$ to ensure non-hysteretic operation. As this inductance is prohibitively small, we developed a $J_c = 1.5 \mu\text{A}/\mu\text{m}^2$ trilayer, with which a μm^2 junction requires a loop inductance of $L_S \approx 8 \text{ pH}$, still a small inductance, but reasonable to fabricate in our cleanroom.

From this critical current Equation 2.160 predicts that at the optimal flux bias, the flux noise due to the HEMT amplifier should be roughly $0.35 \mu\Phi_0/\sqrt{\text{Hz}}$ for the SQUIDs with matched coupling.

6.1.4 Coil Geometry

A SQUID is unfortunately sensitive to flux from magnetic fields in the environment, such as Earth's field, or the fields from magnetic materials in a telescope, cryostat, or office chair. Earth's field drives a magnetic flux quantum through a loop as small as $10 \mu\text{m} \times 10 \mu\text{m}$. This pickup degrades the SQUID as an amplifier of the current through a specific low-temperature detector. Coil gradiometry (Figure 6.4) can greatly reduce this pickup.

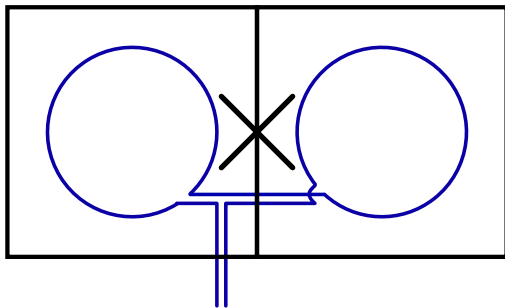


Figure 6.4: Schematic of a parallel, two-lobe (first-order) gradiometer with input coil.

Series gradiometry consists of twisting a loop so that it only couples to field gradients. Parallel gradiometry consists of orienting parallel lobes so that they couple to a uniform field with opposite polarity; screening current flows around the circumference of the gradiometer, bypassing the Josephson junction,

cancelling the flux from a uniform field and leaving equal and opposite flux in the two lobes. Note that in a parallel gradiometer the mutual inductance between input coil and SQUID is that of a single lobe, but the SQUID self-inductance is divided by the number of lobes.

Gradiometric coils couple to higher-order terms in the multipole expansion of the magnetic field. Distant sources produce dipole magnetic fields, and nearer sources can produce quadrupole fields, but the winding of the input coil can generate octopole or even higher-order fields.

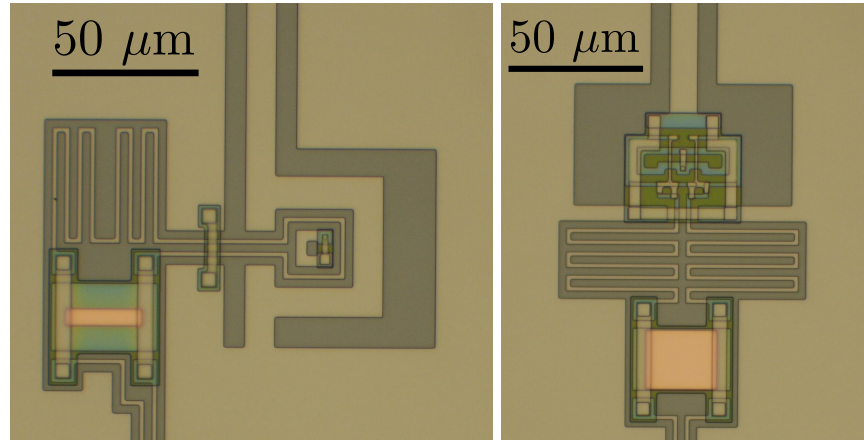


Figure 6.5: Photo of a non-gradiometric rf SQUID (left) and a two-lobe (first-order) gradiometric rf SQUID (right) each inductively coupled to the current antinode of a resonator in $\mu\text{mux}07\text{a}$. Both photos show the input filter consisting of a meander inductor shunted with a copper resistor.

$\mu\text{mux}07\text{a}$ incorporated both non-gradiometric and first-order parallel gradiometric SQUID designs (Figure 6.5). We used simulations of the coupling between the resonators and the SQUIDs to match the peak-to-peak shift in resonance frequency to the resonator bandwidths, intentionally overcoupling some SQUIDs and undercoupling others.

6.2 Filter Design

Microwave power from a resonator can potentially leak out on flux bias lines, degrading Q_i or even affecting the low-temperature detector on the input. To prevent this we placed inductive chokes on the input lines (Figure 6.5).

The inductive chokes may be unnecessary, as any connection with a low-temperature detector is likely to be made with wire bonds (~ 1 nH/mm). We chose to avoid microwave analysis of the low-frequency wiring and of the low-temperature detectors. To further eliminate the low-frequency input circuit from the microwave analysis, we shunted the inductive chokes with resistors, forming high-bandwidth L/R filters on the input lines.

6.3 Results

Measurements of $\mu\text{mux}07\text{a}$ confirmed that we could fabricate multiple superconducting microwave resonators on a chip, and that the resonance frequencies of the resonators shifted periodically with magnetic flux in the SQUID. The dissipationless rf SQUIDs showed low open-loop flux noise at 100 kHz.

6.3.1 Resonance Spacing

We surveyed S_{21} of a $\mu\text{mux}07\text{a}$ chip across wide frequency range. Not all resonances yielded, and some clearly shifted from their design frequencies (Figure 6.6). The remaining resonances were spaced by roughly 40 MHz with Q_i varying between 20,000 and 40,000 and Q_c varying between 2,000 and 6,000.

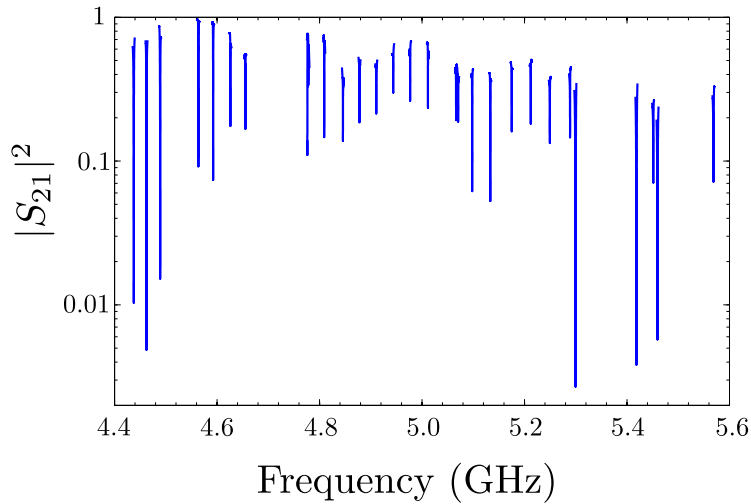


Figure 6.6: Survey of the $\mu\text{mux}07\text{a}$ resonances.

6.3.2 Flux-variable Resonance Frequency

These microwave resonances shifted with magnetic flux in their respective SQUIDs in full agreement with the theory in Section 2.2.4. The transmission S_{21} traversed a circle in the complex plane, so that the strongest response was in the imaginary component of S_{21} at an excitation frequency roughly halfway between the resonance frequency extrema. At high microwave powers the resonance curves distorted from pure Lorentzian shapes.

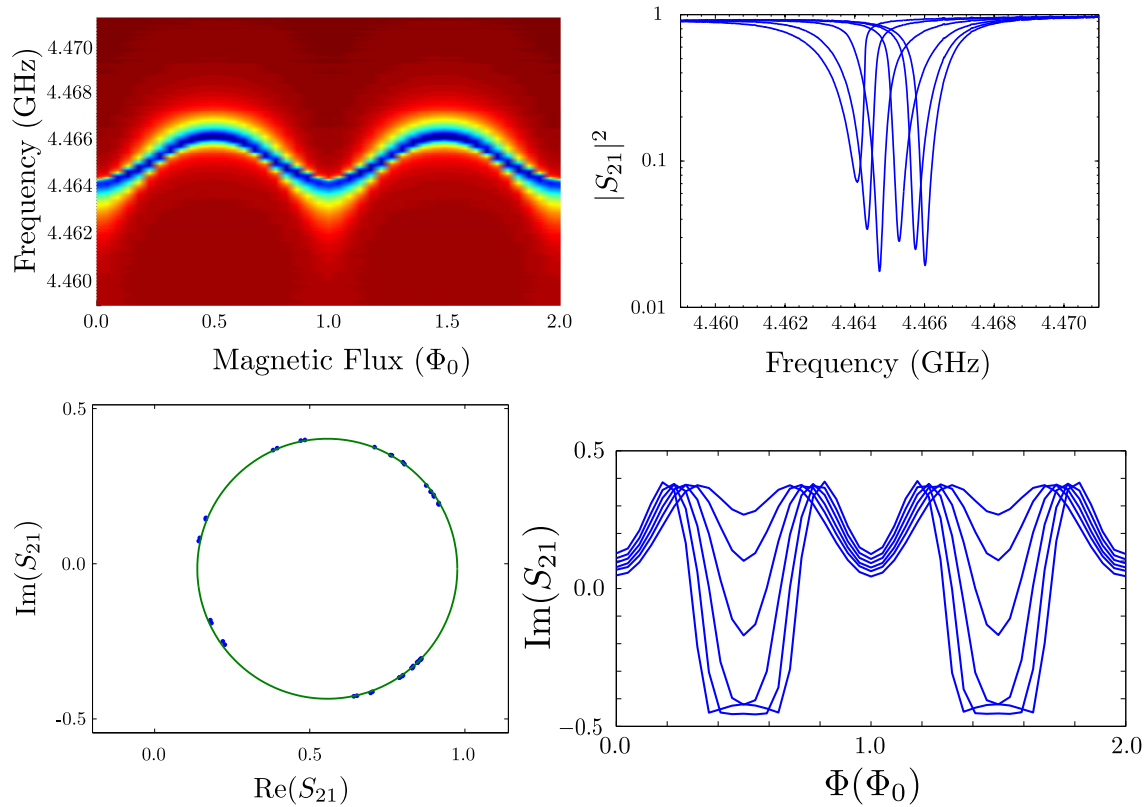


Figure 6.7: Variation of a μmux07a resonance with magnetic flux in the SQUID. Clockwise from the color map: $|S_{21}|$ in color (blue is no transmission, red is unity transmission) as a function of both frequency and magnetic flux, Lorentzian dips in transmitted power at different flux biases, $\text{Im}[S_{21}]$ as a function of flux at different excitation frequencies, S_{21} in the complex plane at one excitation frequency and multiple flux bias values. These data were obtained at excessive microwave power, which distorts the resonance shape.

Figure 6.7 shows the first SQUID/resonator pair we examined in $\mu\text{mux}07\text{a}$ [63]. It is strongly overcoupled, so that variation in flux in the SQUID can shift the resonance with respect to a stationary excitation to make the excitation on resonance or almost completely off resonance.

This coupling strength means that a strong microwave excitation can drive the resonator to bifurcation[76]. When the resonance frequency shifts dramatically over one period of the microwave excitation, the resonator can occupy either of two modes which differ in the phase relationship between the microwave excitation on the feedline and the standing wave in the resonator and in internal power. The switching between these bistable modes disrupts any flux-locked loop or flux-ramp modulation scheme.

6.3.3 Flux Noise

To measure open-loop flux noise we bias to a steep slope of the $\text{Im}[S_{21}]$ vs. Φ curve, measure output noise, and divide it by the slope of the curve. The results indicate the flux noise we would obtain operating the SQUID in a flux-locked loop. The flux noise with flux-ramp modulation is worse by at least a factor of $\sqrt{2}$ than the open-loop flux noise at the modulation frequency. This penalty is even worse for overcoupled SQUIDs because their response is not sinusoidal.

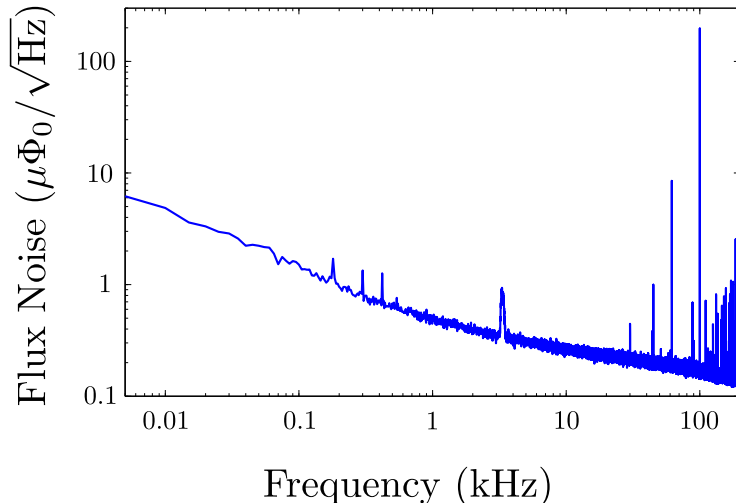


Figure 6.8: Flux noise of a $\mu\text{mux}07\text{a}$ SQUID/resonator. The noise falls to $0.17 \mu\Phi_0/\sqrt{\text{Hz}}$ at 100 kHz. The 100 kHz tone comes from a known input flux that calibrated the measurement.

Using the homodyne measurement setup from Figure 4.2 to read out the SQUID, we observed open-loop flux noise falling from $5 \mu\Phi_0/\sqrt{\text{Hz}}$ at 10 Hz to $0.17 \mu\Phi_0/\sqrt{\text{Hz}}$ at 100 kHz (Figure 6.8). Few SQUIDs have ever demonstrated noise this low[88].

The low self-inductance of the SQUID limits the input coupling due to the fact that $M_{in} \leq \sqrt{L_s L_{in}}$ and a $20 \mu\text{m} \times 20 \mu\text{m}$ area cannot accommodate a large number of turns of the input coil. The input coupling for this SQUID was only $M_{in} \approx 5 \text{ pH}$ so the open-loop input current noise was roughly $100 \text{ pA}/\sqrt{\text{Hz}}$, comparable to the output current noise of many TES designs.

6.3.4 Flux-ramp Modulation

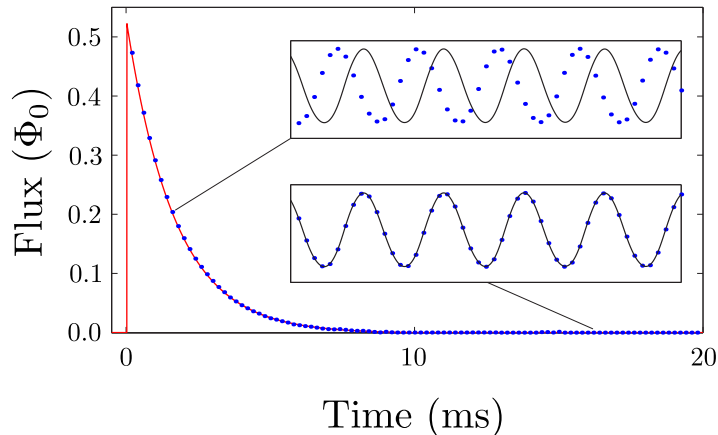


Figure 6.9: Demonstration of flux ramp demodulation performed with μmux07a reproducing an input pulse and exponential decay.

Since the μmux07a SQUIDs have only a single input coil, we could not fully implement flux-ramp modulation. Instead, we drove the SQUIDs with the sum of a 5 kHz, $10 \Phi_0$ sawtooth and a variety of slow functions, e.g. an exponential decay with a $\tau \approx 1.6 \text{ ms}$ time constant.

We began by Nyquist sampling the SQUID response and averaging the response to many ramps to form a Nyquist interpolated template function. We then performed a Wiener-optimal fit for the phase,

shifting the template function against each measured time trace, filtering the traces according to the power spectrum of the template.

We were able to reconstruct the slow input functions (Figure 6.9). The demodulated data matched the input functions without any additional fitting parameters because readout with flux-ramp modulation is linear according to $\phi = 2\pi \frac{\Phi}{\Phi_0}$.

6.3.5 Summary

μ mux07a demonstrated readout of a dissipationless rf SQUID coupled to a superconducting microwave resonator. It showed we could achieve exceptionally low flux noise. It demonstrated flux-ramp demodulation to linearize the SQUID response. These results were promising and suggested the development of a Microwave SQUID Multiplexer with stronger input coupling to the SQUIDs for lower input current noise.

Chapter 7

μ mux09a: Low Input Current Noise

7.1 Design

μ mux09a was our first attempt to make a dissipationless rf SQUID for TES readout, meaning a SQUID matched to the bandwidth of its resonator, with low input current noise, low environmental pickup, and two flux bias lines. We therefore appropriated the design of the NIST dc-SQUID for time-division multiplexing and adapted it for microwave operation.

7.1.1 Resonator Design

The resonator CPW expanded to a 20 μ m center conductor with 13 μ m gaps to reduce the two-level system frequency noise. We again coupled 33 resonators to the feedline with a target spacing of roughly 30 MHz.

7.1.2 Resonator-Feedline Coupling

μ mux09a included several design splits, with coupling capacitors tuned for $Q_c \approx 400, 900, 10,000$, and 40,000. We will focus on results for the design for $Q_c \approx 900$.

7.1.3 Critical Current

The NIST dc-SQUID has a self-inductance of roughly 20 pH, requiring ($\lambda \approx 1/3$) a junction with a critical current of roughly $I_c = 5 \mu$ A. The fabrication team at NIST developed a $J_c = 0.5 \mu$ A/ μ m² trilayer

process that allowed us to use a $10 \mu\text{m}^2$ junction area. From this critical current Equation 2.160 predicts a flux noise due to the HEMT amplifier of roughly $0.6 \mu\Phi_0/\sqrt{\text{Hz}}$.

7.1.4 Coil Geometry

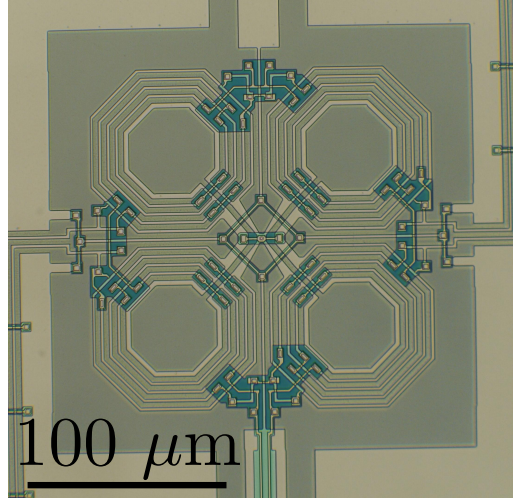


Figure 7.1: Photo of a second-order gradiometric rf SQUID inductively coupled to the resonator. ($\mu\text{mux}09\text{a}$)

This SQUID loop is a second-order gradiometer consisting of four parallel lobes arranged like a cloverleaf (Figure 7.1). Each lobe uses a slotted washer design with the input coil and feedback coil running in the slots to minimize their capacitive coupling to the SQUID. The orientation of the lobes alternates around the SQUID, making the SQUID insensitive to first-order gradients as well as uniform fields.

The flux bias coils alternate orientation from lobe to lobe and therefore generate fields that couple strongly to the gradiometer. The flux-ramp coil makes a half-turn around each lobe and the input coil makes one and a half turns around each lobe. The size of these lobes enables input coupling of $M_{in} \approx 85 \text{ pH}$.

Since metal traces on the chip can re-broadcast uniform fields from the environment as higher-order fields, we took care to symmetrize metal around the chip, either by 180° around the junction, or by reflection across the axis of the resonator.

7.1.5 SQUID-Resonator Coupling

There are several ways to couple microwave flux into the SQUID. Each design has a different inductance matrix between the SQUID, resonator, flux-ramp coil, and input coil. We simulated different designs with FastHenry[89] so that we could match the peak-to-peak shift in resonance frequency to the resonator bandwidth.

7.1.5.1 Direct Coupling

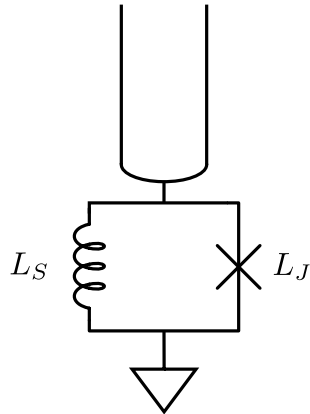


Figure 7.2: Circuit diagram for an rf SQUID directly coupling to the current anti-node of a resonator.

The theory we developed in Section 2.1 considers inductively coupled rf SQUIDs, but anti-node current flowing directly through the rf SQUID (Figure 7.2) produces a similar effect. Instead of a peak-to-peak change in termination inductance of

$$\Delta L_{pp} = \frac{2M_c^2}{L_J(1 - \lambda^2)} \quad (7.1)$$

direct coupling gives a peak-to-peak change of

$$\Delta L_{pp} = \frac{2\lambda^2 L_J}{1 - \lambda^2} \quad (7.2)$$

For $L_J \approx 60 \text{ pH}$, $\lambda \approx 1/3$, $Z_1 \approx 50 \Omega$, and $f_0 \approx 6 \text{ GHz}$ the peak-to-peak frequency shift in response to magnetic flux is

$$\Delta f_0 = \frac{4f_0^2 L_{pp}}{Z_1} \quad (7.3)$$

$$= \frac{4f_0^2}{Z_1} \frac{2\lambda^2 L_J}{1 - \lambda^2} \quad (7.4)$$

$$= \frac{4(6 \text{ GHz})^2}{50 \Omega} \frac{2\frac{1}{9}(60 \text{ pH})}{1 - \frac{1}{9}} \quad (7.5)$$

$$\approx 30 \text{ MHz} \quad (7.6)$$

Direct coupling is therefore ideal for very high-bandwidth resonances. We tested directly coupled SQUIDs in $\mu\text{mux}07\text{a}$, but have since focused on narrower bandwidth resonances.

7.1.5.2 Weak Inductive Coupling

Antinode current that splits around the SQUID before it returns to ground (Figure 7.3) weakly couples flux into the SQUID. The current that wraps around the SQUID is closer than the return current on the ground plane and therefore creates a non-zero magnetic field in the lobes of the SQUID. The flux is stronger in the two lobes closer to the resonator and changes sign from left to right, therefore coupling to the gradiometric SQUID. This design does not require the resonator wiring to cross over the SQUID wiring.

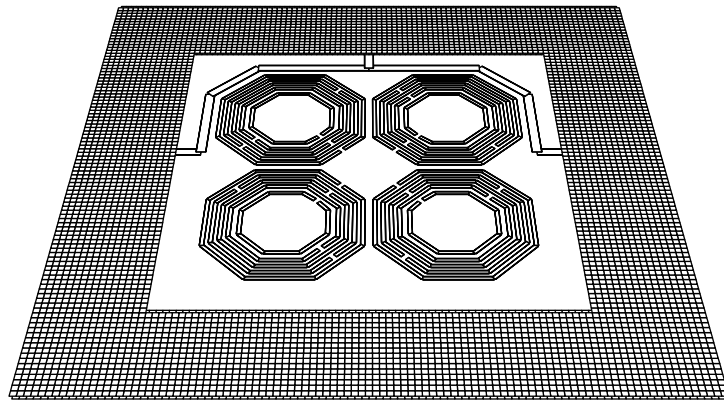


Figure 7.3: FastHenry model of a weak inductive coupling between the resonator and the SQUID. Crossovers are implemented with virtual connections.

M_{ij} (pH)	SQUID	Ramp	Input	Resonator
SQUID	18.9	30.9	87.5	1.65
Ramp		312	115	3.64
Input			1044	8.81
Resonator				77.6

Table 7.1: Simulated inductance values for a weak inductive coupling between the resonator and the SQUID.

The simulation (Figure 7.3 and Table 7.1) gives inductance values that determine the maximum frequency shift in response to flux:

$$\Delta f_0 = \frac{4f_0^2}{Z_1} \frac{2\lambda M_c^2}{L_S(1 - \lambda^2)} \quad (7.7)$$

$$= \frac{4(6 \text{ GHz})^2}{50 \Omega} \frac{\left(\frac{2}{3}\right)(1.65 \text{ pH})^2}{(18.9 \text{ pH})(1 - \frac{1}{9})} \quad (7.8)$$

$$\approx 310 \text{ kHz} \quad (7.9)$$

This weak inductive coupling is ideal for the narrowest bandwidth resonances that we can reliably space by ten times their bandwidth. We use this coupler design for the high- Q splits of $\mu\text{mux}09\text{a}$ and for $\mu\text{mux}10\text{b}$, adjusting the distance between the coupler and the SQUID to exactly match the design bandwidth.

7.1.5.3 Strong Inductive Coupling

Antinode current that wraps completely around two lobes strongly couples flux into the SQUID. This design also generates a field with the appropriate second-order gradients to couple magnetic flux into the SQUID gradiometer. For symmetry, current can continue directly down to the ground plane along the line of symmetry, but it does not couple flux into the gradiometer. This design requires the resonator wiring to cross over the SQUID wiring.

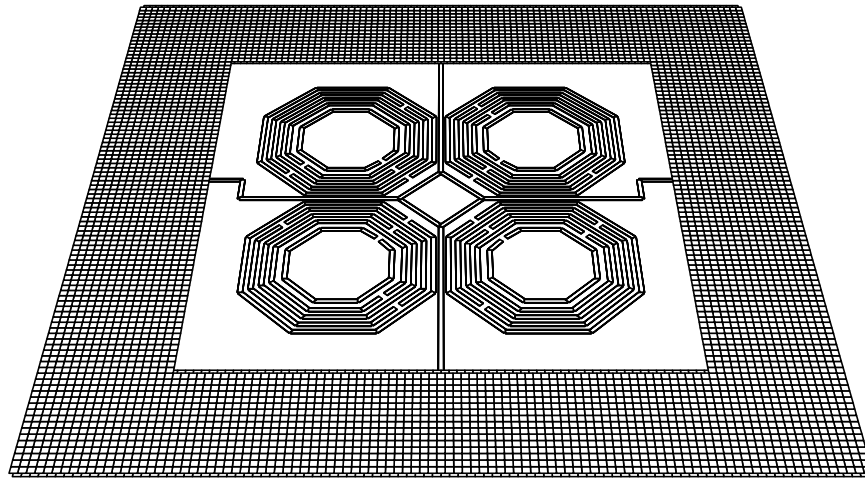


Figure 7.4: FastHenry model of a strong inductive coupling between the resonator and the SQUID. Crossovers are implemented with virtual connections.

M_{ij} (pH)	SQUID	Ramp	Input	Resonator
SQUID	17.9	28.9	82.5	9.42
Ramp		308	104	20.2
Input			1017	51.9
Resonator				145

Table 7.2: Simulated inductance values for a strong inductive coupling between the resonator and the SQUID.

The simulation (Figure 7.4 and Table 7.2) gives inductance values that determine the maximum frequency shift in response to flux:

$$\Delta f_0 = \frac{4f_0^2}{Z_1} \frac{2\lambda M_c^2}{L_S(1 - \lambda^2)} \quad (7.10)$$

$$= \frac{4(6 \text{ GHz})^2}{50 \Omega} \frac{\left(\frac{2}{3}\right)(9.42 \text{ pH})^2}{(17.9 \text{ pH})(1 - \frac{1}{9})} \quad (7.11)$$

$$\approx 11 \text{ MHz} \quad (7.12)$$

The stronger SQUID-resonator coupling causes a much larger frequency shift. We use this coupler design for the low- Q splits of μmux09a .

7.1.5.4 Adjustable Inductive Coupling

We finally simulated a design that allows tunable coupling across a wide range. Since resonator current that flows to ground along the line of symmetry does not couple flux into the gradiometric SQUID, we can adjust the coupling of the strong inductive coupler by changing the distribution of current between the three branches to ground. We add inductance on the side branches to make a larger fraction of the current flow along the line of symmetry.

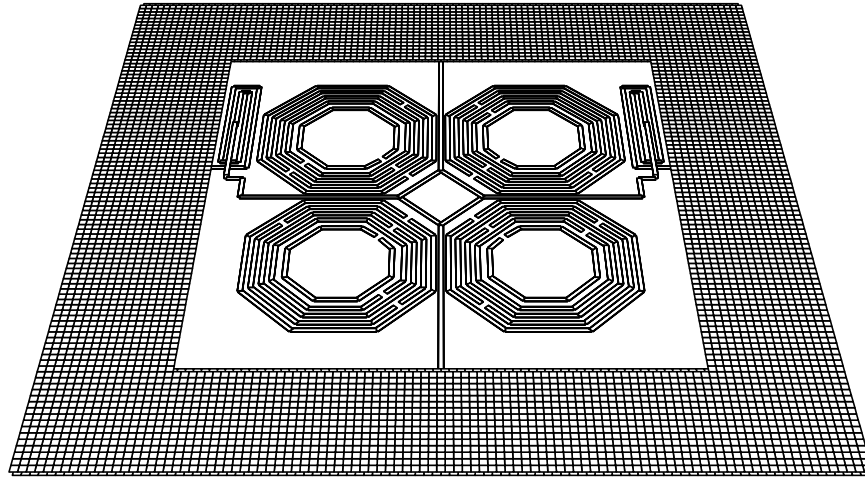


Figure 7.5: FastHenry model of a variable inductive coupling between the resonator and the SQUID. Crossovers are implemented with virtual connections.

M_{ij} (pH)	SQUID	Ramp	Input	Resonator
SQUID	18.3	29.7	84.6	5.46
Ramp		310	108	11.7
Input			1028	30.3
Resonator				186

Table 7.3: Simulated inductance values for a variable inductive coupling between the resonator and the SQUID.

The simulation (Figure 7.5 and Table 7.3) gives inductance values that determine the maximum frequency shift in response to flux:

$$\Delta f_0 = \frac{4f_0^2}{Z_1} \frac{2\lambda M_c^2}{L_S(1 - \lambda^2)} \quad (7.13)$$

$$= \frac{4(6 \text{ GHz})^2}{50 \Omega} \frac{\left(\frac{2}{3}\right)(5.46 \text{ pH})^2}{(18.3 \text{ pH})(1 - \frac{1}{9})} \quad (7.14)$$

$$\approx 3.5 \text{ MHz} \quad (7.15)$$

The extra inductance on the coupling branches reduces the SQUID-resonator coupling so that the frequency shift is intermediate between the strong and weak inductive coupling designs. We have not fabricated a coupler of this design in a real device, but it may be useful in the future.

7.2 Filter Design

The stronger input coupling requires stronger microwave blocking filters (Figure 7.6) on both the flux-ramp and input coils.

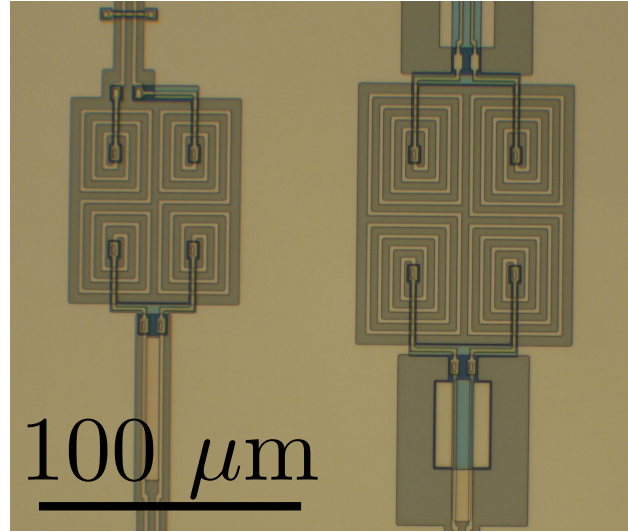


Figure 7.6: Photo of the input filters that block microwave power from reaching the input circuits.

With $L_F \approx 7 \text{ nH}$ and $R_F \approx 0.2 \Omega$, Equation 2.145 sets a limit on the internal quality factor due to losses in the filter on flux-ramp coil of $Q_f \approx 5 \times 10^5$. The limit on the quality factor due to the input coil

filter is even higher. We have observed $Q_i > 2 \times 10^6$ in bare resonators, so it is possible for the filter to set the Q_i of the resonator, but $Q_i \approx 5 \times 10^5$ is enough to make the power losses in a multiplexer insignificant in comparison to TES bias power.

7.3 Results

Measurements of $\mu\text{mux}09\text{a}$ proved that complex SQUIDs work well in microwave resonant circuits. These SQUIDs demonstrated low input current noise. The flux-ramp modulation wire did not yield in this fabrication, so we could not demonstrate flux-ramp modulation.

7.3.1 Resonance Spacing

We surveyed S_{21} of a $\mu\text{mux}09\text{a}$ chip designed for $Q_c \approx 400$ across wide frequency range. All resonances yielded, spaced by roughly 30 MHz, with one shifting from its design frequency to interfere with another (Figure 7.7).

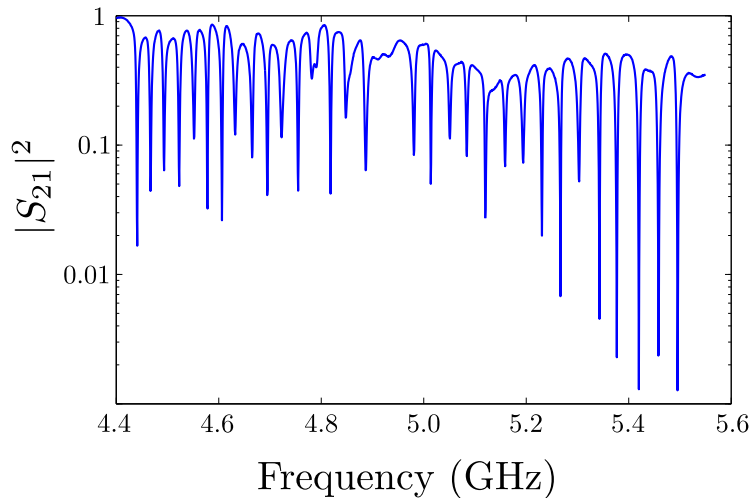


Figure 7.7: Survey of the $\mu\text{mux}09\text{a}$ resonances on a chip designed for $Q_c \approx 400$. The 4.8 GHz dip is actually two colliding resonances. One resonance is not shown.

7.3.2 Flux-variable Resonance Frequency

The microwave resonances shifted in agreement with theory in response to magnetic flux (Figure 7.8).

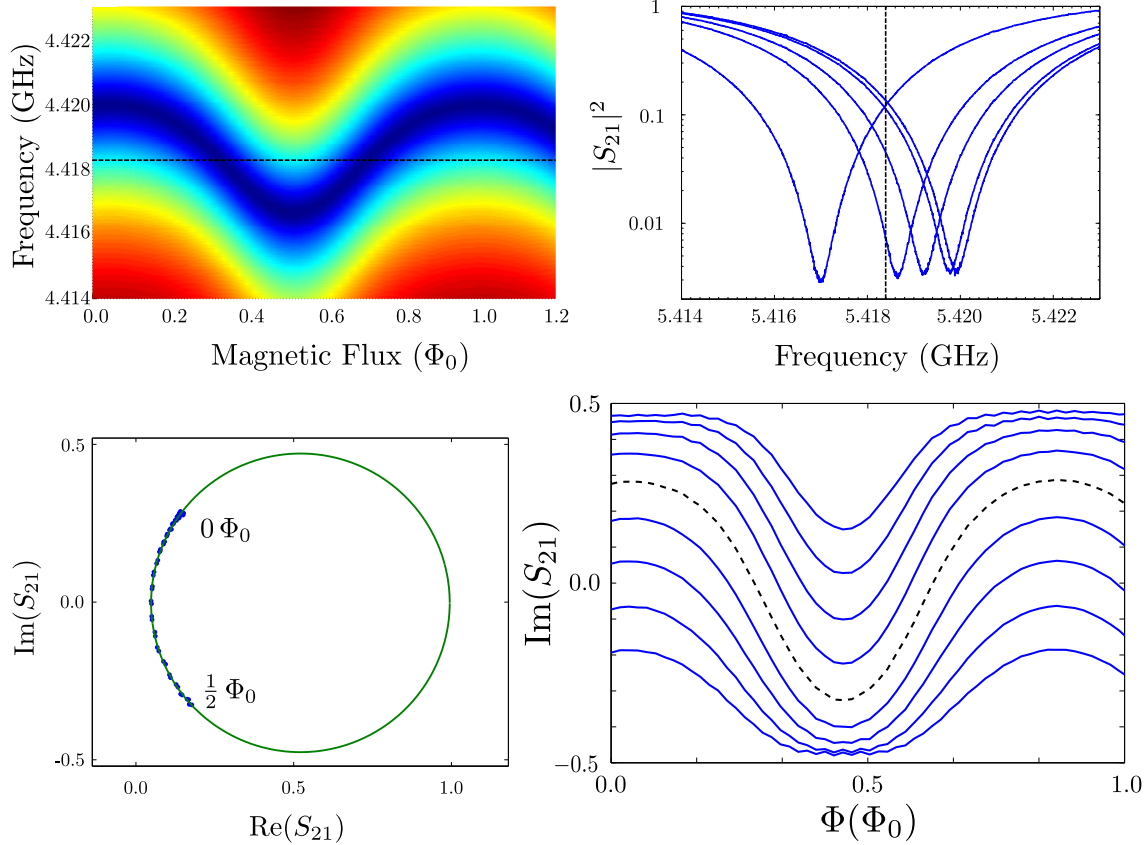


Figure 7.8: Variation of a $\mu\text{mux}09\text{a}$ resonance with magnetic flux in the SQUID. Clockwise from the color map: $|S_{21}|$ in color (blue is no transmission, red is unity transmission) as a function of both frequency and magnetic flux, Lorentzian dips in transmitted power at different flux biases, $\text{Im}[S_{21}]$ as a function of flux at different excitation frequencies, S_{21} in the complex plane at one frequency as a function of flux bias.

The resonance in Figure 7.8 was slightly undercoupled. Since the peak-to-peak shift in resonance frequency of this resonance was less than the bandwidth of the resonance, we could find a microwave excitation frequency for which $\text{Im}[S_{21}]$ was almost sinusoidal, making it well-suited to operation with flux-ramp modulation. Unfortunately, several vias on the flux-ramp line failed to yield, preventing us from demonstrating true flux-ramp modulation and demodulation until $\mu\text{mux}10\text{b}$.

7.3.3 Flux Noise and Current Noise

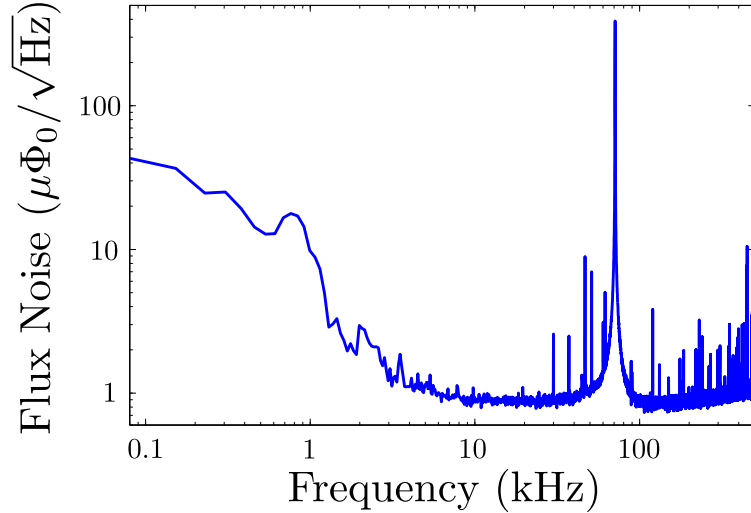


Figure 7.9: Flux noise of a $\mu\text{mux}09\text{a}$ SQUID/resonator. The noise falls to roughly $0.8 \mu\Phi_0/\sqrt{\text{Hz}}$ at 100 kHz.

The 71 kHz tone is due to an input flux oscillation that calibrates the measurement.

The $Q_c \approx 900$ resonances and wide CPWs caused the noise to reach the HEMT limit at much lower frequencies (Figure 7.9). The larger inductance of $\mu\text{mux}09\text{a}$ also raised this noise floor. The flux noise reached roughly $0.8 \mu\Phi_0/\sqrt{\text{Hz}}$ at 100 kHz, which is higher than the flux noise of $\mu\text{mux}07\text{a}$ but comparable to the flux noise of the NIST dc-SQUIDS.

The larger $\mu\text{mux}09\text{a}$ SQUID design allowed stronger input coupling of $M_{in} = 87.5 \text{ pH}$. Therefore while flux noise increased, current noise fell to $19 \text{ pA}/\sqrt{\text{Hz}}$. With flux-ramp modulation we expect this current noise to degrade to roughly $30 \text{ pA}/\sqrt{\text{Hz}}$, which would allow readout of many transition-edge sensors without degradation.

7.3.4 TES Readout

To demonstrate the utility of this multiplexer we obtained several TES chips designed for CMB polarimetry and interface chips with appropriate shunt resistors. We bonded a pair of these to the $\mu\text{mux}09\text{a}$ (Figure 7.10) and measured noise with the SQUID biased at a steep slope of its response curve.

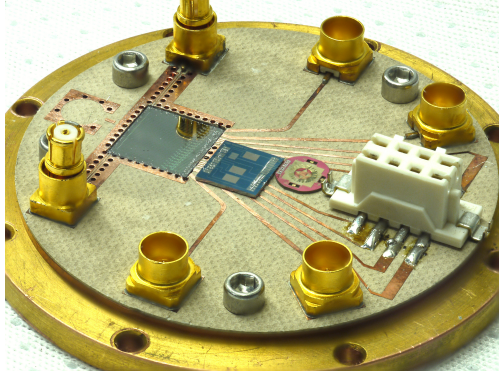


Figure 7.10: Photo of a μ mux09a chip wired for readout of a CMB TES chip.

We measured a noise-equivalent power (Figure 7.11) with a plateau at $3 \times 10^{-17} \text{ W}/\sqrt{\text{Hz}}$, matching measurements of the same TES in a dc-SQUID system. The NEP rolled off at the thermal bandwidth of the TES. It showed significant excess noise at low frequencies that we attribute to pickup on the heater line.

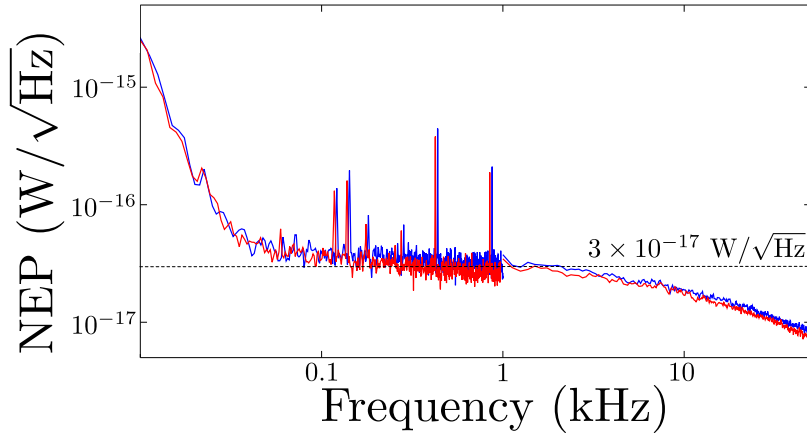


Figure 7.11: Noise-equivalent power of a TES for CMB polarimetry, measured with μ mux09a. The two curves were taken at two different TES bias points.

The excess noise did not depend on TES resistance, which indicated that it was a true power noise. Pickup on the heater lines is a common problem for TES readout with Time-Division Multiplexing as well and requires careful filtration to eliminate. See Section 8.5 for a measurement of NEP without heater lines.

7.3.5 Summary

μ mux09a demonstrated microwave readout of a complex rf SQUID with high input mutual inductance. The strong input coupling of this SQUID produced low input current noise. We used this device to read out a CMB TES (Figure 7.10), but could not prove non-degrading readout at low frequencies because of pickup on the heater lines.

Chapter 8

μ mux10b: Multiplexer for CMB TESs

8.1 Design

μ mux10b was our first attempt to make a practical Microwave SQUID Multiplexer for arrays of TESs, specifically targeting the NIST CMB polarimeters. We packed the resonances tightly enough to fit 600 in an octave of bandwidth between 4 GHz and 8 GHz. We optimized the design to improve yield and enable flux-ramp modulation. We used a 20 mm \times 3 mm chip that matches the NIST time-division multiplexer with an identical layout of bond pads that allows us to easily couple to any detector chip designed for readout with the NIST time-division multiplexer.

8.1.1 Resonator Design

We wanted the μ mux10b resonances to fit in a 275 MHz band to match the open-source electronics described in Section 4.1. We chose to fill this band with 35 resonances, 33 to leverage the similarity with the NIST 1 \times 33 time-division SQUID multiplexer and two for diagnostics. The number of resonances and the bandwidth indicate a spacing of roughly 6 MHz, which would allow more than 600 in the 4-8 GHz band. To avoid cross-coupling between resonances, the resonator bandwidth must be no more than 600 kHz (Section 2.3.9), so we chose to use the weak inductive coupler design, spacing the resonances by twenty times their bandwidth, with $BW \approx 300$ kHz and $Q_c \approx 16,000$.

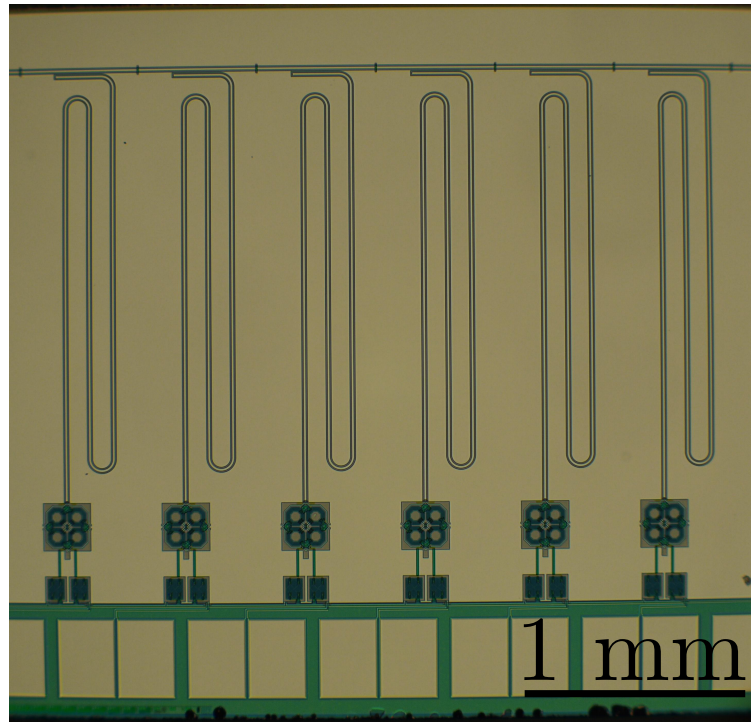


Figure 8.1: Photo of an arrangement of trombone resonators, each slightly different in length.

To fit on the 3 mm wide chip the roughly 5 mm long resonators meander like trombones (Figure 8.1), changing the slider length by $3 \mu\text{m}$ between adjacent resonators so that $\Delta l = 6 \mu\text{m}$ and the frequency spacing is close to 6 MHz. We also reverted to CPWs with $10 \mu\text{m}$ center strips and $6 \mu\text{m}$ gaps.

8.1.2 Resonator-Feedline Coupling

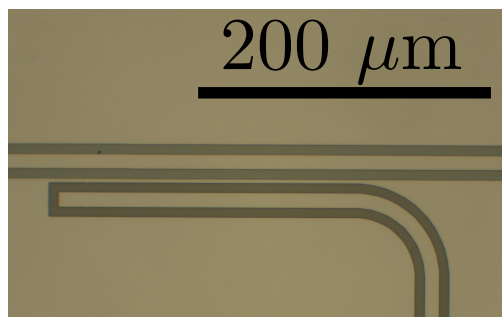


Figure 8.2: Photo of the elbow coupler in μmux10b .

$\mu\text{mux}10\text{b}$ used an elbow coupler (Figure 8.2) designed for $Q_c \approx 16,000$. The elbow coupler simply brings the resonator close to the feedline for an extended length, with a narrow strip of ground plane between them.

This coupler is not compact, but allowed us to quickly fabricate and test a single-layer design ($\mu\text{mux}10\text{a}$). Measurements of $\mu\text{mux}10\text{a}$ showed that low inductance connections between ground planes are critical for reliable resonator placement and consistent Q .

8.1.3 Coil Geometry

We optimized the SQUID design and tuned the weak-inductive coupling to match the resonance frequency shift to the 300 kHz bandwidth (Figure 8.3).

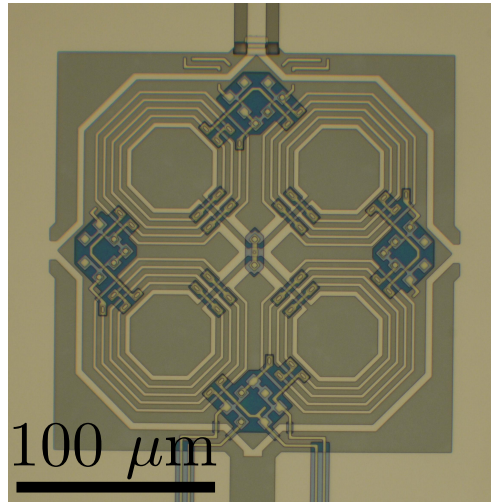


Figure 8.3: Photo of a second-order gradiometric rf SQUID inductively coupled to the resonator. ($\mu\text{mux}10\text{b}$)

We changed the design to comply with conservative design rules, particularly with regard to vias, to improve fabrication yield. We also reduced the amount of insulator in the SQUID. The insulator dielectric can be a source of loss and two-level system noise, although the effect is weak at the current anti-node of the resonator, where the electric field is smallest.

8.1.4 Filter Design

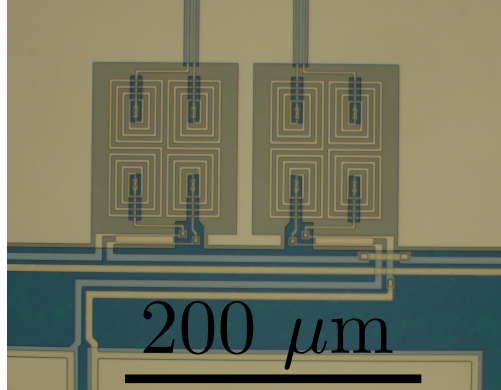


Figure 8.4: Photo of the input filters that block microwave power from reaching the input circuits.

We adapted the input filters slightly for the new SQUID design (Figure 8.4). Loss in the filters places a limit of $Q_i < 5 \times 10^6$. We also moved these filters farther away from the SQUID to make room for a low impedance connection between the ground planes on either side of the resonator.

8.2 Results

Measurements of $\mu\text{mux}10\text{b}$ demonstrated accurate placement of resonators tightly spaced in frequency. We demonstrated linear readout of the SQUIDs with flux-ramp modulation. We demonstrated two-pixel multiplexing of SQUIDs and TESs. Finally we demonstrated measurement of TES devices for CMB polarimetry without degradation of the noise-equivalent power.

8.2.1 Resonance Spacing

We surveyed S_{21} of a $\mu\text{mux}10\text{b}$ chip across a 250 MHz band (Figure 8.5). Almost all resonances yielded, with only one shifting from its design frequency. The remaining resonances were spaced by roughly 6 MHz.

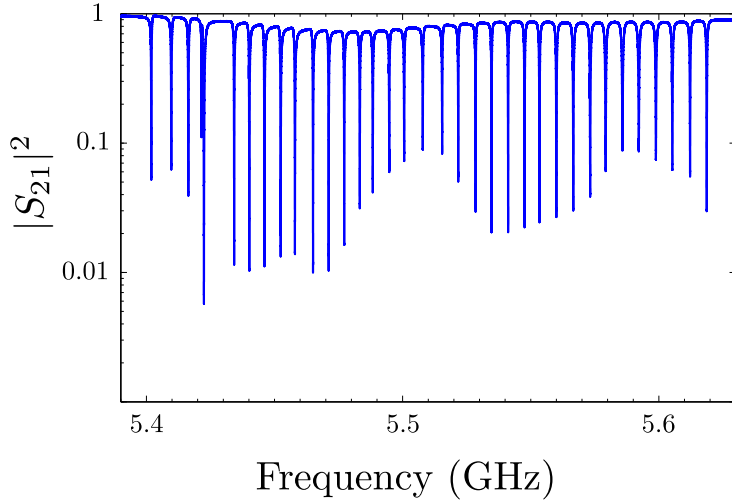


Figure 8.5: Survey of the μ mux10b resonances. The 5.42 GHz dip is the collision of two resonances.

The μ mux10b couplers targeted $Q_c \approx 16,000$, but measured Q_c and Q_i varied significantly across the chip (Figure 8.6), although less than in previous designs. Time-domain reflectometry measurements showed significant reflection at the microwave launch. Reflections at the microwave launches could produce a standing wave on the feedline and change Q_c by changing the effective impedance the feedline presents to the coupling capacitor. The variation in Q is small enough that all resonances are useful for readout.

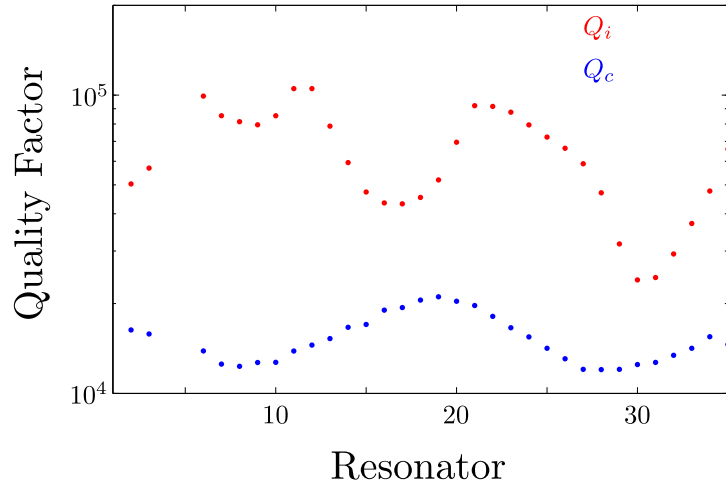


Figure 8.6: Internal and coupling quality factors for the resonances across a μ mux10b chip.

Variation in Q_i is less important so long as Q_i is large enough to not limit the bandwidth or dissipate excessive power at the cold stage. We do not yet understand why the Q_i of a chip that has been through the full SQUID fabrication process is lower than that of a chip with bare niobium resonators.

8.2.2 Flux-variable Resonance Frequency

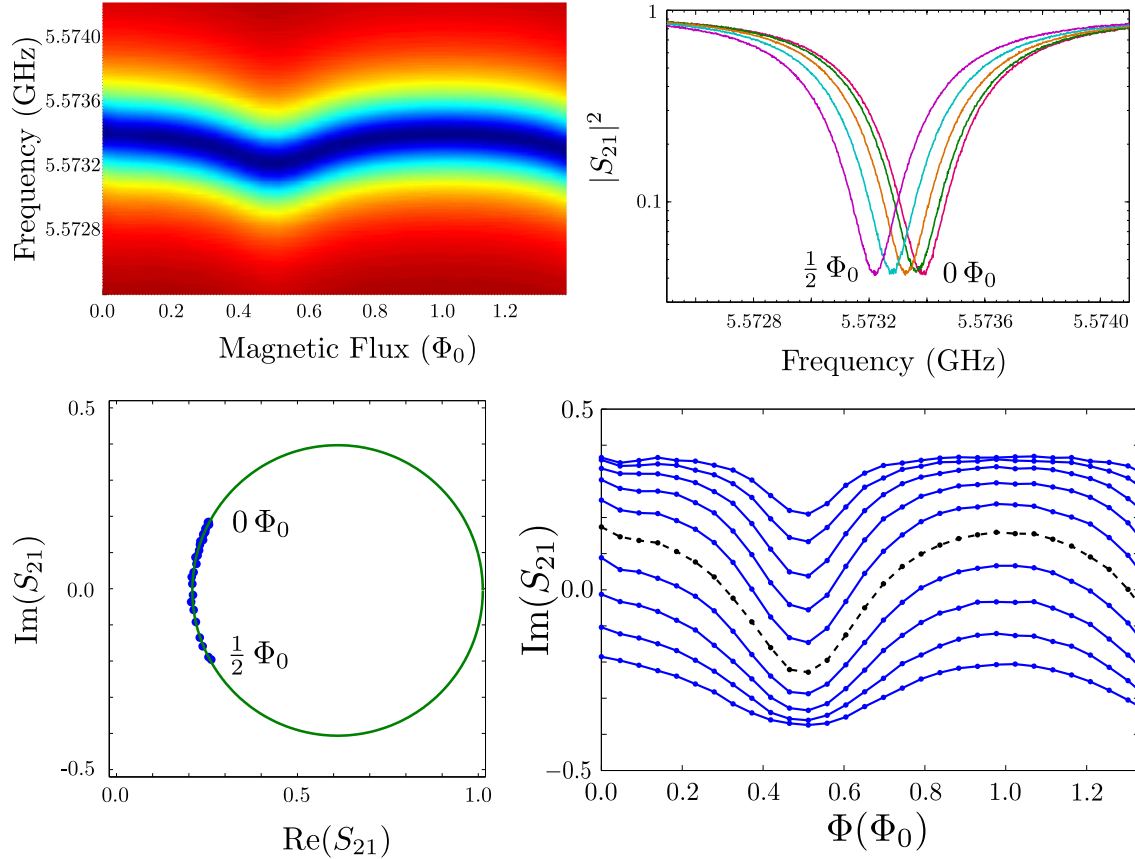


Figure 8.7: Variation of a μ mux10b resonance with magnetic flux in the SQUID. Clockwise from the color map: $|S_{21}|$ in color (blue is no transmission, red is unity transmission) as a function of both frequency and magnetic flux, Lorentzian dips in transmitted power at different flux biases, $\text{Im}[S_{21}]$ as a function of flux at different excitation frequencies, S_{21} in the complex plane at one frequency as a function of flux bias.

This SQUID/resonator pair from μ mux10b is slightly undercoupled (Figure 8.7) and at the appropriate measurement frequency its response in the imaginary component of S_{21} is approximately sinusoidal with flux,

with the deviation matching $\lambda \approx 1/3$. Current on the flux-ramp line shifts all resonances together and current on the individual input lines shifts individual resonances (Figure 8.8).

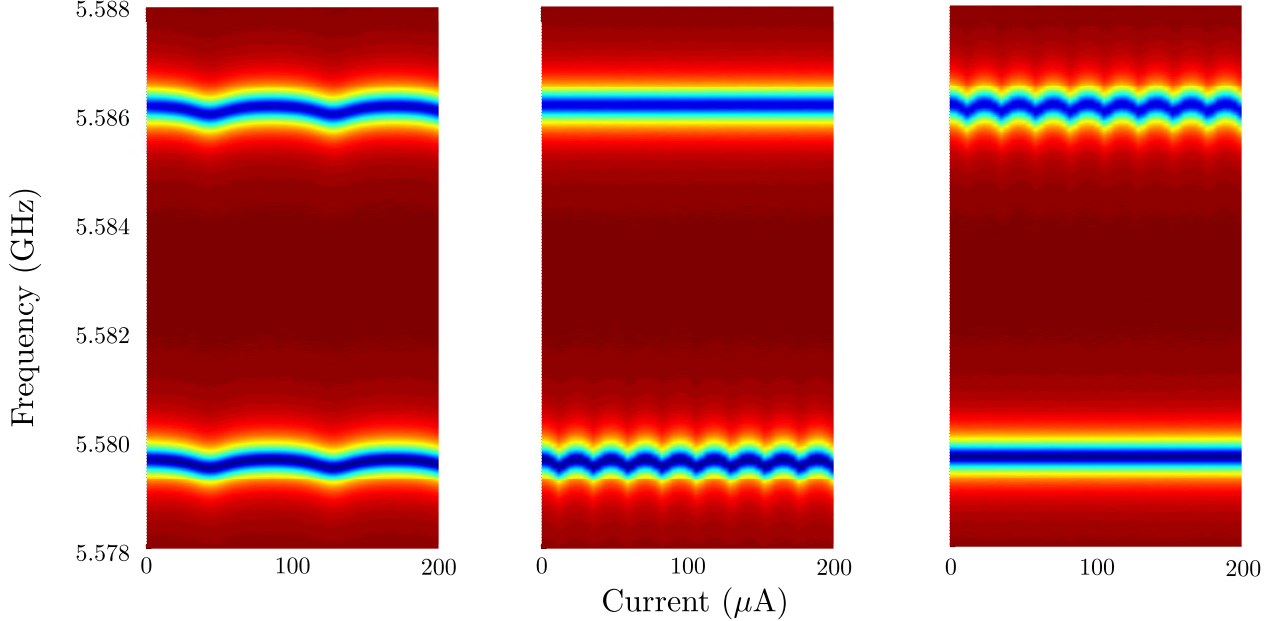


Figure 8.8: Variation of two $\mu\text{mux}10\text{b}$ resonances with current through their common (left) or individual (center and right) flux bias lines. The color plots show $|S_{21}|$ in color (blue is low, red is high) as a function of both frequency and current

The periodicity of the $\mu\text{mux}10\text{b}$ response implies coupling inductances of $M_{fr} \approx 24 \text{ pH}$ and $M_{in} \approx 88 \text{ pH}$, which are quite close to the simulated values.

8.2.3 Flux Noise and Frequency Noise

The increase in Q and reversion to a narrower CPW resulted in the two-level system noise dominating the HEMT noise even at 100 kHz, as shown by the difference in noise spectrum of the two quadratures (Figure 8.9). HEMT noise should appear equally in both quadratures, but TLS noise, as a fluctuation of resonance frequency, should appear predominantly in the imaginary quadrature.

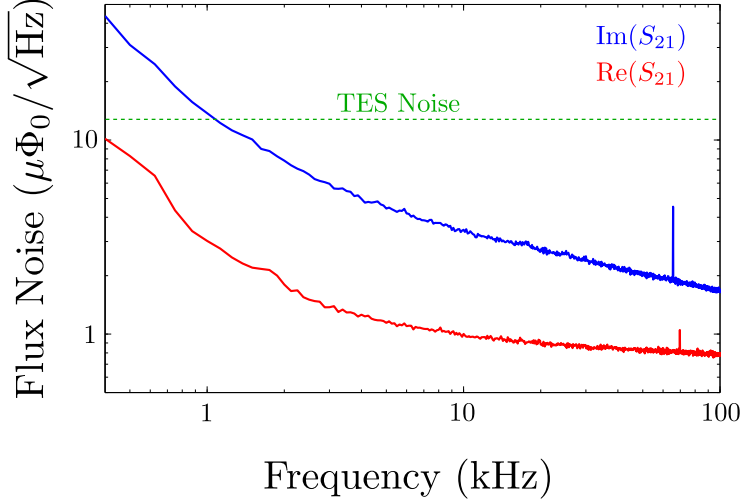


Figure 8.9: Noise of a μ mux10b SQUID/resonance referred to flux noise. The $\text{Re}[S_{21}]$ noise has been scaled by the same factor as the $\text{Im}[S_{21}]$ noise, even though there is no SQUID response in the amplitude direction, to show what a reduction in two-level system noise can achieve. The dashed line shows a representative TES current noise of $300 \text{ pA}/\sqrt{\text{Hz}}$.

The noise curves in Figure 8.9 show output noise in both $\text{Re}[S_{21}]$ and $\text{Im}[S_{21}]$ referred through the gain in $\text{Im}[S_{21}]$. There is no gain in $\text{Re}[S_{21}]$ and so the noise in that real quadrature does not refer to actual flux noise, but rather indicates what the flux noise would be without two-level systems, roughly $0.8 \mu\Phi_0/\sqrt{\text{Hz}}$ at 100 kHz. The noise of the imaginary quadrature is the actual open-loop flux noise, including two-level systems, which falls to roughly $1.6 \mu\Phi_0/\sqrt{\text{Hz}}$ at 100 kHz. These noise levels show that a roughly factor of two reduction in two-level system noise should restore HEMT-limited operation.

The open loop noise increased dramatically at low frequencies, so that without flux-ramp modulation the added noise of the Microwave SQUID Multiplexer would dominate the noise of a CMB TES below 1 kHz.

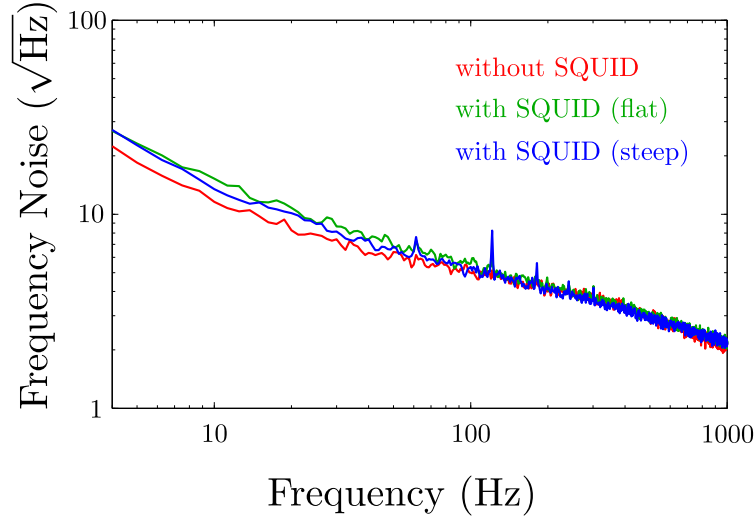


Figure 8.10: Low-frequency noise of $\mu\text{mux}10\text{b}$ resonances referred to frequency noise. The green and blue curves show noise for the same SQUID/resonator biased to be sensitive or insensitive to magnetic flux. The red curve shows noise for a resonator without a SQUID. The overlap of the green and blue curves shows that low-frequency flux noise in the SQUID is insignificant compared to TLS noise in the resonator. The other resonator could have a different density of two-level systems and was measured at a different internal power, so a slight deviation is expected.

Both fundamental noise mechanisms of an rf SQUID, flipping of magnetic dipoles on the loop[81] and critical current fluctuations in the junction[79][80], have $1/f$ frequency dependence. To investigate the contribution of these noise mechanisms we measured the frequency noise at different SQUID bias points. Output noise due to flipping magnetic dipoles should increase on the steep slopes of the SQUID response. Output noise due to fluctuations of the critical current should increase on the flat slopes of the SQUID response. The frequency noise at different bias points appears identical (Figure 8.10), indicating that the two-level-system noise of the resonator dominates.

8.2.4 Flux Ramp Modulation

To evade the low-frequency noise in the resonator we modulate the SQUID signal up to higher frequencies, ideally to where the two-level system noise falls below the HEMT noise.

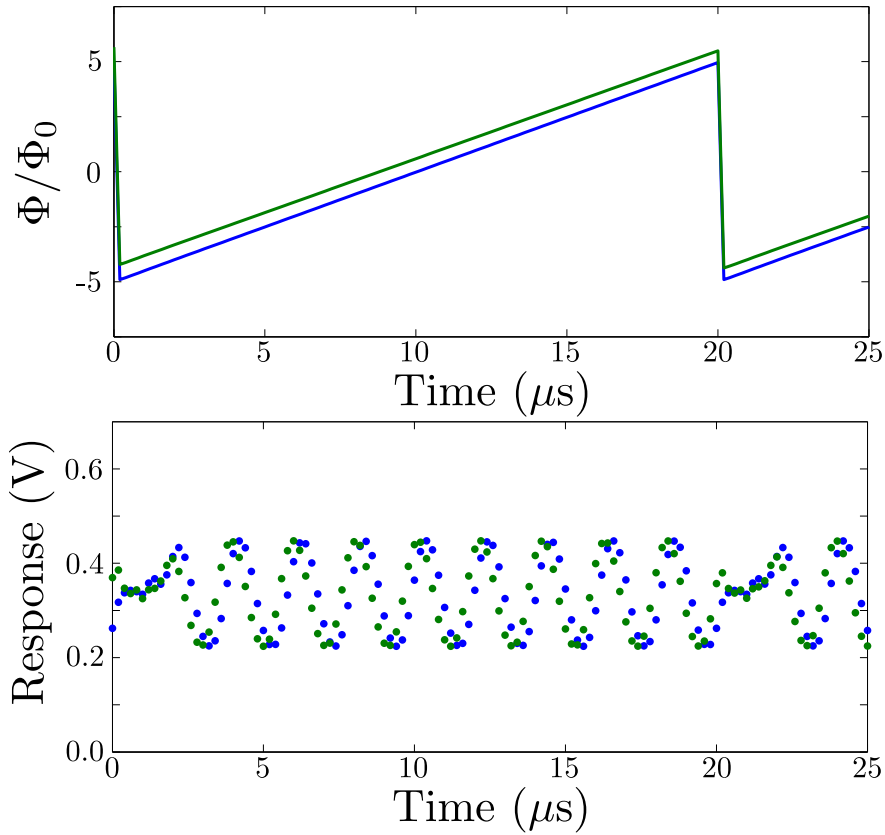


Figure 8.11: Flux ramp that repeatedly sweeps out the SQUID response of all resonators. An offset of the flux ramp causes a phase shift of the SQUID response.

We drive the flux-ramp line with a sawtooth (Figure 8.11) that sweeps through multiple flux quanta in the SQUIDs. The slew rate of this ramp must exceed that of any input signal. Therefore any input signal looks like a flux offset during the duration of the ramp, which produces a phase shift in the SQUID response to the ramp. This phase-modulation applies to all SQUIDs on a chip because the flux-ramp line couples to all SQUIDs.

Low-frequency signals shift the phase of the SQUID response while low-frequency noise from I_c fluctuations vary the amplitude of the SQUID response and low-frequency noise from two-level systems in the resonator vary the offset. We can therefore reject these sources of noise by extracting the phase of the SQUID response for each ramp.

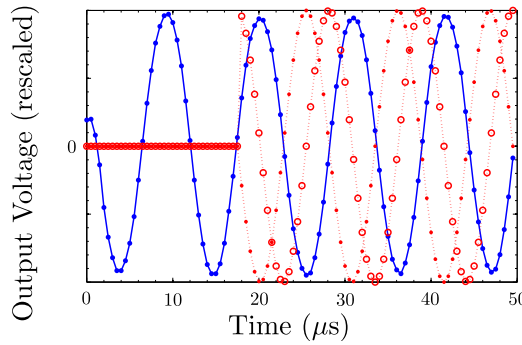


Figure 8.12: Illustration of the phase-fitting method. The phase is the arctangent of the ratio of the data (blue) multiplied by both red curves. We discard part of the response to let the ramp reset transient settle.

We had previously used a Wiener optimal fitting algorithm to extract the phase of the ramp response, but have since settled on the simple Fourier solution: knowing the frequency of modulation, we multiply the SQUID response by that frequency sine and cosine (Figure 8.12) and extract the phase angle:

$$\phi = \arctan \left(\frac{\sum x_t \sin \omega_m t}{\sum x_t \cos \omega_m t} \right) \quad (8.1)$$

This solution is computationally efficient and requires no knowledge of the precise shape of the SQUID response. It discards the information in higher harmonics of the SQUID response, but for matched coupling the power in the higher harmonics is low and this has little impact on the readout noise.

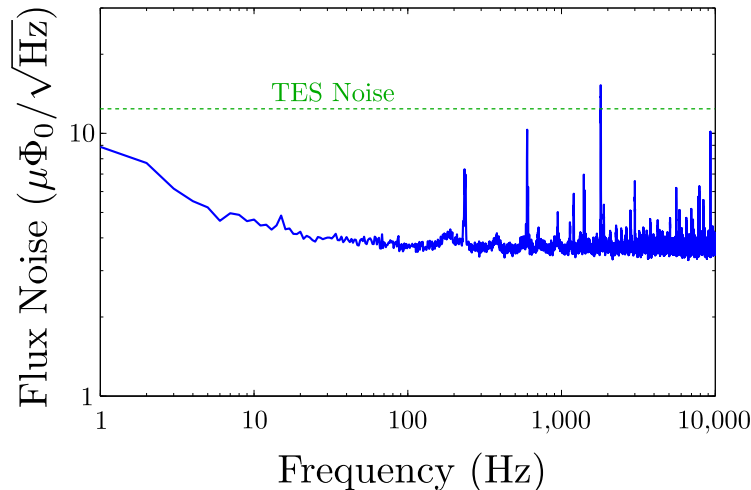


Figure 8.13: Flux noise after flux-ramp demodulation, with dashed line showing TES noise of $300 \text{ pA}/\sqrt{\text{Hz}}$.

For purely sinusoidal SQUID response, flux-ramp modulation imposes a $\sqrt{2}$ penalty (Equation 2.167) in flux noise compared with operation of the SQUID in a flux-locked loop because a substantial fraction of each ramp is spent measuring the SQUID at an extremum of its response curve where it is insensitive to changes in input flux. The noise further increases as we discard the ramp reset transient from the beginning of each ramp response and discard information in the higher harmonics. These factors combine to roughly double the flux noise compared to the open-loop noise at the modulation frequency (Figure 8.13).

The noise after modulation/demodulation is flat down to roughly 10 Hz and less than the noise of a CMB TES. This multiplexer is therefore suitable to read out a practical CMB TES instrument.

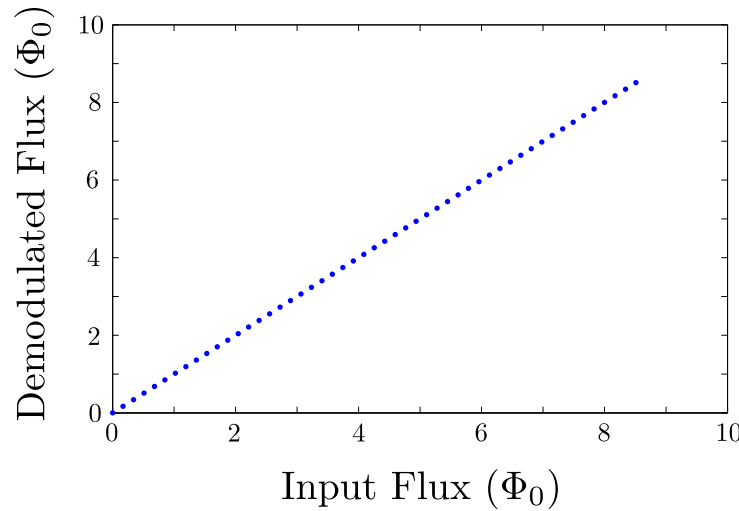


Figure 8.14: Flux ramp demodulation performed with μ mux10b showing linear response.

An important benefit of flux-ramp modulation is the fact that it linearizes the response of all SQUIDs on a chip using a single twisted-pair. The phase shift of the ramp response is simply $\phi = 2\pi\Phi/\Phi_0$. To verify this we measured readout linearity with flux-ramp modulation (Figure 8.14).

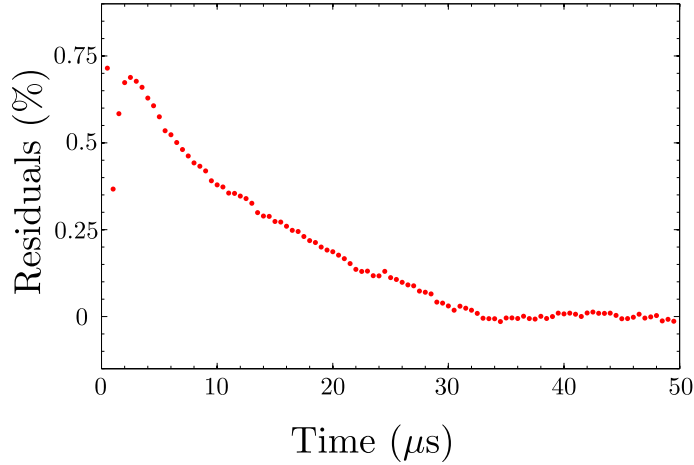


Figure 8.15: Difference between applied flux ramp and a perfectly linear ramp.

Since we do not compensate for the ramp reset transient, the flux ramp is not perfectly linear during its rise (Figure 8.15). This distortion affects the Fourier measurement differently at different phase shifts and therefore creates a readout non-linearity (Figure 8.16) that is periodic with flux in the SQUID. The current flux-ramp measurements are linear to roughly one part in 1,000, and should improve with better control of the flux ramp. This linearity is sufficient for most applications.

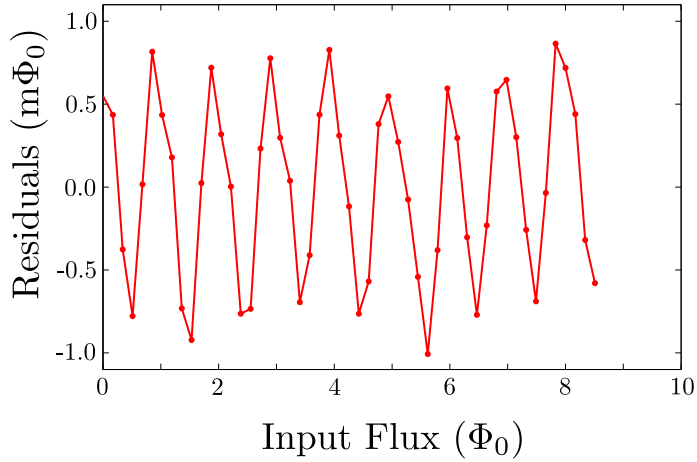
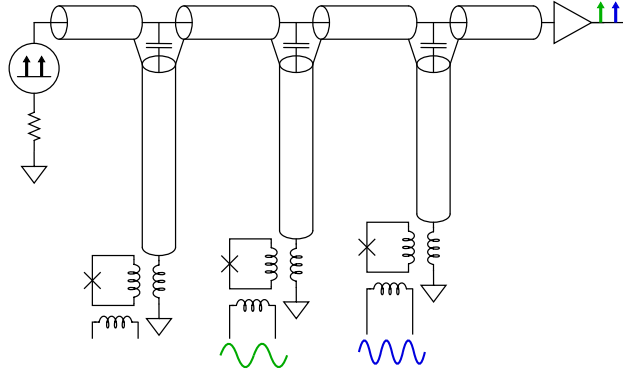


Figure 8.16: Measured non-linearity of the flux-ramp modulation scheme. The deviation from linearity is periodic with flux.

8.3 SQUID Multiplexing Demonstration

As a demonstration, we performed multiplexed readout of a pair of synthesized flux signals:



The signals from the two microwave resonators separated cleanly and reproduced the synthesized input signals (Figure 8.17). We detected no significant ac crosstalk between these synthesized flux signals.

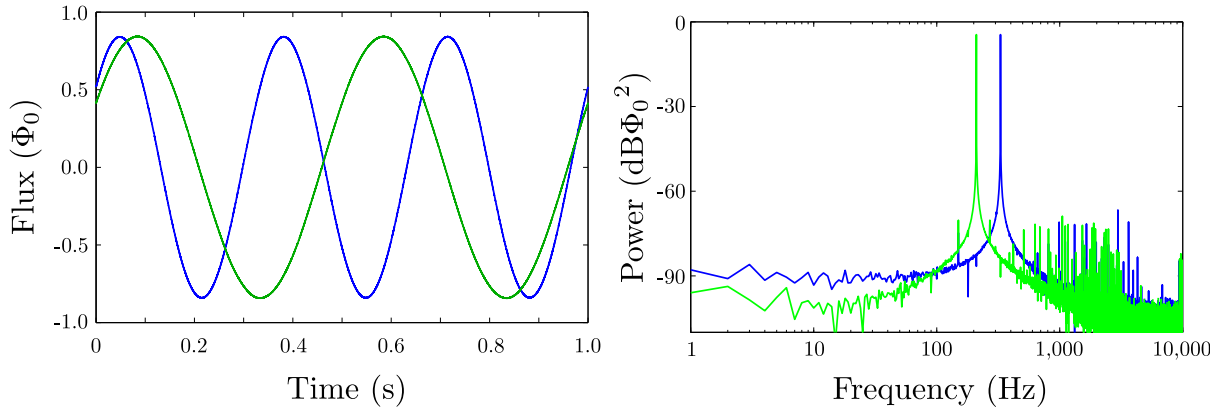


Figure 8.17: Multiplexed readout of two synthesized flux signals, at 2 Hz and 3 Hz (left). Power spectrum of two channels measuring synthesized signals at 210 Hz and 330 Hz (right).

A measurement of one SQUID with a slow sweep of flux in another indicates crosstalk at the part per 1,000 level (Figure 8.18). The periodicity of the crosstalk suggests that it occurs after the SQUID gain. It depends on the relative microwave power between the resonators and not on their separation in frequency,

which suggest that it occurs in the HEMT or the IQ-mixer, for example through load on the HEMT bias circuit affecting the gain for all microwave signals. This level of crosstalk is sufficient for most applications.

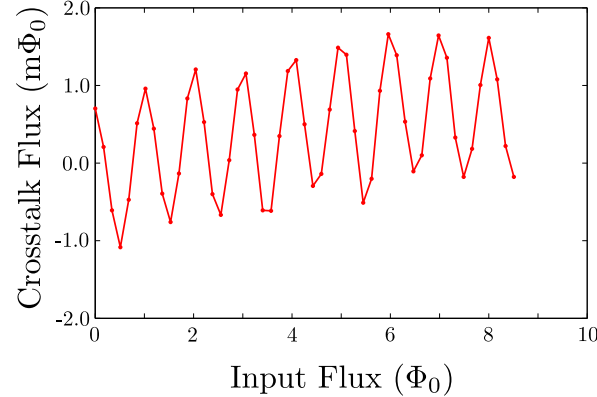


Figure 8.18: DC crosstalk of one channel into the other. The periodicity of the crosstalk indicates that it occurs on the output side of the SQUID, e.g. through the HEMT amplifier.

8.4 TES Multiplexing

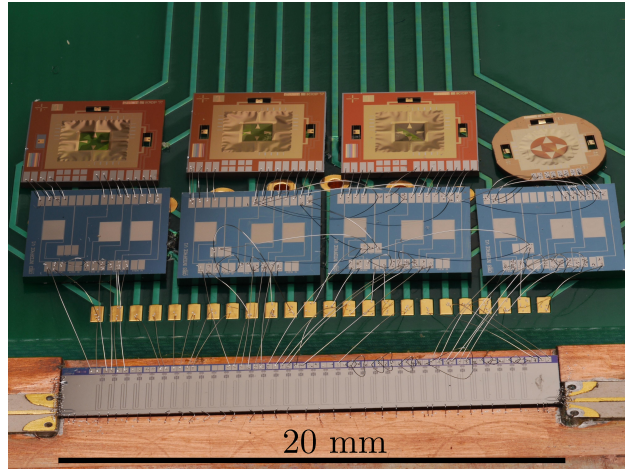


Figure 8.19: Photo of a μ mux10b chip wired for readout of several CMB TES chips. In a real array the detector chips would abut the multiplexer chip and use short wirebonds, or the detectors would be integrated on the multiplexer chip.

We obtained several NIST CMB TESs (Figure 8.19) intended for future measurements of the polarization B-mode signature of the cosmic microwave background[72], wired them to a μ mux10b chip, and used them to demonstrate multiplexed TES readout.

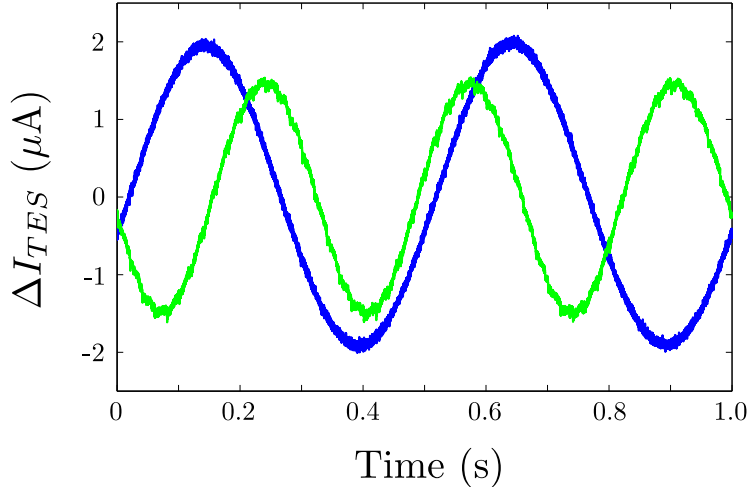


Figure 8.20: Multiplexed readout of two voltage-biased TES's responding to sinusoidal heater signals. Pickup on the heater lines accounts for the noisy signal.

These devices have heaters on the TES membranes that we used to inject power into the TESs. We synthesized detector signals and performed multiplexed readout of the TESs. The signals separated cleanly (Figure 8.20), constituting the first full demonstration of microwave frequency multiplexing of TESs. Unfortunately, pickup on the heater lines made the readout excessively noisy. Better filtration on the heater lines, or measurement of optical signals without heaters, should eliminate this effect in the future.

8.5 TES Readout

In order for this device to be considered for large scale TES arrays in the future, it is important to show that it does not degrade the TES sensitivity. We therefore removed the heater lines from the CMB pixels, biased them in their transition, and measured their noise-equivalent power using the Microwave SQUID Multiplexer (Figure 8.21).

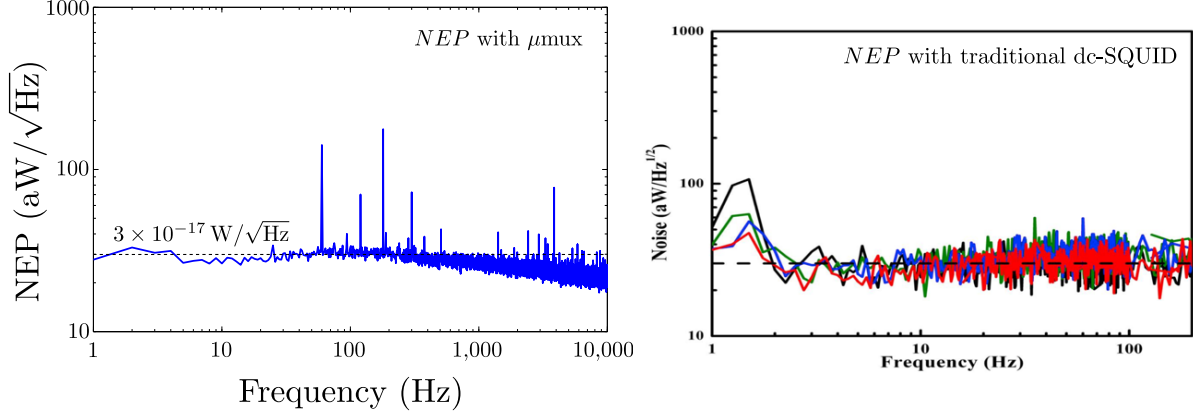


Figure 8.21: Noise-equivalent power of the TES in the transition taken with the Microwave SQUID Multiplexer (left) and a traditional dc-SQUID (right).

We used full flux-ramp modulation to read out the TES current and referred it to incident power through the TES voltage bias. We measured NEP of $3 \times 10^{-17} \text{ W}/\sqrt{\text{Hz}}$, precisely matching previous measurements of the same TES using a dc-SQUID readout. The NEP is flat down to 1 Hz in contrast to open-loop measurements like in Figure 8.10. This measurement, performed with two coaxial cables and one twisted-pair for the flux ramp exactly as we would multiplex a large array, constitutes proof that the Microwave SQUID Multiplexer does not degrade the sensitivity of the detector.

8.5.1 Summary

μmux10b demonstrated full flux-ramp modulation and demodulation, multiplexed SQUIDs with low-noise and low-crosstalk, and measured NIST TESs intended for polarimetry of the cosmic microwave background without any degradation of the noise-equivalent power. These results show that the Microwave SQUID Multiplexer is a viable option for multiplexed readout of low-temperature detector arrays.

Chapter 9

Future Work

9.1 Multiplexer Re-design

We have already designed the next generation of Microwave SQUID Multiplexer, incorporating the lessons of previous designs and attempting to improve input current noise to make the device suitable for TES detectors with higher operating resistance.

9.1.1 Surface State Reduction

We have seen evidence that the CF_4 sloped sidewall etch reduces Q_i , perhaps because of a suppression of superconductivity in the thinned edges of the niobium traces. Microwave currents flow mainly at the edges of the wires and some fraction of the resonator current could therefore pass through resistive niobium and dissipate power. We also worry about a possible increase in two-level systems on unprotected niobium surfaces during the insulator etch.

In the future, we intend to use a fabrication process that defines the resonator and most of the SQUID wiring in both layers of niobium, without insulator between them. This process hides the niobium surface that gets exposed to the insulator etch between the layers, where there is no electric field and therefore no sensitivity to two-level systems. The bottom surface of the resonator will be deposited on clean, HF-dipped silicon and the top surface will be protected by photoresist. This process will also restrict the CF_4 etch to the area immediately around crossovers and Josephson junctions. We expect this fabrication process to produce resonators with higher Q_i and lower two-level system noise, although we cannot predict the magnitude of improvement.

9.1.2 SQUID Design

The new SQUID design adds an extra loop inside each lobe of the gradiometer (Figure 9.1), reducing the self-inductance of the SQUID, and increases junction critical current to maintain $\lambda \approx 1/3$. These changes increase optimal microwave power on the feedline and reduce flux noise due to the HEMT. They also allow stronger input coupling: one full turn for the flux-ramp and two full turns for the input, which will further reduce input current noise.

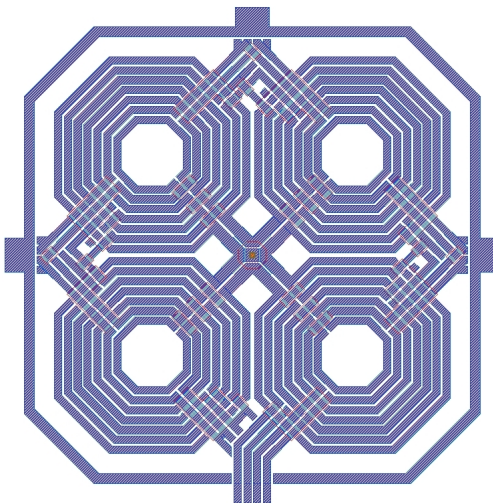


Figure 9.1: The layout for the rf SQUID in $\mu\text{mux}11\text{a}$.

9.1.3 Resonator Geometry

The new design widens the center strip of the coplanar waveguide to $s = 14 \mu\text{m}$ with $g = 8 \mu\text{m}$ gaps to reduce the two-level system noise[82]. The resonators will couple to the feedline with interdigitated capacitors for $Q_c \approx 10,000$ to further reduce the flux noise due to two-level systems. The SQUID-resonator coupling will increase to maintain the match between frequency shift and resonance bandwidth. We expect the combination of these changes with the process changes to make the flux noise HEMT-limited at 100 kHz.

Our goal is to make a multiplexer that adds only $30 \text{ pA}/\sqrt{\text{Hz}}$, capable of reading out many existing TES designs without degradation.

9.2 Microwave Launches

The variation of Q with position of the resonators on the chip suggests that there is a standing wave on the feedline, indicating reflections at the microwave launches. Time-domain reflectometry measurements support this theory. We intend to investigate the cause of these reflections and improve the microwave launch, for example by a flip-chip coupler, to eliminate them so that all input channels to the multiplexer require the same readout power and exhibit the same flux noise.

9.3 Room Temperature Electronics

The multiplexing demonstrations in this dissertation used two microwave signal generators to generate the tones for simultaneous readout of two pixels. In the future we plan to read out tens, hundreds, or thousands of pixels but we clearly cannot afford thousands of \$10,000 signal generators. Instead, we are collaborating with MKID groups and digital electronics engineers to create a digital solution: software defined radio (SDR) capable of digitally generating and demultiplexing hundreds of tones.



Figure 9.2: Open-source software-defined radio solution, designed and built by the Center for Astronomy Signal Processing and Electronics Research (CASPER).

We have received the first generation of open-source electronics for SDR from the collaboration (Figure 9.2). We intend to use it to demonstrate 33 pixel multiplexing of TESs, which, although not qualitatively different from 2 pixels, should increase confidence in the scalability of the Microwave SQUID Multiplexer.

9.4 Lumped-Element Resonators

Each resonator in μmux10b takes up a roughly $2.5 \text{ mm} \times 0.5 \text{ mm}$ footprint on the chip. We will need a more compact resonator design if we want to fit hundreds of resonators on a chip. A semi-lumped design, with a meander inductor and interdigitated capacitor can achieve the same resonance frequency using a $0.3 \text{ mm} \times 0.3 \text{ mm}$ area[90]. A true lumped-element design, with a spiral inductor and parallel-plate capacitor can achieve the same resonance frequency using even less area[91].

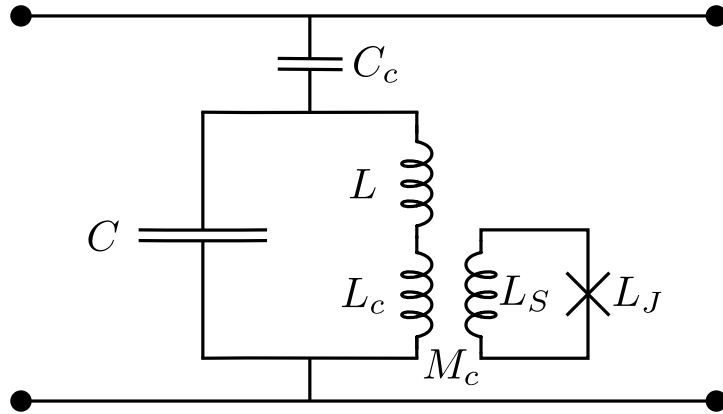


Figure 9.3: A resonator using lumped rather than distributed capacitance and inductance. Lumped-element resonators could significantly reduce the resonator footprint.

With multi-SQUID resonators (Section 9.5.1) or hybrid multiplexing techniques (Section 9.5.2), the footprint of the resonator may not be significant in future detector arrays.

9.5 Multiplexer Efficiency

Neither the Microwave SQUID Multiplexer nor the Microwave Kinetic Inductance Detector have high Shannon efficiency for the many applications that require very low bandwidth per pixel. The CMB polarimetry application we have been referring to requires only 100 Hz of bandwidth for each polarimeter, set primarily by the scan rate of the telescope on the sky. Efficient use of the microwave bandwidth would require a device with hundreds of thousands of resonators with $Q > 10^6$, spaced by roughly 10 kHz.

We cannot now fabricate devices with total Q that high and internal Q even higher. We cannot fabricate that many resonators on a chip. Most importantly, we cannot space the resonators that close together. We currently measure a roughly 1 MHz variation in resonance frequency placement, likely due to slight variations in over-etch, metal thickness, substrate thickness, etc. across the wafer. A similar scatter is observed with MKIDs. We must space the resonances at least 3 MHz apart to prevent a large number of collisions and excessive nearest-neighbor crosstalk (Section 2.3.9).

We would therefore use 3 MHz of bandwidth to measure a 100 Hz signal. We are pursuing more efficient use of the microwave bandwidth with multi-SQUID resonators and hybrid multiplexing schemes.

9.5.1 Multi-SQUID Resonators

One solution is to couple multiple SQUIDs to each microwave resonator and read out multiple input signals in its bandwidth. We can place multiple SQUIDs at the current anti-node and separate their signals by coupling them to the flux ramp with different mutual inductances (Figure 9.4), so that they modulate at different frequencies, e.g. 80 kHz, 100 kHz, and 120 kHz. Their input signals then appear in different sidebands of the microwave carrier (Figure 9.5).

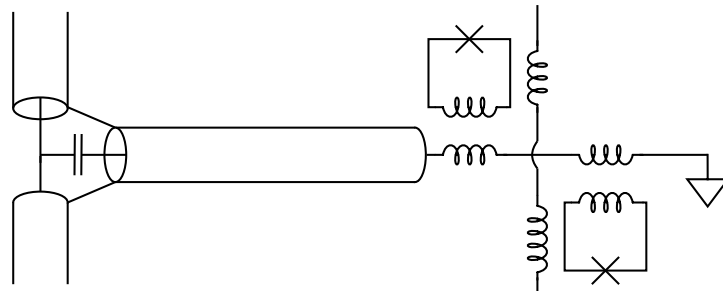


Figure 9.4: Two rf SQUIDs coupling to the same quarter-wave resonator. Note that the flux-ramp line couples with different strength to each SQUID.

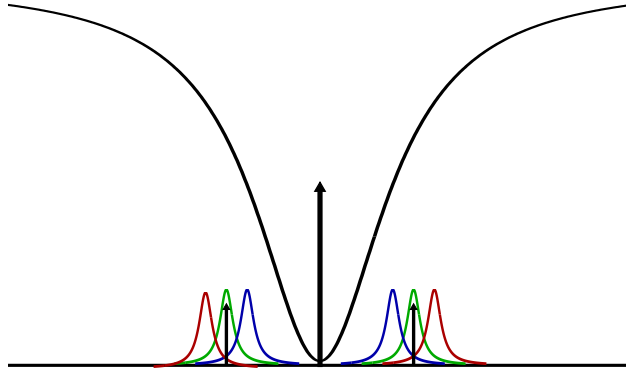


Figure 9.5: Different SQUIDs produce signals in different sidebands of the microwave carrier frequency.

The coupling between each rf SQUID and the resonator must be reduced by a factor of \sqrt{n} to maintain a match between total frequency shift and resonance bandwidth and prevent excessive coupling between the flux-ramp response of the different SQUIDs. The optimal readout power increases therefore by a factor of n and the voltage gain of each is reduced by \sqrt{n} . This strategy is therefore interesting but introduces a new mechanism for crosstalk and increases flux noise by \sqrt{n} .

9.5.2 Hybrid Multiplexing

Finally, let us consider hybrid multiplexing schemes. Hybrid multiplexing is a standard solution to reach higher Shannon efficiency in a variety of applications, for example 3G cell-phone communication[92].

The fundamental advantage of microwave multiplexing of SQUIDs is the output bandwidth of a coaxial cable, not the high Q that allows a large number of resonances per cable. Instead of multiplexing hundreds of thousands of narrow-band SQUIDs we can multiplex hundreds of wide-band SQUIDs. We can therefore use a Microwave SQUID Multiplexer to multiplex hundreds of high-bandwidth SQUIDs and low-frequency techniques to multiplex hundreds of low-bandwidth signals into each high-bandwidth SQUID.

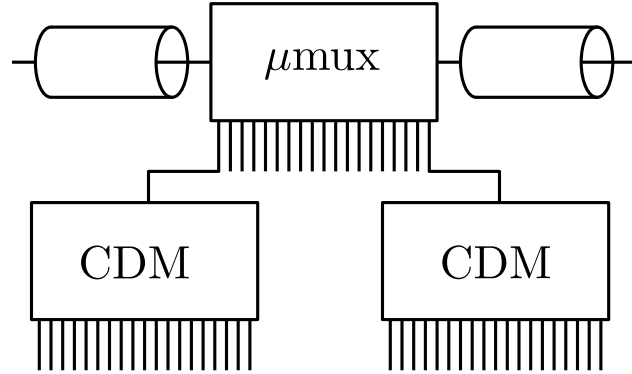


Figure 9.6: Each input channel of the Microwave SQUID Multiplexer can be fed by the output of a low-bandwidth multiplexer, e.g. a Code-Division Multiplexer.

Hybrid multiplexing of SQUIDs has been previously considered[93]. The complexity of combining two technologies is outweighed by the fact that we need not push the limits of either technology. The low-frequency multiplexing technology that seems to fit the Microwave SQUID Multiplexer best is a form of Code-Division Multiplexing with current-steering and binary addressing.

9.5.2.1 CDMA

This promising Code-Division Multiple Access (CDMA) scheme consists of SQUID switches steering TES current through inductors that couple with opposite polarity to the microwave SQUID. The SQUID switches allow rapid inversion of the flux signal from any TES. A Walsh code of inversions (Figure 9.7) provides a basis set that allows complete reconstruction of the input signals.

The code-division pre-multiplexer[53] can have very low power dissipation per pixel, on the order of the power dissipated in the TES bias circuit. It does not suffer the noise aliasing weakness of Time-Division Multiplexing, allowing larger multiplexing factors. Finally, because the switches are SQUIDs and therefore selected with flux modulo Φ_0 , it can use a binary addressing scheme to further reduce the wirecount.

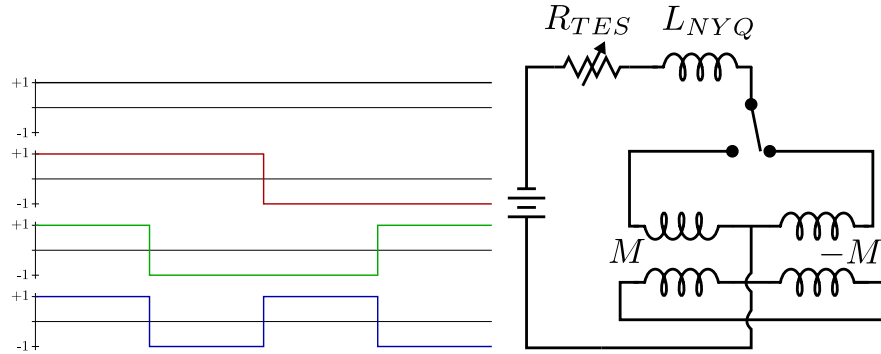


Figure 9.7: Inversion pattern for a 4-channel Walsh code for CDM (left). Schematic of current-steering implementation of CDM (right).

A Microwave SQUID Multiplexer with 256 channels, each fed by a Code-Division Multiplexer with 256 channels can read out 65536 pixels with high spectral efficiency. This type of hybrid multiplexer could read out a megapixel array using only 40 coaxial cables and 24 twisted-pairs. We intend to pursue this technology to provide a real megapixel multiplexing solution within the next ten years.

Chapter 10

Conclusion

We developed a microwave frequency multiplexer of dissipationless rf SQUIDs for the readout of large-scale arrays of low-temperature detectors. Such a multiplexer demanded scalability to large numbers of input channels, input current noise low enough to read out TESs without degradation, and low per-pixel power dissipation.

Using standard lithographic techniques we fabricated multiple superconducting microwave resonators on each multiplexer chip. These resonators had distinct resonance frequencies, similar bandwidths, and sufficiently low loss to limit the heat load to less than 5 pW per pixel.

Various designs exhibited flux noise as low as $0.17 \mu\Phi_0/\sqrt{\text{Hz}}$, input current noise as low as $20 \text{ pA}/\sqrt{\text{Hz}}$, and readout of a CMB TES pixel without degrading the noise-equivalent power of $3 \times 10^{-17} \text{ W}/\sqrt{\text{Hz}}$. Flux-ramp modulation avoided the low-frequency two-level system noise of the resonators and linearized the response of all SQUIDs using only a single twisted-pair for the entire multiplexer. Flux noise after modulation/demodulation remained flat to low frequencies.

Finally, we performed multiplexed readout of two SQUIDs driven by synthesized current signals and actual TES currents. The multiplexed signals separated cleanly with crosstalk of a part per 1,000.

These results indicate that the Microwave SQUID Multiplexer is suitable to read out arrays of thousands of low-temperature detectors. We are now working on hybrid multiplexing schemes to increase Shannon efficiency beyond what can be achieved with superconducting microwave resonators alone. This will enable readout of tens of thousands of detectors using two coaxial cables and a handful of dc wires, providing the multiplexing factors necessary for the megapixel arrays of the future.

Bibliography

- [1] C. Enss. Cryogenic particle detection (2005).
- [2] J. Bottomley and F. King. Philosophical Transactions of the Royal Society of London. Series A, Containing Papers of a Mathematical or Physical Character **208**, 349 (1908).
- [3] R. Jones. JOSA **37**, 879 (1947).
- [4] D. H. Andrews, W. F. Brucksch, and W. T. Ziegler. Physical Review **59**, 1045 (1941).
- [5] D. H. Andrews, R. M. Milton, and W. Desorbo. Journal of the Optical Society of America **36**, 518 (1946).
- [6] W. Boyle, J. Rodgers, and Others. JOSA **49**, 66 (1959).
- [7] F. J. Low. Journal of the Optical Society of America **51**, 1300 (1961).
- [8] K. D. Irwin. Phonon-Mediated Particle Detection Using Superconducting Tungsten Transition-Edge Sensors. Ph.D. thesis (1995).
- [9] S. Bandler. SPIE Newsroom 2–4 (2010).
- [10] C. Enss, A. Fleischmann, K. Horst, J. Schonefeld, J. Sollner, J. S. Adams, Y. H. Huang, Y. H. Kim, and G. M. Seidel. Journal of Low Temperature Physics **121**, 137 (2000).
- [11] P. Day, H. LeDuc, B. Mazin, A. Vayonakis, and J. Zmuidzinas. Nature **425**, 817 (2003).
- [12] B. Mazin, P. Day, J. Zmuidzinas, and H. LeDuc. In AIP Conference Proceedings, 309–312. Citeseer (2002).
- [13] S. P. Langley. Proceedings of the American Academy of Arts and Sciences **14**, 106 (1878).
- [14] C. L. Hunt, J. J. Bock, P. K. Day, A. Goldin, A. E. Lange, H. G. LeDuc, A. Vayonakis, and J. Zmuidzinas. In Proceedings of SPIE, volume 4855, 318 (2003).
- [15] K. Irwin. Applied Physics Letters **66**, 1998 (1995).
- [16] K. D. Irwin, G. C. Hilton, D. a. Wollman, and J. M. Martinis. Applied Physics Letters **69**, 1945 (1996).
- [17] D. Schwan, F. Bertoldi, S. Cho, M. Dobbs, R. Guesten, N. W. Halverson, W. L. Holzapfel, E. Kreysa, T. M. Lanting, A. T. Lee, and Others. New Astronomy Reviews **47**, 933 (2003).
- [18] A. Kosowsky. New Astronomy Reviews **47**, 939 (2003).
- [19] D. Becker, J. Beall, H. M. Cho, W. Duncan, G. Hilton, R. Horansky, K. Irwin, P. Lowell, M. Niemack, N. Paultre, and Others (2010).

- [20] J. J. Bock, M. Kenyon, K. Irwin, M. Bradford, J. P. L. Caltech, M. Devlin, U. Penn, A. Lange, C. Jpl, A. Lee, U. C. Berkeley, and B. Mason. *Jet Propulsion* 1–11.
- [21] W. S. Holland, W. Duncan, B. D. Kelly, K. D. Irwin, A. J. Walton, P. A. R. Ade, and E. I. Robson. In *Proceedings of SPIE*, volume 4855, 1 (2003).
- [22] D. Morozov, P. D. Mauskopf, P. Ade, M. Bruijn, P. A. J. de Korte, H. Hoevers, M. Ridder, P. Khosropahah, B. Dirks, and J. R. Gao. In *AIP Conference Proceedings*, volume 1185, 48 (2009).
- [23] B. Cabrera, R. M. Clarke, P. Colling, A. J. Miller, S. Nam, and R. W. Romani. *Applied Physics Letters* **73**, 735 (1998).
- [24] N. E. White and H. Tananbaum. *Nuclear Instruments and Methods in Physics Research Section A: Accelerators, Spectrometers, Detectors and Associated Equipment* **436**, 201 (1999).
- [25] D. A. Wollman, K. D. Irwin, G. C. Hilton, L. L. Dulcie, D. E. Newbury, and J. M. Martinis. *Journal of Microscopy* **188**, 196 (1997).
- [26] W. B. Doriese, J. N. Ullom, J. a. Beall, W. D. Duncan, L. Ferreira, G. C. Hilton, R. D. Horansky, K. D. Irwin, J. a. B. Mates, C. D. Reintsema, L. R. Vale, Y. Xu, B. L. Zink, M. W. Rabin, a. S. Hoover, C. R. Rudy, and D. T. Vo. *Applied Physics Letters* **90**, 193508 (2007).
- [27] R. D. Horansky, J. N. Ullom, J. A. Beall, G. C. Hilton, K. D. Irwin, D. E. Dry, E. P. Hastings, S. P. Lamont, C. R. Rudy, and M. W. Rabin. *Applied Physics Letters* **93**, 123504 (2008).
- [28] J. C. Mather. *Applied Optics* **21**, 1125 (1982).
- [29] A. T. Lee, P. L. Richards, S. W. Nam, B. Cabrera, and K. D. Irwin. *Applied Physics Letters* **69**, 1801 (1996).
- [30] B. D. Josephson. *Physics Letters* **1**, 251 (1962).
- [31] B. D. Josephson. *Reviews of Modern Physics* **46**, 251 (1974).
- [32] J. Clarke and A. I. Braginski. *The SQUID handbook*, volume 1. Wiley-Vch (2006). ISBN 3527402292.
- [33] R. C. Jaklevic, J. Lambe, A. H. Silver, and J. E. Mercereau. *Physical Review Letters* **12**, 159 (1964).
- [34] A. H. Silver and J. E. Zimmerman. *Physical Review* **157**, 317 (1967).
- [35] Y. Aharonov and D. Bohm. *Physical Review* **115**, 485 (1959).
- [36] M. Tinkham. *Introduction to superconductivity*. Dover Pubns (2004). ISBN 0486435032.
- [37] T. Van Duzer and C. W. Turner. *Principles of superconductive devices and circuits*. Prentice Hall (1999). ISBN 0132627426.
- [38] W. Seidel, G. Forster, W. Christen, F. von Feilitzsch, H. G\"obel, F. Pr\"obst, and R. L. M\"obius. *Physics Letters B* **236**, 483 (1990).
- [39] J. Zmuidzinas. historical trends. personal communication.
- [40] C. Shannon. *Proceedings of the IEEE* **86**, 447 (1998).
- [41] J. a. Chervenak, K. D. Irwin, E. N. Grossman, J. M. Martinis, C. D. Reintsema, and M. E. Huber. *Applied Physics Letters* **74**, 4043 (1999).
- [42] J. Chervenak, E. Grossman, K. Irwin, J. Martinis, C. Reintsema, C. Allen, D. Bergman, S. Moseley, and R. Shafer. *Nuclear Instruments and Methods in Physics Research Section A: Accelerators, Spectrometers, Detectors and Associated Equipment* **444**, 107 (2000).

- [43] D. J. Benford, T. A. Ames, J. A. Chervenak, E. N. Grossman, K. D. Irwin, S. A. Khan, B. Maffei, S. H. Moseley, F. Pajot, T. G. Phillips, and Others. In AIP Conference proceedings, 589–594. IOP INSTITUTE OF PHYSICS PUBLISHING LTD (2002).
- [44] D. Benford, C. Allen, J. Chervenak, M. Freund, A. Kutyrev, S. Moseley, R. Shafer, J. Staguhn, E. Grossman, G. Hilton, and Others. International Journal of Infrared and Millimeter Waves **21**, 1909 (2000).
- [45] A. L. Woodcraft, P. a. R. Ade, D. Bintley, J. S. House, C. L. Hunt, R. V. Sudiwala, W. B. Doriese, W. D. Duncan, G. C. Hilton, K. D. Irwin, C. D. Reintsema, J. N. Ullom, M. D. Audley, M. a. Ellis, W. S. Holland, M. MacIntosh, C. C. Dunare, W. Parkes, A. J. Walton, J. B. Kycia, M. Halpern, and E. Schulte. Review of Scientific Instruments **78**, 024502 (2007).
- [46] T. Lanting, H. Cho, J. Clarke, M. Dobbs, A. Lee, P. Richards, A. Smith, and H. Spieler. Applied Superconductivity, IEEE Transactions on **13**, 626 (2003).
- [47] M. F. Cunningham, J. N. Ullom, T. Miyazaki, S. E. Labov, J. Clarke, T. M. Lanting, A. T. Lee, P. L. Richards, J. Yoon, and H. Spieler. Applied Physics Letters **81**, 159 (2002).
- [48] J. Yoon, J. Clarke, J. M. Gildemeister, A. T. Lee, M. J. Myers, P. L. Richards, and J. T. Skidmore. Applied Physics Letters **78**, 371 (2001).
- [49] M. Dobbs, N. W. Halverson, P. A. R. Ade, K. Basu, A. Beelen, F. Bertoldi, C. Cohalan, H. M. Cho, R. G\\\"osten, W. L. Holzapfel, and Others. New Astronomy Review **50**, 960 (2006).
- [50] J. Ruhl, P. A. Ade, J. E. Carlstrom, H. M. Cho, T. Crawford, M. Dobbs, C. H. Greer, N. Halverson, W. L. Holzapfel, T. M. Lanting, and Others. In Proceedings of SPIE (2004). ISBN 0819454303.
- [51] P. Oxley, P. A. Ade, C. Baccigalupi, P. DeBernardis, H. M. Cho, M. J. Devlin, S. Hanany, B. R. Johnson, T. Jones, A. T. Lee, and Others. In Society of Photo-Optical Instrumentation Engineers (SPIE) Conference Series, volume 5543, 320–331 (2004).
- [52] K. D. Irwin, M. D. Niemack, J. Beyer, H. M. Cho, W. B. Doriese, G. C. Hilton, C. D. Reintsema, D. R. Schmidt, J. N. Ullom, and L. R. Vale. Superconductor Science and Technology **23**, 34004 (2010).
- [53] M. D. Niemack, J. Beyer, H. M. Cho, W. B. Doriese, G. C. Hilton, K. D. Irwin, C. D. Reintsema, D. R. Schmidt, J. N. Ullom, and L. R. Vale. Applied Physics Letters **96**, 163509 (2010).
- [54] C. E. Shannon. ACM SIGMOBILE Mobile Computing and Communications Review **5**, 3 (2001).
- [55] K. Irwin. In AIP Conference Proceedings, volume 1185, 229 (2009).
- [56] B. a. Mazin, B. Bumble, P. K. Day, M. E. Eckart, S. Golwala, J. Zmuidzinas, and F. A. Harrison. Applied Physics Letters **89**, 222507 (2006).
- [57] P. K. Day, H. G. Leduc, A. Goldin, T. Vayonakis, B. A. Mazin, S. Kumar, J. Gao, and J. Zmuidzinas. Nuclear Instruments and Methods in Physics Research Section A: Accelerators, Spectrometers, Detectors and Associated Equipment **559**, 561 (2006).
- [58] J. Gao. The physics of superconducting microwave resonators. Ph.D. thesis, California Institute of Technology (2008).
- [59] K. Duh, M. Pospieszalski, W. Kopp, P. Ho, a.a. Jabra, P.-C. Chao, P. Smith, L. Lester, J. Ballingall, and S. Weinreb. IEEE Transactions on Electron Devices **35**, 249 (1988).
- [60] P. R. Maloney, N. G. Czakon, P. K. Day, T. P. Downes, R. Duan, J. Gao, J. Glenn, S. R. Golwala, M. I. Hollister, H. G. LeDuc, and Others. In Proceedings of SPIE, volume 7741, 77410F (2010).
- [61] J. Schlaerth, A. Vayonakis, P. Day, J. Glenn, J. Gao, S. Golwala, S. Kumar, H. LeDuc, B. Mazin, J. Vaillancourt, and Others. J Low Temp Phys **151**, 684 (2008).

- [62] K. Irwin and K. Lehnert. *Applied Physics Letters* **85**, 2107 (2004).
- [63] J. a. B. Mates, G. C. Hilton, K. D. Irwin, L. R. Vale, and K. W. Lehnert. *Applied Physics Letters* **92**, 023514 (2008).
- [64] P. Day, B. Bumble, and H. G. Leduc. *Journal of Low Temperature Physics* **151**, 934 (2008).
- [65] S. Corvaja. *Nature* **458** (2009).
- [66] L. Knox and Y.-S. Song. *Physical Review Letters* **89**, 1 (2002).
- [67] S. Dodelson, R. Easther, S. Hanany, L. McAllister, S. Meyer, L. Page, P. Ade, A. Amblard, A. Ashoorioon, C. Baccigalupi, and Others. In *AGB Stars and Related Phenomena 2010: The Astronomy and Astrophysics Decadal Survey*, volume 2010, 67 (2009).
- [68] T. Essinger-Hileman, J. W. Appel, J. A. Beal, H. M. Cho, J. Fowler, M. Halpern, M. Hasselfield, K. D. Irwin, T. A. Marriage, M. D. Niemack, and Others. In *AIP Conference Proceedings*, volume 1185, 494 (2009).
- [69] J. J. McMahon, K. A. Aird, B. A. Benson, L. E. Bleem, J. Britton, J. E. Carlstrom, C. L. Chang, H. S. Cho, T. de Haan, T. M. Crawford, and Others. In *American Institute of Physics Conference Series*, volume 1185, 511–514 (2009).
- [70] M. C. Runyan, P. A. R. Ade, R. S. Bhatia, J. J. Bock, M. D. Daub, J. H. Goldstein, C. V. Haynes, W. L. Holzapfel, C. L. Kuo, A. E. Lange, and Others. *The Astrophysical Journal Supplement Series* **149**, 265 (2003).
- [71] J. Britton, K. Yoon, J. Beall, D. Becker, H. Cho, G. Hilton, M. Niemack, and K. Irwin. In *American Institute of Physics Conference Series*, B. Young, B. Cabrera, & A. Miller, ed., *American Institute of Physics Conference Series* 1185, 375378 (Dec, 375–378 (2009)).
- [72] K. W. Yoon, J. W. Appel, J. E. Austermann, J. A. Beall, D. Becker, B. A. Benson, L. E. Bleem, J. Britton, C. L. Chang, J. E. Carlstrom, and Others. In *AIP Conference Proceedings*, volume 1185, 515 (2009).
- [73] P. K. Hansma. *Journal of Applied Physics* **44**, 130 (1973).
- [74] K. K. Likharev. *Dynamics of Josephson Junctions and Circuits*. Gordon and Breach (1986). ISBN 2-88124-042-9.
- [75] D. M. Pozar. *Microwave Engineering*, 3rd (2005).
- [76] I. Siddiqi, R. Vijay, F. Pierre, C. M. Wilson, L. Frunzio, M. Metcalfe, C. Rigetti, R. J. Schoelkopf, M. H. Devoret, D. Vion, and Others. *Physical review letters* **94**, 27005 (2005).
- [77] A. Vayonakis and J. Zmuidzinas. Radiative losses from 2-d apertures.
- [78] J. Gao, M. Daal, A. Vayonakis, S. Kumar, J. Zmuidzinas, B. Sadoulet, B. A. Mazin, P. K. Day, and H. G. Leduc. *Applied Physics Letters* **92**, 152505 (2008).
- [79] F. C. Wellstood, C. Urbina, and J. Clarke. *APPLIED PHYSICS LETTERS* **85**, 22 (2004).
- [80] F. C. Wellstood, C. Urbina, and J. Clarke. *Applied Physics Letters* **50**, 772 (2009).
- [81] R. H. Koch, D. P. DiVincenzo, and J. Clarke. *Physical review letters* **98**, 267003 (2007).
- [82] J. Gao, J. Zmuidzinas, B. A. Mazin, H. G. LeDuc, and P. K. Day. *Applied Physics Letters* **90**, 102507 (2009).
- [83] H. G. Leduc, B. Bumble, P. K. Day, A. D. Turner, B. H. Eom, S. Golwala, D. C. Moore, O. Noroozian, J. Zmuidzinas, J. Gao, and Others .

- [84] B. A. Mazin, P. K. Day, K. D. Irwin, C. D. Reintsema, and J. Zmuidzinas. *Nuclear Instruments and Methods in Physics Research Section A: Accelerators, Spectrometers, Detectors and Associated Equipment* **559**, 799 (2006).
- [85] B. A. Mazin, J. B. Mates, and K. D. Irwin .
- [86] AWR. TX-Line.
- [87] J. Krupka, J. Breeze, A. Centeno, N. Alford, T. Claussen, and L. Jensen. *Microwave Theory and Techniques, IEEE Transactions on* **54**, 3995 (2006).
- [88] M. J. Hatridge. *SQUID magnetometry from nanometer to centimeter length scales.* Ph.D. thesis, Ernest Orlando Lawrence Berkeley National Laboratory, Berkeley, CA (US) (2010).
- [89] M. Kamon, M. J. Tsuk, and J. K. White. *Microwave Theory and Techniques, IEEE Transactions on* **42**, 1750 (2002).
- [90] S. Doyle, P. Mauskopf, J. Naylor, A. Porch, and C. Duncombe. *Journal of Low Temperature Physics* **151**, 530 (2008).
- [91] S. Weber, K. W. Murch, D. H. Slichter, R. Vijay, and I. Siddiqi. *Arxiv preprint arXiv:1102.2917* (2011).
- [92] C. Huang. In *Vehicular Technology Conference, 1999 IEEE 49th*, volume 1, 342–345. IEEE (2002). ISBN 0780355652.
- [93] C. D. Reintsema, J. Beall, W. Doriese, W. Duncan, L. Ferreira, G. C. Hilton, K. D. Irwin, D. Schmidt, J. Ullom, L. Vale, and Others. *J Low Temp Phys* **151**, 927 (2008).
- [94] J. E. Zimmerman and A. H. Silver. *Physical Review* **141**, 367 (1966).
- [95] B. A. Mazin. *Microwave kinetic inductance detectors* (2005). ISBN 0496944924.
- [96] C. M. Caves. *Physical Review D* **26**, 1817 (1982).
- [97] S. Kumar, J. Gao, J. Zmuidzinas, B. A. Mazin, H. G. LeDuc, and P. K. Day. *Applied Physics Letters* **92**, 123503 (2008).
- [98] J. D. Jackson. *Classical Electrodynamics*. John Wiley and Sons, Inc. (1999).

Appendix A

Instruments and Components

The primary instruments used in this work were:

- Agilent E5071B Network Analyzer
- Agilent E4407B Spectrum Analyzer
- Agilent E8247C Signal Generator
- Anritsu 68369A/NV Signal Generator
- National Instruments PCI-6132 Digitizer
- Hewlett Packard 3562A Dynamic Signal Analyzer

The primary microwave components were:

- HEMT 0.5-11 GHz (Sander Weinreb, Caltech)
- Miteq AFS4-00101000-35-10P-4 Amplifier
- Marki Microwave IQ0307LXP IQ-Mixer
- Pamtech CTH1392K4 Circulator

We used coaxial cables from Coax-Co to minimize the heat load on our ADR.

- SC-086/50-SCN-CN
- SC-160/50-NbTi-NbTi

Appendix B

Transformer Coupling Calculations

Screening currents (Figure B.1) flow in the rf SQUID loop and change the effective load on the resonator.

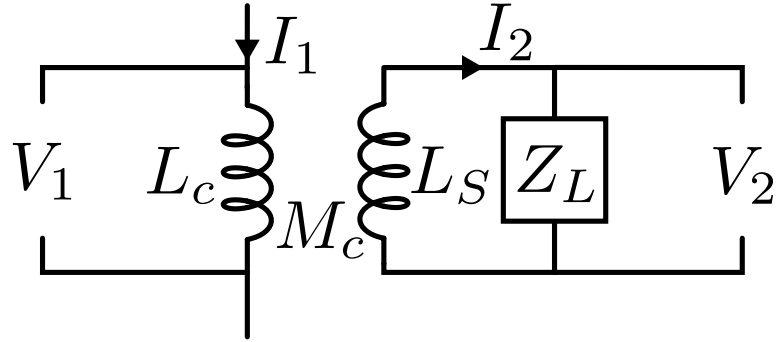


Figure B.1: Circuit diagram of an rf-SQUID screening an inductor.

To find the effective load Z_{eff} we solve a coupled set of linear equations:

$$V_1 = i\omega I_1 L_c - i\omega I_2 M_c \quad (\text{B.1})$$

$$V_2 = -i\omega I_2 L_S + i\omega I_1 M_c = I_2 Z_L \quad (\text{B.2})$$

We can write the screening current in terms of the primary current:

$$I_1 = I_2 \frac{i\omega L_S + Z_L}{i\omega M_c} \quad (\text{B.3})$$

and apply it back to the primary inductor to find the voltage drop:

$$V_1 = i\omega I_1 \left(L_c - \frac{M_c^2}{L_S + Z_L/i\omega} \right) \quad (\text{B.4})$$

which defines an effective impedance of

$$Z_{\text{eff}} = i\omega \left(L_c - \frac{M_c^2}{L_S + Z_L/i\omega} \right) \quad (\text{B.5})$$

B.1 Shunted Junction

Practical Josephson junctions have some capacitance C_J and leakage resistance R_{sg} which shunt the junction inductance (Figure B.2).

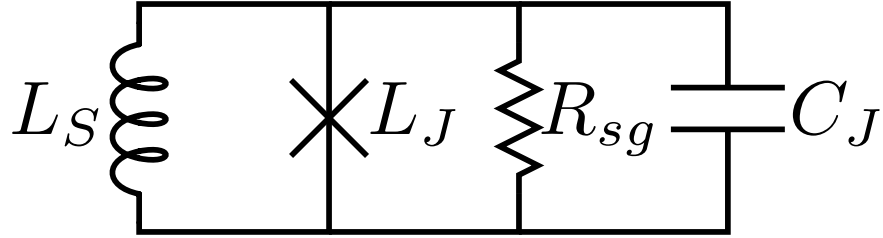


Figure B.2: SQUID circuit including leakage resistance and junction capacitance.

The effect of these shunts on the effective load impedance can be calculated exactly, but it is more elucidating to consider the perturbation theory. Let $y_s \equiv i\omega L_J Y_s$ be the admittance of the parallel shunts, normalized to the junction inductance.

$$Z_{\text{eff}} = i\omega \left(L_c - \frac{M_c^2}{L_S + \frac{L_J}{\cos \phi + y_s}} \right) \quad (\text{B.6})$$

We then consider y_s to be small:

$$Z_{\text{eff}} = i\omega \left(L_c - \frac{M_c^2}{L_S + L_J \sec \phi} \right) - i\omega \frac{M_c^2}{L_J} \left(\lambda + \frac{1}{\cos \phi} \right)^{-2} (\cos \phi)^{-2} y_s + \dots \quad (\text{B.7})$$

$$\approx i\omega \left(L_c - \frac{M_c^2}{L_S + L_J \sec \phi} \right) - i\omega \frac{M_c^2}{L_J} (1 + \lambda \cos \phi)^{-2} y_s \quad (\text{B.8})$$

$$\approx i\omega \left(L_c - \frac{M_c^2}{L_S + L_J \sec \phi} \right) + \frac{(\omega M_c)^2 Y_s}{(1 + \lambda \cos \phi)^2} \quad (\text{B.9})$$

Note that the denominator minimizes to $1 - \lambda$ so the greatest change in load impedance due to the junction shunts is

$$\Delta Z_{\text{eff}} \approx \frac{(\omega M_c)^2 Y_s}{(1 + \lambda)^2} \quad (\text{B.10})$$

B.2 Input Filter

The circuit that feeds a magnetic flux signal to the SQUID (Figure 2.17) may present an impedance with a real component. Microwave power in the resonator may therefore dissipate in the input circuit.

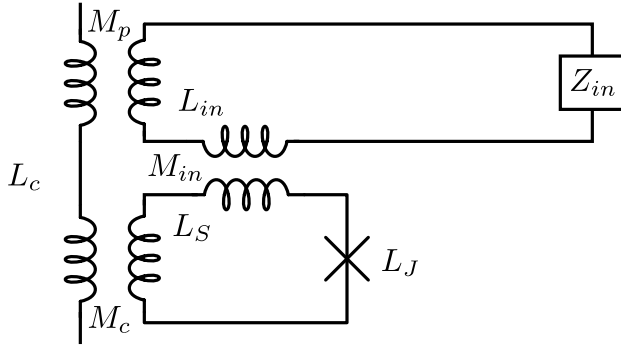


Figure B.3: Schematic of the rf-SQUID and input coil coupling to both the resonator and each other.

There are two ways for the microwave power to couple to the input circuit. First, there is an unavoidable parasitic coupling from the resonator termination into the input coil. Second, the resonator drives microwave currents in the SQUID loop which directly couple to the input coil. Maximum coupling occurs when $\phi = \pi$ and the SQUID effectively "anti-screens" flux from the resonator. Solving the coupled set of linear equations:

$$Z_L = i\omega \left(L_c - \frac{M_p^2 L_S (1 - \lambda^{-1}) + M_c^2 (L_{in} + Z_{in}/i\omega) - 2M_{in}M_cM_p}{L_S(1 - \lambda^{-1})(L_{in} + Z_{in}/i\omega) - M_{in}^2} \right) \quad (\text{B.11})$$

$$= i\omega \left(L_c + \frac{M_c^2 (L_{in} + Z_{in}/i\omega) - 2L_S M_p^2 - 2M_{in}M_cM_p}{2L_S(L_{in} + Z_{in}/i\omega) + M_{in}^2} \right) \quad (\text{B.12})$$

Assume that the input circuit can be seen as a low-pass filter $Z_{in} = i\omega L_F + R_F$ with a cutoff frequency of $\omega_F = \frac{R_F}{L_F + L_{in}}$ far below the microwave resonance frequency. On resonance then:

$$\text{Re}[Z_L] = -\omega_0 \text{Im} \left[\frac{M_c^2(L_{in} + Z_{in}/i\omega) - 2L_S M_p^2 - 2M_{in} M_c M_p}{2L_S(L_{in} + Z_{in}/i\omega) + M_{in}^2} \right] \quad (\text{B.13})$$

$$= -\omega_0 \text{Im} \left[\frac{M_c^2(L_{in} + L_F)(1 - i\frac{\omega_F}{\omega_0}) - 2L_S M_p^2 - 2M_{in} M_c M_p}{2L_S(L_{in} + L_F)(1 - i\frac{\omega_F}{\omega_0}) + M_{in}^2} \right] \quad (\text{B.14})$$

$$= \omega_F \frac{M_c^2(L_{in} + L_F) (2L_S(L_{in} + L_F) + M_{in}^2) - 2L_S(L_{in} + L_F) (M_c^2(L_{in} + L_F) - 2L_S M_p^2 - 2M_{in} M_c M_p)}{(2L_S(L_{in} + L_F) + M_{in}^2)^2 + O\left((\frac{\omega_F}{\omega_0})^2\right)} \quad (\text{B.15})$$

$$= R_F \frac{M_c^2 (2L_S(L_{in} + L_F) + M_{in}^2) - 2L_S (M_c^2(L_{in} + L_F) - 2L_S M_p^2 - 2M_{in} M_c M_p)}{(2L_S(L_{in} + L_F) + M_{in}^2)^2 + O\left((\frac{\omega_F}{\omega_0})^2\right)} \quad (\text{B.16})$$

$$= R_F \frac{M_c^2 M_{in}^2 + 4L_S (L_S M_p^2 + M_{in} M_c M_p)}{(2L_S(L_{in} + L_F) + M_{in}^2)^2 + O\left((\frac{\omega_F}{\omega_0})^2\right)} \quad (\text{B.17})$$

$$\approx R_F \frac{M_c^2 M_{in}^2 + 4L_S (L_S M_p^2 + M_{in} M_c M_p)}{(2L_S(L_{in} + L_F) + M_{in}^2)^2} \quad (\text{B.18})$$

Appendix C

Derivative of Resonator Impedance

We previously derived an expression for the impedance of a lossless resonator:

$$Z_R(\omega) = \frac{1}{i\omega C_c} + Z_1 \frac{i\omega L \cot\left(\omega \frac{l}{v_p}\right) + iZ_1}{Z_1 \cot\left(\omega \frac{l}{v_p}\right) - \omega L} \quad (\text{C.1})$$

let $x \equiv \omega/\omega_0$ and $\alpha \equiv \omega_0/\omega_1$,

$$Z_R(\omega)/iZ_1 \approx \frac{\omega_0 x L \cot(x\alpha\pi/2) + Z_1}{Z_1 \cot(x\alpha\pi/2) - \omega_0 x L} - \frac{x^{-1}}{\omega_0 C_c Z_1} \quad (\text{C.2})$$

so that

$$\frac{\partial Z_R(\omega)/iZ_1}{\partial x} \Big|_{x=1} \approx \frac{\omega_0 L (\cot(\alpha\pi/2) - \alpha\pi/2) (Z_1 \cot(\alpha\pi/2) - \omega_0 L) - (\omega_0 L \cot(\alpha\pi/2) + Z_1) (-Z_1 \alpha\pi/2 - \omega_0 L)}{(Z_1 \cot(\alpha\pi/2) - \omega_0 L)^2} + \frac{1}{\omega_0 C_c Z_1} \quad (\text{C.3})$$

Although the cotangent terms in the numerator can be neglected, the cotangent term in the denominator dominates. To account for it, we can refer back to the resonance condition:

$$Z_1 \cot(x\alpha\pi/2) - \omega_0 L = (\omega_0 C_c Z_1) (\omega_0 L \cot(x\alpha\pi/2) + Z_1) \quad (\text{C.4})$$

so that

$$\frac{\partial Z_R(\omega)/iZ_1}{\partial x} \Big|_{x=1} \approx \frac{\omega_0 L (\cot(\alpha\pi/2) - \alpha\pi/2) (Z_1 \cot(\alpha\pi/2) - \omega_0 L) - (\omega_0 L \cot(\alpha\pi/2) + Z_1) (-Z_1 \alpha\pi/2 - \omega_0 L)}{(\omega_0 C_c Z_1)^2 (\omega_0 L \cot(x\alpha\pi/2) + Z_1)^2} + \frac{1}{\omega_0 C_c Z_0} \quad (\text{C.5})$$

$$\approx \frac{(\omega_0 L)^2 \alpha\pi/2 + Z_1 \omega_0 L + Z_1^2 \alpha\pi/2}{(\omega_0 C_c Z_1)^2 Z_1^2} + \frac{1}{\omega_0 C_c Z_0} \quad (\text{C.6})$$

$$\approx \frac{\pi}{2 (\omega_0 C_c Z_1)^2} \quad (\text{C.7})$$